Tunable Fiber Lasers based on fiber Bragg grating arrays and a Theta Ring Cavity

Dissertation

zur Erlangung des akademischen Grades Doktor-Ingenieur (Dr.-Ing.)

vorgelegt dem Rat der Physikalische-Astronomischen Fakultät der Friedrich-Schiller-Universität Jena

von Tobias Tieß
geboren am 15.06.1987 in Jena

1. Gutachter: Prof. Dr. Hartmut Bartelt (Friedrich-Schiller-Universität Jena)
2. Gutachter: Prof. Dr. Stefan Nolte (Friedrich-Schiller-Universität Jena)
3. Gutachter: Prof. Dr. Alain Villeneuve (Optav Solutions Montreal, Kanada)

Tag der Disputation: 27.11.2018

Contents

1 Introduction

Driven by the vision of advanced healthcare for society and extended life expectancy, global research efforts are increasingly focusing on the broad fields of life sciences, biophotonics and medical technology. Novel analysis techniques and enhanced concepts in spectroscopy enable faster and more precise diagnostics for deeper insights into molecular processes. An example is given by the nonlinear microscopy concept of stimulated emission depletion (STED) surpassing the resolution limitations of classical light microscopy [67], which has been awarded with the Nobel Prize in 2014. In the biophotonics industry, this development pushes sustainable growth rates with an expected doubling in market volume in the current decade [71].

This development is strongly linked to research for suitable light sources [103]. On the one hand, they need to meet advanced requirements of novel concepts and, on the other hand, also facilitate technological transfer to clinical applications. Research efforts are mainly linked to laser sciences based on the unique properties of the emitted light. Diverse functionality is enabled such as monochromacy and coherence, the generation of ultrashort pulses in the femtosecond scale with unprecedented peak powers or directional beams with superb brightness. Tunable lasers depict an important key technology in this process providing intense light sources with adaptable emission wavelengths. The spectral properties can be flexibly adjusted for application fields crucially depending on the exciting wavelength. Besides common industries like material processing and academic research, this particularly includes spectroscopy [28] as well as the medical sector comprising monitoring, probing, imaging, therapy and surgery [35].

Fiber lasers depict the perfect platform to develop such sources. Due to the waveguide structure, they combine an excellent beam quality in single-mode operation with high efficiencies and superb heat dissipation. This also reduces cost and complexity in the cooling design especially at high-power levels. Furthermore, rare-earth doped glasses as gain media in fiber lasers usually feature broad gain regions, providing a wide operation window for the tunable emission wavelength. It may span over tens to hundreds of nanometers offering an excellent spectral flexibility. In a fiber-integrated design, those advantages are potentially fused with robust designs as well as small footprint sizes, user-friendly operation and low-maintenance requirements. Accordingly, fiber lasers set the benchmark in leading-edge designs for many industries [81]. While typical applications addressed telecommunications as well as material processing, fiber-integrated light sources access new fields in the life sciences sector based on the spectral flexibility as well as system integrability [131]. All-fiber layouts accelerate the technological transfer rates from research to industry.

Accordingly, tunable fiber lasers are required to maintain a fiber-integrated structure as well as to provide huge spectral flexibility to exhaust the broad operation ranges enabled by rare-earth doped fibers. Common tuning approaches applied in the research sector do not combine both demands. On the one hand, free-space coupled diffraction gratings operate over huge bandwidths on the cost of prohibiting an all-fiber structure. On the other hand, fiber Bragg gratings (FBGs) as narrowband mirrors inscribed in the core of the fiber only allow small tuning bandwidths typically in the range of a few nanometers by applying strain or temperature variations [35].

While there is a zoo of alternative rather academic tuning approaches that can be integrated into a fiber network, a new concept has been presented in the last decade working with a chirped FBG structure as spectral filter operating over extended bandwidths [149]. The distributed filter feedback is utilized for controlling the emission wavelength via the pulse repetition rate (PRR). This dispersion tuning approach for pulsed lasers in a specific sigma-ring cavity setup combines an all-fiber design with excellent emission properties and programmable operation. In case of discretely chirped FBG arrays as spectral filters, they also feature the unique possibility for customized tuning ranges tailored to a specific application [143]. Due to the potential of this concept in the growing markets of biophotonics and spectroscopy, the Canadian company `Genia Photonics Inc.` commercialized dispersion tuned all-fiber lasers in the sigma-ring cavity layout [148, 149]. They utilize continuously chirped FBGs and electro-optic modulators to achieve compact tunable picosecond lasers with decent bandwidths of multiple ten nanometers.

Still, dispersion tuning in the sigma-ring cavity is inherently connected to a changing PRR along the tuning range. This particularly applies to the scenario with discretely chirped FBG arrays enabling vast bandwidths. Due to the long filter structure, the PRR changes significantly over the full tuning range. In the case of reference [143] applying long FBG arrays for a record tuning bandwidth of $74\,nm$, the PRR changes by a factor of about 2 from the first to the last emission line. The direct link between the PRR and the emission wavelength is problematic in various applications that, e.g., rely on clocked processes. This concerns sped up measurement setups with synchronized detectors as well as nonlinear frequency generation based on overlapping two tunable pulsed lasers. Additionally, the massive change in the PRR promotes inconsistent pulse properties (e.g.: pulse energy, peak power, duration) along the tuning range [139].

A solution to this dilemma is developed in the present work by a novel resonator design. The theta-ring cavity layout features an outer unidirectional ring structure coupled to a bidirectionally operated middle branch with a reflective filter such as an FBG (e.g.: see Fig. 3.1). In general, theta resonator designs have been reported in several application fields. As an example, chirped pulse oscillators with intracavity dispersion management have been demonstrated based on a theta cavity layout and chirped FBGs [87, 99]. Furthermore, Li et al. presented a tunable fiber laser using cascaded FBGs in a theta layout [90]. However, spectral tuning was operated via a polarization controller lacking usability and flexibility to scale the tuning features. An alternative approach with two modulators working with harmonic loss modulation only achieved a tuning range of $1\,nm$ in a theta configuration [85].

In the present work, the theta-ring cavity layout is utilized to develop broadly tunable fiber-integrated lasers working with FBG arrays as discrete spectral filters. A middle branch incorporates two counter-propagating passes through the reflective filter compensating for the distributed feedback delay over one round trip. Thus, the theta-ring cavity facilitates a constant PRR over the tuning range due to matched spectral path lengths. To incorporate tunability, optical gating of pulses is applied presetting the time of flight in the filter structure to select an emission wavelength out of the ensemble provided by the FBG array. Optical gating via an electronic control signal ensures programmable operation without relying on any mechanically moving element. Additionally, customized optical gating signals enable unique flexibility to drive the system in novel operation regimes (e.g. tunable multi-wavelength emission) or

remotely-control further emission properties (e.g. pulse duration). Hence, it may provide a powerful platform to tailor the emission properties of this fiber-integrated laser for accessing novel application fields. The present work targets the development of this new tuning concept based on the theta-ring cavity and to evaluate its performance as well as prospects.

Following this **introduction**, the thesis starts with a brief overview over the fundamentals of optical fibers focusing on the propagation properties of light. **Chapter 2** also introduces FBGs as narrowband reflectors inscribed into the fiber core that depict a key element in the presented tuning concept. Furthermore, the principles of fiber lasers are presented with an extended study on the potential gain bandwidths of Yb-doped fibers. Correspondingly, the subsequent part provides an overview over the state of the art in tuning concepts utilized for fiber lasers.

Chapter 3 introduces the new tuning concept of the theta cavity fiber laser (TCFL) based on a novel resonator configuration ensuring a constant PRR for dispersion tuned lasers with FBG arrays as versatile spectral filters. The optical gating approach to control the spectral emission properties is outlined, providing new prospects to extend the feature set of tunable fiber lasers. The experimental study gives a proof of principle demonstrating adjustable emission wavelengths with tuning bandwidths of up to $50\,nm$. Following on design considerations in the resonator layout to unravel the full tuning potential, major emission properties are discussed as well as their dependencies from the optical gating parameters. Parts of the results are published in reference [140]. Additionally, the novel tuning concept was filed for a German patent, which has been granted in 2018 [76].

Based on the specific resonator layout as well as the optical gating approach with unique freedom in tailoring and remote-controlling multiple emission characteristics, **Chapter 4** highlights the potential of the TCFL to access new application fields by presenting two advanced operation concepts beyond a plain tunable laser. In the first part, the laser resonator is utilized to implement a new method for dispersion characterization of optical fibers by a direct temporal measurement. Based on evaluating pulse shape variations along the tuning range depending on the applied gating parameters with sensitivities in the sub $10\,ps$ scale, two fiber samples have been analyzed comparing the retrieved dispersion parameter to simulations as well as a reference experimental method. A corresponding manuscript is in preparation for publication.

In the second part of chapter 4, the tuning concept is extended towards a tunable multi-wavelength regime generated in a single oscillator. Solely by modifying the optical gating signal, the TCFL can be operated with multiple emission wavelengths that are independently tunable and feature an inherently synchronized pulsed output. This unique operation mode is experimentally investigated based on a tunable dual-wavelength emission. A fiber-integrated time-delay spectrometer (TDS) has been developed to analyze and optimize the pulse overlap between both emission lines. The potential to further scale the number of emission wavelengths is outlined demonstrating tunable triple-wavelength emission. The main results are published in references [141, 145].

Chapter 5 concludes on the major results of the thesis investigating and developing the new tuning concept based on the TCFL. A short outlook is given on potential routes to promote this approach.

2 Fundamentals

This chapter introduces fundamental concepts and principles of optical fibers as well as fiber lasers. Covering the scope of the thesis, the amplification bandwidth of the gain medium, fiber Bragg gratings (FBGs) as fiber-integrated spectral filters and the dispersion properties of optical fibers are discussed in greater depth. Furthermore, the state of the art in tunable fiber lasers is provided by an overview over common tuning concepts and their limitations.

2.1 Optical fibers

The concept of optical fibers as well as their mathematical treatment and technological platform are extensively discussed in literature (see, e.g., [6,27,104,111,120,124,133]). The basic principles are summarized in this section.

2.1.1 Structure of an optical fiber

In the following, an optical fiber will be simply referred to as fiber. The principle structure of a standard step-index fiber is depicted in Fig. 2.1.

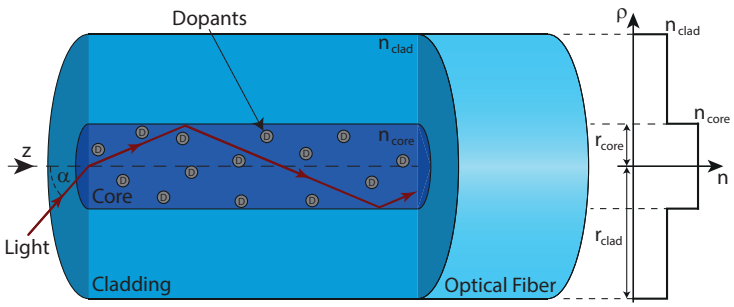

Fig. 2.1: Principle structure of a step-index fiber with a doped core region. The graph sketches the refractive index n over the radius ρ.

It comprises an inner core region with radius r_{core} and refractive index n_{core} surrounded by an outer cladding with radius r_{clad} and refractive index n_{clad}. In order to guide light along the fiber axis (z-direction), the refractive index n_{core} must be larger than n_{clad} as depicted in the graph of Fig. 2.1 over the radial coordinate ρ. Accordingly, light rays with an incoupling angle of $\alpha < \alpha_{crit}$ are guided in the core due to total internal reflection on the interface core and cladding, allowing for low-loss transmission of signals over long distances. Applying Snell's law of refraction, the critical acceptance angle α_{crit} is calculated from the fiber parameters by

$$\sin(\alpha_{crit}) = \sqrt{n_{core}^2 - n_{clad}^2} = NA. \tag{2.1}$$

The numerical aperture NA (also known as core-NA) is a characteristic parameter pointing to the refractive index difference between core and cladding. Following the ray optics picture, the greater the NA is, the larger might be the acceptance angle for incoming beams or divergence angle for output beams.

As indicated in Fig. 2.1, the core region of the fiber often is composed of additional dopants in order to incorporate a specific functionality. Besides the adjustment of n_{core} with respect to n_{clad}, this comprises e.g. optical amplification to realize fiber lasers. As will be discussed in subsection 2.3.1, such active fibers are usually doped with rare-earth elements.

Depending on the application, optical fibers may have much more elaborate designs featuring different functionality. One example is given by polarization-maintaining (PM) fibers, which usually break the rotational symmetry of the structure by stress elements in the cladding or a non-circular core to introduce birefringence that decouples the modes of different polarizations [118]. Well known layouts of PM fibers are panda fibers, bow-tie fibers or elliptical core fibers. More complex fiber geometries are often labeled as microstructured fibers. They work with complex core and cladding structures to engineer effective propagation properties that are hardly accessible by plain fiber designs and standard materials. Some examples are given by photonic-crystal fibers [118], suspended core fibers [43], photonic bandgap fibers [41], hollow core fibers [82] or large-pitch fibers [93].

2.1.2 Light propagation

The ray optics approach applied in section 2.1 only provides a basic understanding of the light guidance in step-index fibers. In contrast, a comprehensive description of the physical effects occurring for light propagating in small waveguide structures is given by the wave-optical treatment [104]. Starting from Maxwells equations for electromagnetism [102], the general wave equation can be derived as

$$\nabla \times \nabla \times \mathbf{E} = -\frac{1}{c_0^2}\frac{\partial^2 \mathbf{E}}{\partial t^2} - \mu_0 \frac{\partial^2 \mathbf{P}}{\partial t^2} \tag{2.2}$$

with $\mathbf{E}$ as the electric field vector, $\mathbf{P}$ the polarization vector, t the time, c_0 the speed of light in vacuum and μ_0 the vacuum permeability. Bold parameters represent vectors. The polarization $\mathbf{P}$ is connected to the electrical field $\mathbf{E}$ given by

$$\mathbf{P} = \epsilon_0(\chi^{(1)}\mathbf{E} + \chi^{(2)}\mathbf{E}^2 + \chi^{(3)}\mathbf{E}^3 + ...) \tag{2.3}$$

with ϵ_0 as the vacuum permittivity. The corresponding material response linking both parameters is represented via the j^{th} order susceptibility tensor $\chi^{(j)}$. While for strong electrical field strengths, nonlinear terms ($j > 1$) show a significant contribution, weak field interactions are well approximated by only the linear material response ($j = 1$).

Assuming the linear regime and loss-less media, equation (2.2) can be simplified to the Helmholtz equation in the frequency domain

$$\triangle \widetilde{\mathbf{E}}(\mathbf{r}, \omega) + n(\mathbf{r}, \omega)^2 \frac{\omega^2}{c_0^2} \widetilde{\mathbf{E}}(\mathbf{r}, \omega) = 0 \ . \tag{2.4}$$

It models the propagation of a light wave in a dielectric medium such as a fiber. The refractive index of the medium is given by $n(\mathbf{r}, \omega) = \sqrt{1 + \chi^{(1)}(\mathbf{r}, \omega)}$ with the position vector $\mathbf{r}$ and the radial frequency ω. The electric field vector in the frequency domain $\widetilde{\mathbf{E}}(\mathbf{r}, \omega)$ is obtained via the Fourier transform of the electric field vector $\mathbf{E}(\mathbf{r}, t)$ by

$$\widetilde{\mathbf{E}}(\mathbf{r}, \omega) = \int_{-\infty}^{+\infty} \mathbf{E}(\mathbf{r}, t) e^{i\omega t} \mathrm{d}t \ . \tag{2.5}$$

The Helmholtz equation describes a discrete set of solutions for the electrical field distribution $\widetilde{\mathbf{E}}(\mathbf{r},\omega)$ that can propagate through a fiber. These mutually orthogonal solutions are denoted as modes. In arbitrary geometries, they are numerically calculated with commercial mode solvers such as provided by `COMSOL Multiphysics`®.

For step-index fibers, analytical solutions can be obtained. Adapting to the rotational symmetry of this geometry, equation (2.4) can be solved with the separation ansatz in cylindrical coordinates (radial: ρ, azimuthal: φ) for field component $\widetilde{\mathbf{E}}_\mathbf{z}$ [6] by

$$\widetilde{\mathbf{E}}_\mathbf{z}(\mathbf{r},\omega) = A(\omega)B(\rho,\varphi)e^{i\beta(\omega)z} \ . \tag{2.6}$$

$A(\omega)$ is a spectral normalization parameter that is significant as envelope function for pulsed signals. $B(\rho,\varphi)$ describes the 2-dimensional field distribution of the modes in the fiber propagating along the z-direction. The ρ component is derived from a differential equation solved in the core region and the cladding region giving Bessel functions [16] as solutions. The propagation of a specific mode j in the fiber is governed by the corresponding propagation constant $\beta_{(j)}(\omega)$. The number of modes that are guided in the core region can be determined with the normalized frequency V given by

$$V = r_{core}k_0\sqrt{n_{core}^2 - n_{clad}^2} = r_{core}k_0 NA \ . \tag{2.7}$$

The vacuum wave number k_0 is calculated by

$$k_0 = \omega/c_0 = 2\pi/\lambda \ . \tag{2.8}$$

The larger V is, the more transversal modes may be guided by the core area. For fiber layouts with $V < 2.405$ at the operation wavelength, the core only supports the fundamental transversal mode HE_{11} that is degenerated in two mutually orthogonal polarizations. Most fiber designs for laser applications target single-mode (SM) operation ensuring a superb Gaussian-like beam quality matching the highest demands. The lasers in this work are developed within the SM regime.

2.1.3 Chromatic dispersion in a fiber

The propagation constant $\beta(\omega)$ is a measure for the traveling speed of a mode in z-direction. The underlying frequency dependency is called chromatic dispersion. In an optical fiber, the effective dispersion in $\beta(\omega)$ is composed of a material contribution, arising from the spectral dependency of the refractive index $n(\omega)$, and the modal dispersion, originating from the waveguide geometry.

A transversal fiber mode is connected to a specific $\beta(\omega)$ that defines the corresponding effective mode index n_{eff} as

$$n_{eff}(\omega) = \frac{\lambda}{2\pi}\beta(\omega) = \frac{\beta(\omega)}{k_0} = \frac{c_0}{\omega}\beta(\omega) \ . \tag{2.9}$$

The phase velocity v_{ph} of the respective mode is governed by

$$v_{ph} = \frac{c_0}{n_{eff}(\omega)} = \frac{\omega}{\beta(\omega)} \ . \tag{2.10}$$

Modes that are guided by the core region follow the relation $n_{clad} < n_{eff} < n_{core}$.

However, the actual propagation speed of a signal, such as a pulse, is determined by the group velocity

$$v_{gr} = \frac{d\omega}{d\beta} \ . \tag{2.11}$$

The corresponding group propagation time τ_{gr} along a fiber segment of length L results to

$$\tau_{gr} = \frac{L}{v_{gr}} = L\frac{d\beta}{d\omega} = L\frac{d\beta}{d\lambda}\frac{d\lambda}{d\omega} \ . \tag{2.12}$$

Applying equation(2.8) and equation(2.9), this relation can be simplified to

$$\tau_{gr} = \frac{L}{c_0}\left(n_{eff} - \lambda\frac{dn_{eff}}{d\lambda}\right) = \frac{L}{c_0}n_{gr,eff} \tag{2.13}$$

with the effective group index $n_{gr,eff}$ determining the pulse propagation speed $v_{gr} = c_0/n_{gr,eff}$.

For signals comprising different wavelengths, the spectral variation of the group propagation time is estimated from

$$\Delta\tau_{gr} = \frac{d\tau_{gr}}{d\lambda}\Delta\lambda \ . \tag{2.14}$$

The derivative is calculated with equation(2.13) by

$$\frac{d\tau_{gr}}{d\lambda} = L\frac{\lambda}{c_0}\frac{d^2n_{eff}}{d\lambda^2} \ . \tag{2.15}$$

Normalizing this derivative by the length L defines the dispersion parameter D_λ

$$D_\lambda = -\frac{\lambda}{c_0}\frac{d^2n_{eff}}{d\lambda^2} = -\frac{2\pi c_0}{\lambda^2}\frac{d^2\beta}{d\omega^2} \ . \tag{2.16}$$

as a characteristic value for the fiber dispersion. The transfer to the second expression is derived by plugging in equation(2.8) and equation(2.9). In an illustrative picture, D_λ denotes the dispersion-caused temporal delay experienced by a traveling signal per spectral bandwidth and per propagation distance in a fiber. Alternatively, fiber dispersion may also be quantified via the group velocity dispersion (GVD) parameter β_2 given by

$$\beta_2 = \frac{d^2\beta}{d\omega^2} \ . \tag{2.17}$$

The dispersion of a fiber or the round-trip dispersion of a resonator are important system parameters that need to be carefully considered in the design of, e.g., ultrashort pulsed light sources. Fiber dispersion may not only cause pulse broadening by delaying the spectral phases with respect to each other, but plays a key role together with nonlinear effects for the pulse formation in a mode-locked fiber laser ([18, 24, 107]) or for supercontinuum generation creating ultra-broad spectral light sources ([37, 65, 150]). Depending on the sign of D_λ, two regimes are classified: $D_\lambda < 0$ denotes normal dispersion and $D_\lambda > 0$ labels anomalous dispersion. In each regime, different effects in pulse formation may occur.

The freedom in fiber design, i.e. the waveguide geometry and to some extent also the material selection, provides a powerful framework to engineer and control the fiber dispersion for specific applications. This process is mainly driven by numerical simulations, but experimental verifications of the fiber design may provide important feedback for the design of mode-locked lasers or supercontinuum light sources, generating ultra-wide band emission spectra by nonlinear broadening of laser pulses. Thus, the measurement of the fiber dispersion or even of the round-trip dispersion in a resonator is beneficial for the development of enhanced fiber-based light sources (see section 4.1).

2.2 Fiber Bragg gratings (FBGs)

Fiber Bragg gratings (FBGs) as fiber-integrated narrow band reflectors are the key element of the studied tuning concept. The following section provides a basic overview over their fundamental properties as well as common fabrication techniques. Further reading is provided in literature, e.g. [78].

2.2.1 Principle structure

An FBG denotes a periodic modulation of the refractive index n along the propagation axis of an optical fiber. The imprinted perturbations can establish distinct coupling between specific modes transferring energy to different propagation states. Thus, FBGs are a key technology for advanced all-fiber networks. They provide a powerful platform for integrating tailored functionality into optical fibers. These features open up a broad range of applications, most notably in optical communications, fiber lasers and sensing [70].

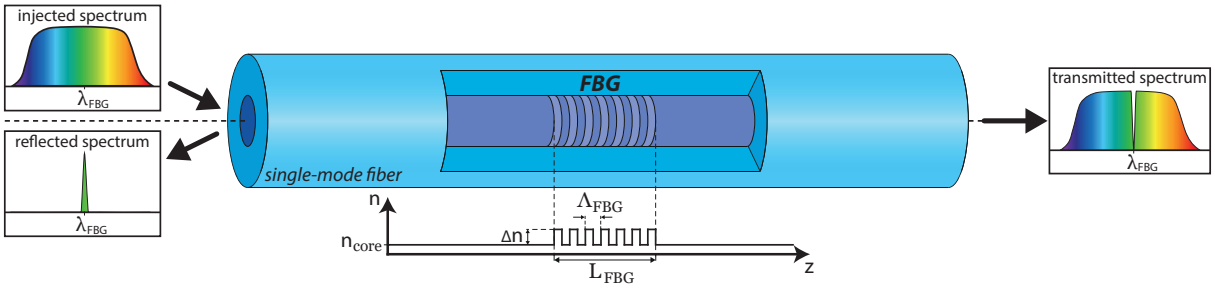

Fig. 2.2: Principle structure of a uniform FBG as narrowband reflector inscribed into a single-mode fiber. It comprises a periodic refractive index modulation in the core of modulation depth Δn with period Λ_{FBG} as sketched in the graph. For a broadband signal injected into the fiber, this periodic structure causes mode coupling, reflecting the wavelength λ_{FBG} while the rest of the spectrum transmits nearly unperturbed.

The principle structure of an FBG is illustrated in Fig. 2.2 picturing the scenario of a reflection grating included into a SM fiber core. The uniform FBG comprises a square modulation of the refractive index n with modulation depth Δn and period Λ_{FBG} that extends over the grating length L_{FBG}. The effect of this structure on a signal with a broadband spectrum injected into the fiber is schematically visualized in the three boxes. The signal propagates through the fiber and gets perturbed by the periodic index modulation in the grating region causing successive weak reflections at each interface of an index variation. The reflected light fractions follow

an interference behavior. Only for a particular wavelength λ_{FBG}, they add up constructively backwards over the grating length inducing efficient energy coupling to the counter-propagating mode. Accordingly, the spectral region around λ_{FBG} is reflected by the FBG as depicted by the green peak in the reflected spectrum of Fig. 2.2. Surrounding spectral components experience destructive interference and transmit with negligible loss through the grating region. Consequently, the FBG acts as a monolithic narrowband reflector for the wavelength λ_{FBG}.

In a formal description, the perturbation of the index grating induces a local deviation of the effective mode index $\Delta n_{eff}(z)$ modeled by

$$\Delta n_{eff}(z) = \overline{\Delta n_{eff}}(z) \left[1 + \nu \cdot \cos\left(\frac{2\pi}{\Lambda_{FBG}} z + \phi(z)\right)\right] \tag{2.18}$$

for a cosinusoidal modulation [38]. $\overline{\Delta n_{eff}}(z)$ is the mean index variation spatially averaged over a grating period and ν describes the modulation strength. The additional phase $\phi(z)$ covers local variations of the grating period Λ_{FBG} along z, which is defined as a chirped FBG and will be discussed more in detail in subsection 2.4.3.

A comprehensive formal treatment to calculate the spectral response characteristics of this structure involves coupled mode theory as discussed in several text books (e.g.: [78]). However, the condition for constructive coupling between different modes induced by the FBG can be analyzed analogous to the treatment of a diffraction grating [122]. Considering mode 1 and mode 2 with the respective propagation constant $\beta_{(1)}$ and $\beta_{(2)}$, the condition for efficient energy coupling is given by the grating equation as follows

$$\beta_{(2)} - \beta_{(1)} = m\frac{2\pi}{\Lambda_{FBG}} \ . \tag{2.19}$$

The propagation direction of each mode is considered via the sign of $\beta_{(1)}$ and $\beta_{(2)}$ with negative values labeling backwards propagation. The integer m denotes the diffraction order. A second essential condition for mode coupling requires spatial overlap of the two modes and the induced index modulation area. If both conditions are satisfied, energy is transferred.

Incorporating equation(2.9), equation(2.19) can be rewritten for the plain scenario of a reflection grating in a SM fiber as depicted in Fig. 2.2. The energy coupling to the counter-propagating mode is governed by the simplified grating equation

$$\lambda_{FBG} = 2n_{eff}\Lambda_{FBG} \ , \tag{2.20}$$

in first order considering retroreflection. λ_{FBG} represents the feedback wavelength or Bragg wavelength of the FBG.

Equation(2.20) reveals the direct connection between the grating period and the corresponding feedback wavelength. This link is the basis for a wide application field of FBGs as sensors. Any environmental influence that temporally alters Λ_{FBG} (or n_{eff}) can be monitored by a simple optical measurement of λ_{FBG}. Hence, FBGs are widely employed as e.g. strain sensors, temperature sensors, or recently even as real-time shape sensors with stacked FBGs in multi-core fibers [86, 106, 116]. Reversing this principle, the feedback wavelength of the grating

might be actively controlled and tuned by varying temperature or strain. As will be discussed subsection 2.4.3, this is beneficial for fiber-integrated lasers enabling stabilized or plain tunable sources.

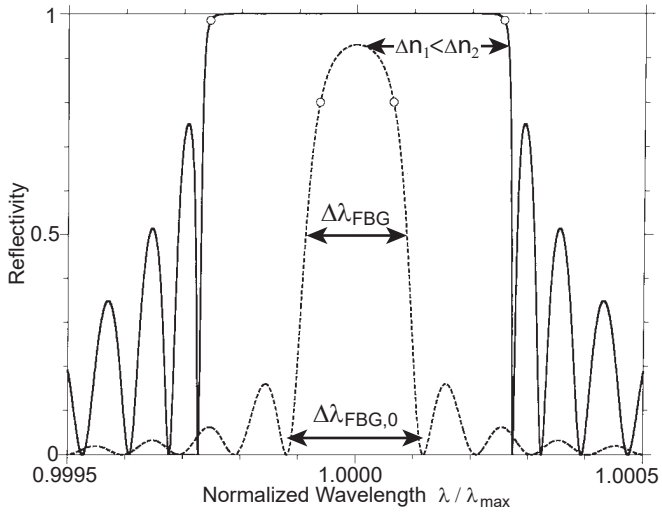

Fig. 2.3: Calculated reflection spectra of a uniform FBG for two different gratings strengths $\Delta n_1 < \Delta n_2$ [38].

A simulated reflection spectrum of a uniform FBG ($\overline{\Delta n_{eff}}(z) = \overline{\Delta n_{eff}}$) is shown in Fig. 2.3. The traces represent two different grating strengths symbolized by the index modulation amplitudes $\Delta n_1 < \Delta n_2$. Both traces have a strong central feedback peak that is accompanied by decaying side lobes to both sides. These distortions arise from the uniformity and limited length of the analyzed grating and can be suppressed with a specifically apodized FBG, i.e. a locally changing grating strength $\overline{\Delta n_{eff}}(z)$ following an envelope function. Advantageously, most fabricated gratings show an inherent apodization due to the beam profile of the inscribing laser.

The traces in Fig. 2.3 also show that a stronger grating typically exhibits a higher peak reflectivity R and broader feedback width $\Delta\lambda_{FBG}$. Derived from the coupled mode theory analysis, the reflectivity of a uniform grating can be estimated by [70]

$$R = \tanh^2\left(\frac{\pi\nu\overline{\Delta n_{eff}}\Gamma}{\lambda_{FBG}} \cdot L_{FBG}\right) . \tag{2.21}$$

Accordingly, at a fixed wavelength λ_{FBG} , the reflectivity grows with greater index modulation $\overline{\Delta n_{eff}}$ (stronger interaction) and longer FBG lengths L_{FBG} (more grating periods to interact with). The modal overlap with the grating region is considered by the factor Γ. As an example, a moderate index modulation depth of $\nu\overline{\Delta n_{eff}} = 5 \cdot 10^{-5}$ at a wavelength $\lambda_{FBG} = 1060\,nm$ with an effective FBG length of $L_{FBG} = 1\,cm$ results in a peak reflectivity of around 81%. Common inscription methods usually achieve highly reflective FBGs with R close to 100%, i.e. transmission losses at λ_{FBG} exceeding $30\,dB$.

Fig. 2.3 also indicates different feedback bandwidth $\Delta\lambda_{FBG}$ (full width at half maximum, FWHM) for the two exemplary gratings, which is another characteristic parameter of an FBG. In a similar way as for R, the bandwidth can be estimated based on the coupled mode theory analysis. An analytical expression can be retrieved for the separation $\Delta\lambda_{FBG,0}$ of the first zeros to either side of the main reflection peak by [38]

$$\Delta\lambda_{FBG,0} = 2\nu\overline{\Delta n_{eff}}\Lambda_{FBG}\sqrt{1 + \left(\frac{2n_{eff}\Lambda_{FBG}}{\nu\overline{\Delta n_{eff}}L_{FBG}}\right)^2} . \tag{2.22}$$

This relation holds as an upper limit of the FWHM $\Delta\lambda_{FBG}$ of a uniform FBG. In the regime of a weak-grating approximation, i.e. $\nu\overline{\Delta n_{eff}} \ll \lambda_{FBG}/L_{FBG}$, this simplifies to

$$\Delta\lambda_{FBG,0} \approx \frac{\lambda_{FBG}^2}{n_{eff} \cdot L_{FBG}} \ . \tag{2.23}$$

More handy to measure is the FWHM that can be estimated in this regime via a factor of 1/2 [119]:

$$\Delta\lambda_{FBG} \approx \frac{\lambda_{FBG}^2}{2 \cdot n_{eff} \cdot L_{FBG}} \ . \tag{2.24}$$

Accordingly, narrow reflection bandwidths are achieved for rather long gratings (in the weak-grating regime). With a typical grating length of $1\,cm$, the bandwidth at $\lambda_{FBG} = 1060nm$ is estimated to $\Delta\lambda_{FBG} \approx 40\,pm$ ($n_{eff} \approx 1.45$ for a silica fiber). The narrowest bandwidth reported in literature measures about $2.5\,pm$ based on a $1\,m$ long FBG [46]. Such scaling of the grating length is feasible due to elaborate technological efforts enabling an actively controlled phase correction of the inscription to consider fiber inhomogeneities and to avoid phase errors (stitching errors) [97].

Extended grating bandwidths are achieved in the strong-grating limit, i.e. $\nu\overline{\Delta n_{eff}} \gg \lambda_{FBG}/L_{FBG}$. The grating width can be approximated to

$$\Delta\lambda_{FBG,0} \approx 2\nu\overline{\Delta n_{eff}}\Lambda_{FBG} \ . \tag{2.25}$$

Strong modulation amplitudes of the refractive index grating are necessary. In this regime, the impact of the grating length is negligible on the bandwidth since the light does not penetrate the full length of the FBG. As an alternative, chirped gratings offer extended feedback bandwidths due to a locally changing Λ_{FBG} as will be discussed in subsection 2.4.3.

Based on the monolithic design, FBGs inherently preserve the advantages of an all-fiber network with an enclosed signal path featuring particularly ultra-low insertion losses (IL), compact size and robust operation. Besides working as a plain reflection grating, the design flexibility of FBGs enables access to a variety of applications. With adapted grating periods, equation(2.19) also implies the feasibility of general mode converters. Accordingly, a tailored FBG can couple light to any mode propagating in the fiber, specifically also in forward direction, which is referred to as long-period transmission grating [136]. Another example is given by a chirped grating structure with a tailored distribution of the grating period Λ_{FBG} along z that qualifies as a dispersion compensator for pulse shortening or stretching balancing the spectral phase delay of an ultrashort laser pulse [48].

2.2.2 Inscription methods

Even though, the first FBG was accidentally inscribed by a blue laser beam propagating along the fiber axis and forming an interference pattern with an end-facet reflection [69], common inscription techniques rely on a much more flexible side illumination of the fiber imprinting the periodic index modulation. The different approaches differ regarding the wavelength and pulse duration of the illuminating laser as well as regarding the generation of the index pattern.

A post-hoc modification of the refractive index in a fiber is usually caused by the photorefractive effect [58]. A material that is photosensitive in the UV range exhibits a permanent refractive index change when exposed to UV radiation (e.g. $\lambda = 244\,nm$). For glass, this effect can be introduced by special dopants, e.g. germanium or cerium, or by temporarily loading the fiber with hydrogen. The magnitude of the refractive index change Δn may reach values of 10^{-2} [70], but typically ranges between 10^{-5} and 10^{-3}.

Some applications require the use of specialty fibers that interdict the use of photosensitive materials. A solution allowing the inscription of FBGs in almost any transparent material is given by employing ultrashort pulse laser systems [137]. Operating at huge peak powers, they induce nonlinear photorefractive index changes by multi-photon absorption in the glass. Due to the nonlinear dependence on the inscribing field strength, this approach is technologically more challenging since it usually requires tight focusing and is more sensitive to misalignment.

For both approaches, the fabrication of FBGs usually utilizes a side illumination of the fiber. The idea is to imprint the periodic index modulation into the fiber following the intensity distribution of the inscribing laser beam. One approach works with a scanning point-by-point writing of each grating fringe [100]. However, due to the required positioning accuracy with FBG periods in the micron scale, this approach rather qualifies for long-period gratings [78].

In contrast, much more precision is achieved by generating the periodic grating fringes with an interference pattern illuminated with a coherent light source on the side of the fiber. This holographic inscription sets the state of the art and is widely employed in academia and industry.

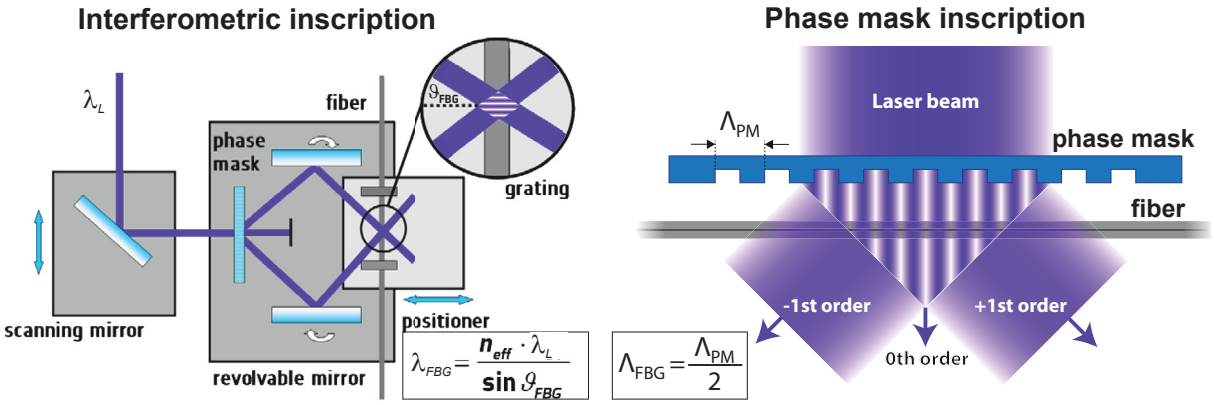

Fig. 2.4: Two principle setups are shown for the holographic inscription of FBGs. While the left hand side uses an interferometer formed by two mirrors to generate the periodic fringe pattern (modified from [94]), the right-hand side relies on a phase mask that utilizes the fringe pattern formed between the $+1$ and -1 diffraction order.

Fig. 2.4 illustrates the two principle setups, which are mostly applied. The left-hand side relies on a Mach-Zehnder-like interferometer formed by two mirrors and a phase mask to split up the beam to both interferometer arms [94]. The periodic fringe pattern is formed in the overlap region giving a 2-beam interference. The fringe period is determined by the beam angles ϑ_{FBG}, which can be tuned by the orientation of the revolvable mirrors. Accordingly, the inscribed grating period Λ_{FBG} can be variably modified during the fabrication procedure to easily tailor

the feedback wavelength λ_{FBG}. The length L_{FBG} of the grating correlates with the beam diameters.

In contrast, the scheme on the right-hand side in Fig. 2.4 relies on a phase mask technique forming the periodic fringe pattern in the overlap region between the +1 and −1 diffraction order [137]. Due to the walk-off effect, the 0^{th} order does usually not interfere for ultrashort pulses [138]. The imprinted period Λ_{FBG} is fixed by the phase mask period Λ_{PM}. While small tuning could be applied by preloading the fiber with, e.g., strain during inscription, different λ_{FBG} usually require the utilization of various costly phase masks. Lacking the spectral flexibility compared to an interferometric inscription, the laser beam can be scanned along the fiber and phase mask allowing longer grating lengths to be realized without phase errors [136]. Furthermore, the phase mask technique provides more stability for large scale production of a single grating wavelength than an interferometric setup.

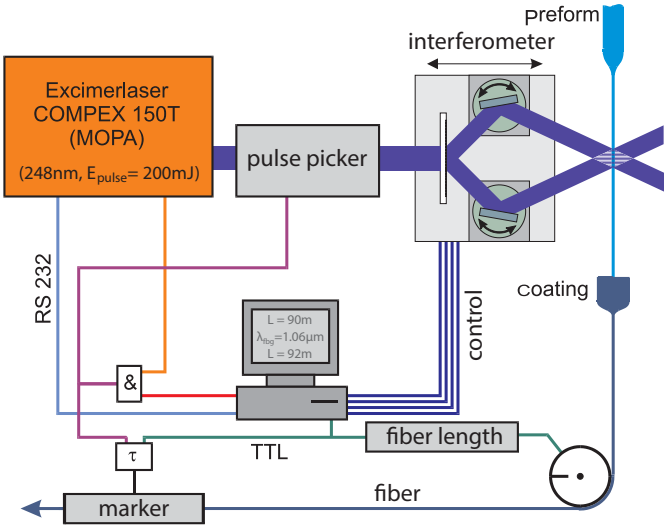

Fig. 2.5: Inscription setup of draw tower gratings during the fabrication process of the fiber with a ns pulsed UV laser. (Modified from [60])

Large scale production of FBGs with varying feedback wavelengths benefits from special fabrication concepts such as inscribing the grating directly during the fiber drawing process [9,31], using a spectrally flexible interferometric setup like depicted in Fig. 2.4. Such FBGs are also referred to as draw tower gratings (DTG). The principle idea of this concept is depicted in Fig. 2.5. The scheme shows a typical fiber drawing setup with a preform drawn to the target fiber diameter. Before the protective coating is applied, the fiber is side illuminated with a ns-pulsed UV laser beam passing through a flexible interferometric setup generating the fringe pattern.

Due to the dynamic drawing process with a continuously moving fiber, the inscription of each grating occurs with a single UV laser pulse limiting the reflectivity. With highly photosensitive fibers, feedback strengths R of more than 30% have been reported [23]. The pristine coating enables unspoiled mechanical robustness of the fiber, which is contrary for most other techniques where the fiber needs to be stripped from the protective coating weakening the fiber. This highly productive concept allows almost infinite numbers of gratings to be inscribed into the fiber with variably adaptable feedback wavelengths and thus provides unique benefits to produce large FBG arrays with broad bandwidths.

While DTG arrays are typically applied in quasi-distributed sensing applications of temperature or strain employing vast numbers of gratings [151], they have been also reported for spectral pulse analysis [145] and for discretely tunable fiber lasers as broadband monolithic filters [143, 149].

The FBGs underlying this work have been inscribed with the spectrally flexible interferometric approach to include gratings with steadily evolving feedback wavelengths stacked in FBG arrays.

They are fabricated with a fs-UV laser system based on the procedure depicted in [13], or with a ns-UV laser system as described in [23].

2.3 Fiber lasers

The principle aim of fiber lasers is to incorporate light amplification into the powerful architecture of optical fibers. The optical confinement of SM fibers combines an excellent nearly diffraction-limited output beam quality and low propagation losses with an enclosed geometry protecting the signal from environmental influences and enabling compact and robust setups. Thus, the fusion of the laser concept with the exceptional fiber architecture sets the benchmark for leading-edge industrial designs demanding user-friendly and low-maintenance systems as well as the feasibility for large scale production. On the other side, ongoing research programs utilize the huge design freedom to incorporate novel features in tailored geometries [129].

An overview about the principles and recent trends in fiber lasers in provided in several text books (e.g. [32, 132]).

In the following, the fundamental design concepts of fiber lasers are briefly introduced. In the context of tunable lasers, general material properties of gain media are presented focusing on the broadening mechanisms that enable enhanced spectral operation windows. In the last part, the effective gain bandwidth of Yb-doped aluminosilicate as a typical gain material in fiber lasers is exemplarily discussed aiming for design conclusions towards enhanced tuning ranges.

2.3.1 Design principles

The laser concept encompasses three fundamental elements: the gain medium with the active laser particles, a pumping mechanism to generate a population inversion in the active medium, and the resonator providing feedback to form a powerful laser signal over multiple passes through the active medium. Each of those elements follow distinctive design principles depending on the diverse laser types. Arising from the unique framework of waveguide structures, the main design concepts of fiber lasers are presented hereafter.

In principle, fiber lasers may operate with single-mode or multi-mode waveguide designs. While the latter potentially offers reduced nonlinear distortions and higher output powers, laser fibers mostly target the single-mode regime by working with smaller core sizes and low NA joining all the advantages of the fiber architecture. This especially includes excellent beam quality and superb brightness.

The gain medium is realized by the active fiber. It typically incorporates active laser dopants in the core region to generate optical amplification (compare to Fig. 2.1). As will be further discussed in subsection 2.3.2, the composition of the gain material determines the major properties including particularly the spectral operation window. Given by the active dopants, the most popular operation ranges are around $1\,\mu m$ (Ytterbium doping), $1.5\,\mu m$ (Erbium doping) or $1.9\,\mu m$ (Thulium doping). However, the emission range is also influenced by the pumping configuration.

Fiber lasers are typically pumped optically with the pump wavelength overlapping the distinctive spectral absorption regions of the active dopants. Fiber-coupled laser diodes depict highly efficient and cost-effective pump sources at various wavelengths covering even high powers in the kW regime. Based on the waveguide structure of fiber lasers, the gain medium is usually end-pumped with the pump light propagating along the fiber axis. Accordingly, the active fiber length provides design freedom to adjust the effective absorption strength of the gain medium ensuring high pump efficiency.

Two pumping geometries are common. For core pumping, the pump light is directly injected into the core that also guides the laser signal. While this concept enables short interaction lengths with strongest pump absorption and rather high population inversions, it puts severe constraints on the brightness of the pump source limiting the available power for single-mode fibers. In the case of cladding pumping, the light is injected into the cladding that operates as a multi-mode pump core surrounding the signal core. This scenario is sketched in Fig. 2.6 showing an active double-clad fiber with an FBG as a reflector in the signal core to form a plain laser. To guide pump and signal light, the refractive indices in a double-clad fiber are connected by $n_{clad2} < n_{clad} < n_{core}$ with n_{clad2} belonging to the outer cladding confining the pump core. Depending on the fractional overlap with the absorbing signal core region, the pump light is

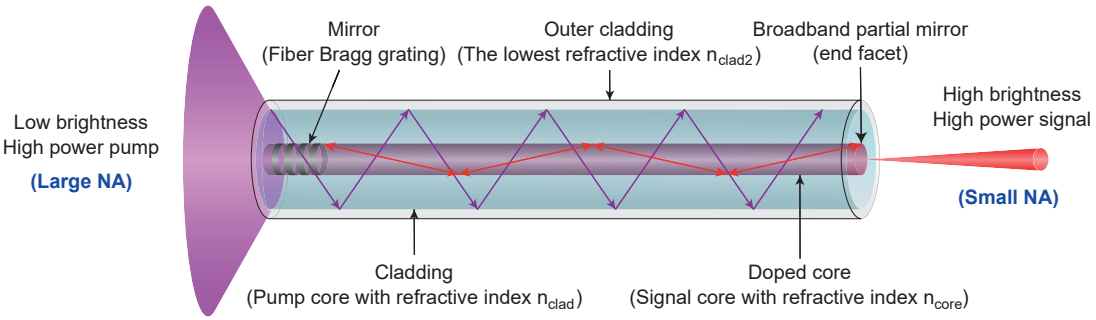

Fig. 2.6: The sketch illustrates the cladding pumping scheme for the plain case of a double-clad fiber laser formed by an FBG in the core and the feedback from the fiber end facet on the right-hand side. (Modified from [5])

gradually absorbed along the fiber inducing longer interaction lengths and rather low population inversions. Often, mode-scrambling techniques, such as asymmetric cladding geometries [56] or distinctive fiber bending [160], are applied to ensure an optimized overlap between the pump light and the doped core along the fiber. With the decoupled relation between pump and signal beam quality, the double-clad fiber geometry acts as brightness converter with an enhancement of up to 6 orders of magnitude [117]. This concept enables the use of low-brightness high-power pump diodes with multi-mode fiber coupling to generate high brightness high power laser signals with unprecedented beam quality emitted from the single-mode core.

The last key element of the fiber laser is the resonator, which utilizes the stimulated emission process by circulating the signal light over multiple round trips. Additionally, the cavity geometry may incorporate various functionalities to tailor the laser output characteristics. This particularly includes e.g. modulators for pulsed emission as well as spectral filters for stabilized or tunable laser wavelengths. With typically high single-pass gain provided by the active fiber

due to long interaction lengths, cavity layouts with high round-trip losses exceeding 20 dB are feasible.

For fiber lasers, the resonator might be free-space coupled or fiber-integrated. The former provides more flexibility for high output powers or enhanced emission characteristics using bulk optical components that are hardly to be incorporated into a fiber. On the other side, fiber-integrated lasers fully benefit from the unique advantages of all-fiber networks. They enable robust systems with alignment-free and user-friendly operation, sealed beam paths, low maintenance requirements as well as small footprint setting the benchmark for leading-edge laser solutions in industry and life sciences. Hence, application-oriented research often targets the transfer of a laser concept to all-fiber designs.

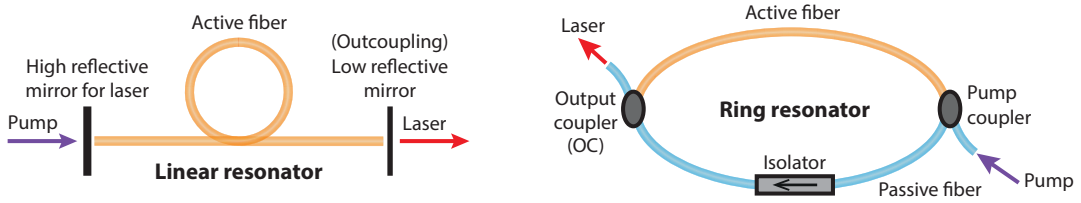

Fig. 2.7: The sketch illustrates the principle schemes of a linear fiber laser cavity (left-hand side) and a fiber ring resonator (right-hand side). Using an optical isolator, a ring resonator may feature unidirectional operation.

In general, laser cavities are classified in linear resonators and ring resonators. As depicted on the left-hand side in Fig. 2.7, a linear resonator is usually formed by two end mirrors circulating the signal back and forth. The mirrors may be realized by bulk optics, end-facet feedback or incorporated into the fiber by FBGs as depicted in Fig. 2.6. This Fabry-Pérot style cavity supports longitudinal modes that form standing wave patterns with local intensity maxima, which may cause spatial hole burning in the gain medium. The right-hand side in Fig. 2.7 illustrates a fiber ring resonator. Without end mirrors in the cavity, light circulates in a loop in two possible directions. With a discriminating element like an optical isolator, unidirectional operation is possible. In contrast to a linear cavity, the signal passes optical components along the resonator loop only once per round trip.

2.3.2 Spectral properties of gain media

The gain medium of lasers typically comprises the active laser elements and the host material. While the active laser elements frame the spectral emission region based on their energy level structure, the host material defines the environment for their operation. This requires not only a sufficiently high solubility of the laser-active elements, but also involves e.g. suitable thermal, mechanical and optical properties as well as a good processability. Depending on the application, crystals or glasses are usually employed as host of solid-state lasers [112]. The active laser elements are mainly trivalent rare-earth ions from the lanthanides, such as Ytterbium (Yb), Erbium (Er) or Thulium (Tm). They combine the electronic configuration of Xenon with a gradually filled 4f shell determining the main optical properties.

While elaborate models are found in literature (e.g. [30]), Yb^{3+}, featuring a simple energetic structure, is well suited for an exemplary discussion of the fundamental effects. It comprises a two-level system with the energy states $^2F_{5/2}$ and $^2F_{7/2}$ as sketched in Fig. 2.8. Implementing Yb^{3+} into a host lattice, each level splits up in a sublevel structure due to the Stark effect caused by the local electric fields. This broadening results in quasi 3-level or even 4-level energetic configurations suitable for laser transitions in the visible and near-infrared. In the case of a crystalline host, the periodic structure creates steady fields along the lattice giving discrete sublevels with sharp transition lines as indicated in Fig. 2.8. In contrast, the disordered lattice of amorphous glass hosts causes locally varying electric fields resulting in strongly broadened sublevels and continuous energy bands due to the Stark effect.

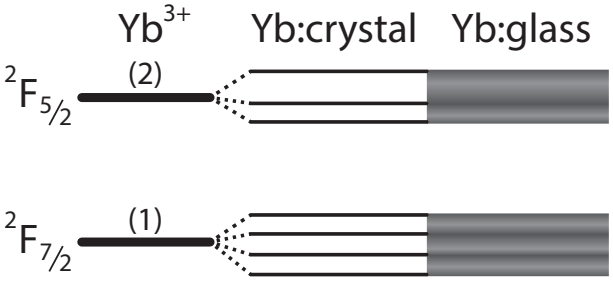

Fig. 2.8: Schematic energy band structure of Yb depending on its environment. Due to the Stark effect, the 2-level structure of the ion splits up in discrete sublevels (crystal host) or continuous energy bands (glass host).

In general, the spectral transition line broadening of a laser medium is categorized in homogeneous or inhomogeneous broadening. For the first case, each active particle is equally affected by the broadening effect resulting in identical emission properties and uniform saturation of the overall spectral gain. The latter group features a macroscopically broadened linewidth that emerges from a superposition of various ensembles of active particles with detuned transition lines. Consequently, the spectral gain at one wavelength may be depleted by a signal while neighboring spectral regions still provide unperturbed amplification. This results in an inhomogeneous saturation of the gain spectrum. In the case of Yb-doped glasses, the line broadening by Stark splitting combined with thermal relaxations is mainly driven homogeneously and thus less sensitive to parasitic emission wavelengths.

As a conclusion, Yb-doped glass exhibits broad continuous transition regimes that feature extended spectral operation windows with potential optical gain for lasing, such as required for tunable lasers. This is combined with the typically broad temporal processing window of glasses which is essential for fiber drawing [133]. Accordingly, rare-earth doped glasses provide a powerful foundation for tunable fiber lasers as targeted in this work.

2.3.3 Potential gain bandwidth of Yb-doped aluminosilicate fibers

Yb-doped aluminosilicate depicts a widely employed gain medium in fiber lasers that is also used in this experimental study. Silica is well known as glassformer joining numerous beneficial properties, including very low optical losses with a broad transparency window from the ultraviolet (UV) to the infrared (IR), high mechanical and chemical robustness, low price due to abundant raw material and high thermal resistance combined with a wide processing window. It is co-doped with aluminum as a network modifier forming the host material aluminosilicate. Yb as the laser active element exhibits a simple 2-level band structure enabling high efficiencies due to a low quantum defect and excluded detrimental effects (e.g. excited state absorption).

Combined with the typically broad gain regions, Yb-doped systems set the benchmark for high power and ultrashort pulsed fiber lasers in industry and research [40, 63, 93, 147].

In the following, the gain characteristics are modeled for an exemplary system that closely relates to the developed laser concept in this study. The discussion aims for conclusions regarding the optimum gain bandwidth restricting the potential spectral tuning range. For a comprehensive treatment of the gain characteristics, the reader is refereed to more extensive studies in literature (e.g. [11, 19, 30, 52, 113]).

A simple model of Yb-doped aluminosilicate can be derived from a 2-level system assuming homogenous broadening [29] and neglecting amplified spontaneous emission (ASE) as well as nonlinear, thermal and saturation effects valid for low power levels [113]. The two energy manifolds $^2F_{7/2}$ and $^2F_{5/2}$ are described by the population densities N_1 and N_2, respectively. The evolution of power P along the propagation direction z in the active fiber can be described with the differential equation [113]

$$\frac{dP}{dz} = g(\lambda)P(z) \tag{2.26}$$

with λ denoting the wavelength and $g(\lambda)$ as the effective spectral gain coefficient that, for simplicity, is assumed to be constant along the z-direction. The solution is described by an exponential growth given by

$$P(z) = P(z=0)\ e^{g(\lambda)z} \tag{2.27}$$

The effective amplification spectrum depicted by $g(\lambda)$ is a linear combination of the ground-state ($^2F_{7/2}$) absorption and excited-state ($^2F_{5/2}$) emission cross-section spectra σ_a and σ_e weighted by the corresponding population densities N_1 and N_2 giving

$$g(\lambda) = \Gamma[\sigma_e(\lambda)N_2 - \sigma_a(\lambda)N_1] \tag{2.28}$$

The parameter Γ depicts a normalized overlap integral factor taking into account the intensity overlap between the transversal mode in the fiber and the active Yb-doped core region [52].

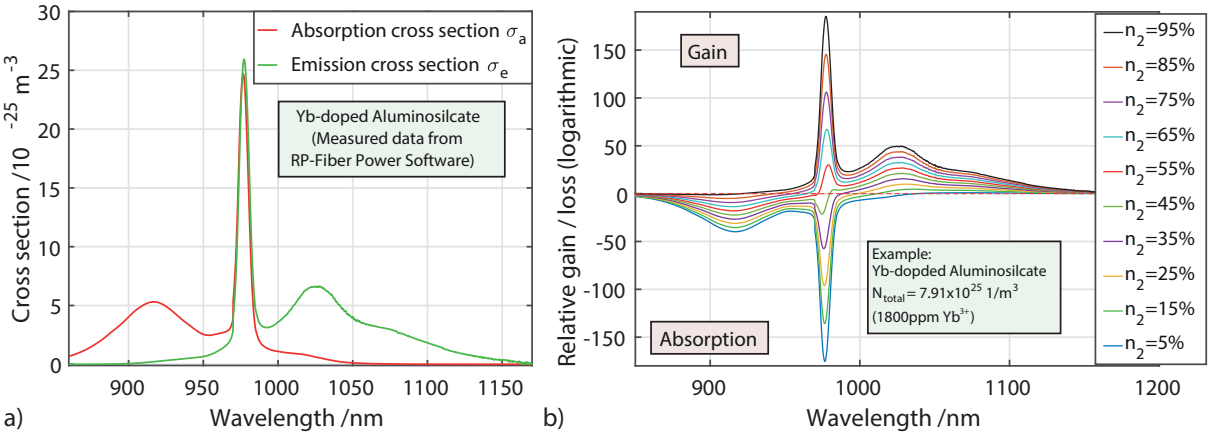

Fig. 2.9: Graph a) plots the emission and absorption cross-section spectra of a typical Yb-doped glass based on aluminosilicate (raw data provided by the commercial software *RP Fiber Power*). Graph b) plots the calculated relative gain spectra for Yb-doped aluminosilicate. Considering varying population inversions n_2, positive values relate to net amplification while negative sections correspond to absorption.

Graph a) in Fig. 2.9 plots measured absorption and emission cross-section spectra σ_a and σ_e of Yb-doped aluminosilicate provided by the commercial software *RP Fiber Power*. The absorption cross section is characterized by a broad peak around 915 nm and a narrow peak around 976 nm with an about 4 times stronger absorption. While both wavelengths are widely used for pumping such lasers, pumping at 976 nm usually needs the pump source to be spectrally stabilized due to the narrow absorption line. The emission cross section σ_e exhibits the same strong peak at 976 nm. In literature, it is usually normalized to the amplitude of σ_a at 976 nm because absolute values are difficult to acquire in the overlap region [113]. The emission cross section σ_e features another peak around 1030 nm that broadly extends even beyond 1100 nm. This frames the typical working window of Yb-doped fiber (YDF) lasers.

From this characteristic behavior in σ_a and σ_e, a few simple conclusions can be drawn. Only dissimilar spectral shapes in σ_a and σ_e driven by the Stark splitting enable the generation of gain in this plain 2-level system. The absorption line extends even in the region of a strong emission cross section beyond 1000 nm resulting in a quasi 3-level behavior of the gain medium including reabsorption effects of the laser signal. For longer signal wavelengths towards 1100 nm, ground state absorption vanishes transferring the gain characteristics effectively to a 4-level laser system in which even low population inversions generate net amplification. Furthermore, assuming matched peak amplitudes of σ_a and σ_e, pumping at 976 nm limits the population inversion to $N_1 \geq N_2$.

Further insights are given by employing normalized population densities n_j based on the total dopant density N_{total} of Yb:

$$n_j = \frac{N_j}{N_{total}}, \sum_{j=1,2} N_j = N_{total}. \tag{2.29}$$

Accordingly, equation(2.28) can be written as

$$g(\lambda) = \Gamma N_{total}[\sigma_e(\lambda)n_2 - \sigma_a(\lambda)n_1] \tag{2.30}$$

Deducing $n_1 + n_2 = 1$ from equation(2.29), n_1 can be eliminated resulting in

$$g(\lambda) = \Gamma N_{total}[n_2(\sigma_e(\lambda) + \sigma_a(\lambda)) - \sigma_a(\lambda)] \tag{2.31}$$

This represents a simple description with solely n_2 determining the effective amplification spectrum of a given gain medium. Graph b in Fig. 2.9 illustrates the resulting gain (positive values) and loss (negative values) spectra for a gradually changing population n_2 in level 2. The graph indicates low population levels, i.e. $n_2 = 5\,\%$, to exhibit a net absorption for wavelengths up to 1040 nm. Accordingly, due to the 3-level character, smaller wavelengths require elevated population inversions. The higher n_2, the more the net gain region shifts to shorter wavelengths. The turn over point from loss to gain at 976 nm is reached at $n_2 \approx 0.5$. In general, the net gain as well as the gain bandwidth increases towards larger population in n_2.

However, the practical operation bandwidth of the gain medium in a tunable laser resonator is also limited by e.g. significant amplitude differences in the amplification spectrum. In order to

estimate a practical dynamic amplification range and prevent gain configurations being prone to parasitic lasing at the strongest spectral amplification, equation(2.31) is rewritten to estimate the absolute gain of a given active medium configuration. The total gain factor G also depends on the interaction length L, i.e. the effective gain medium length. It follows the relation

$$G(\lambda) = g(\lambda)\ L = \Gamma\ N_{total}\ L\ [n_2(\sigma_e(\lambda) + \sigma_a(\lambda)) - \sigma_a(\lambda)] \tag{2.32}$$

This is converted from Neper scale to the more practical decibel (dB) scale by

$$G_{dB}(\lambda) = G(\lambda)\ \log_{10}(e) \approx 4.343\ \Gamma\ N_{total}\ L\ [n_2(\sigma_e(\lambda) + \sigma_a(\lambda)) - \sigma_a(\lambda)] \tag{2.33}$$

relating the estimated boost in output Power $P(z = L)$ compared to $P(z = 0)$.

An exemplary gain medium is chosen based on an Yb-doped aluminosilicate step-index fiber as it is used for some of the experimental investigations in this work. The fiber is doped with an Yb concentration of 1800 ppm (mol) ($N_{total} = 7.91 \cdot 10^{25}\ m^{-3}$). Core and cladding diameters are specified with $d_{core} = 7.1\ \mu m$ and $d_{clad} = 125\ \mu m$. The NA is given by 0.12. Γ is calculated by a modal analysis with the software *COMSOL Multiphysics* (see also subsection 4.1.3) yielding a modal core overlap of about 0.84 at 1060 nm (spectral dependencies are neglected).

For a practical analysis, the peak gain factor $G_{dB,max}$ is normalized to 30 dB allowing different populations in n_2 to be compared with respect to the accessible amplification bandwidth. 30 dB represents a typical gain value achieved in a low-power laser oscillator and stays within the limits allowing ASE effects to be neglected [113]. The normalization is realized by adapting the fiber length L to an effective value L_{eff} for each n_2 ensuring $G_{dB}(\lambda) \leq 30dB$.

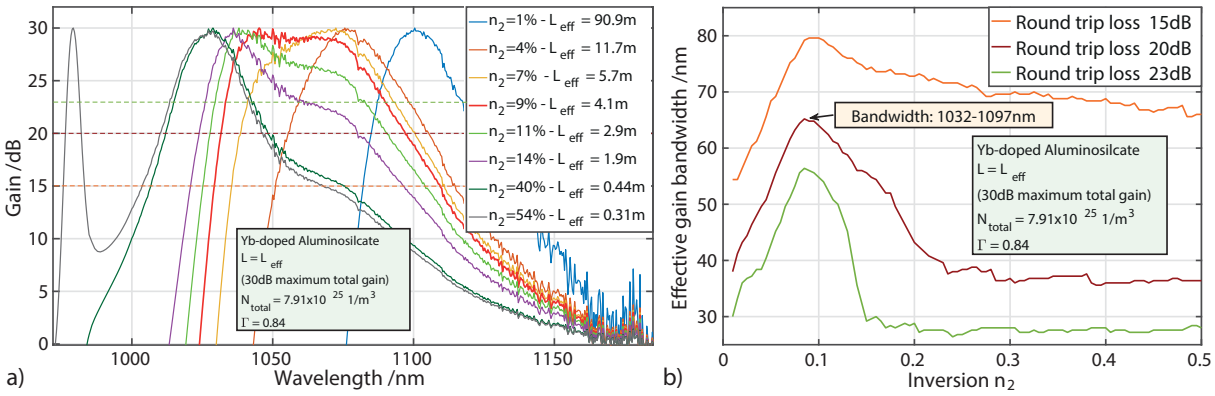

Fig. 2.10: Modeling a typical Yb-doped aluminosilicate fiber (Yb^{3+} concentration: 1800 ppm mol) as gain medium, graph a) plots absolute gain spectra depending on the population inversion n_2. The traces are normalized via the active fiber length L_{eff} to a typical system peak gain of 30 dB, respectively. Graph b) plots the corresponding effective gain bandwidth considering three exemplary round-trip losses of the laser resonator that have to be compensated by the amplification of the active fiber. The longest continuous gain bandwidth could be expected for population inversions around $n_2 \approx 0.09$. Considering resonator round-trip losses of about 20 dB, a maximum tuning range from 1032 nm to 1097 nm could be feasible.

Graph a) in Fig. 2.10 shows the absolute gain spectra of the modeled configuration for varying populations n_2, which are assumed homogenous along the fiber length. L_{eff} progressively increases for decreasing n_2 to establish 30 dB of peak gain in each case.

The graph highlights the gradual blue shift in the amplification regime for growing population inversion. At $n_2 \approx 0.09$, the trace exhibits a broad peak plateau from $1040\,nm$ to $1075\,nm$ ensuring steady gain over a broad range. The dark gray curve highlights the strong inversion regime in n_2 beyond 0.5. It features two characteristic peaks at around $976\,nm$ and $1030\,nm$ separated by a low gain window.

In order to estimate the accessible gain bandwidth for laser operations in a resonator, the round-trip losses of the signal need to be considered, which have to be compensated by the active medium. Losses originate from the other cavity components, e.g. the output coupler, spectral filter, modulator and splices. The dashed lines in graph a) of Fig. 2.10 indicate three exemplary threshold levels at $15\,dB$, $20\,dB$ and $23\,dB$ that are reasonable for the resonator design developed in this work. Accordingly, high population inversions beyond 0.5 as highlighted by the dark gray trace would have two separated operation windows with a broad range around $990\,nm$ where no lasing could be established. For a broad continuous tuning window of the laser wavelength in the chosen configuration, this regime is unsuitable.

Graph b) in Fig. 2.10 plots the calculated effective gain bandwidths over n_2 for the corresponding three round-trip loss levels. In each scenario, the exploitable net amplification bandwidth is maximized between $n_2 = 0.08$ and $n_2 = 0.10$. In the case of $20\,dB$ round-trip losses, a spectral tuning bandwidth over $65\,nm$ ranging from $1032\,nm$ to $1097\,nm$ could be feasible.

In conclusion, the design of the tunable laser should target an operation regime with rather low population inversion n_2 between 0.07 and 0.11 for a maximized bandwidth. The inversion can be mainly adjusted via the pump configuration, pump wavelength, power level as well as the fiber design. For a typical Yb-doped single-mode fiber, cladding-pumped configurations are usually characterized by low n_2 and extended fiber lengths $L > 1\,m$ as suggested by this principle analysis. Hence this scheme will be chosen for the experimental implementation.

2.4 Tuning concepts for fiber lasers

Tunable lasers are characterized by an adjustable emission wavelength λ_L. In principle, there are two approaches to modify the effective spectral gain maximum in the resonator determining λ_L. Either the gain medium is manipulated to alter the amplification spectrum, or an adjustable spectral filter is incorporated into the cavity applying frequency-selective losses to promote a specific wavelength for lasing. While the first approach is only applied for some gain media, e.g. diode lasers, where λ_L can be tuned by changing the temperature or pump current, spectral filters provide a much higher flexibility. They may access even remote spectral gain regions maximizing the potential tuning range for any laser concept.

Tunable fiber lasers typically use spectral filters to control λ_L. In literature, there is a whole zoo of different approaches that are reported for spectral filtering and tuning. In the following, the most common concepts are shortly introduced.

2.4.1 Bulk filters

Tunable bulk filters such as prisms and diffraction gratings have been intensively investigated for spectral tuning of fiber lasers some decades ago. With the free-space coupled beam path within the resonator, this geometry allows those filters to be utilized for any type of tunable laser. Hence, from semiconductor lasers, it is also more formally known as external-cavity feedback tuning.

Reflective diffraction gratings are the most prominent bulk filters, which are still widely utilized. Their characteristics are extensively covered in textbooks, e.g. [120]. For a grating period $\Lambda_{grating}$ as well as an incidence and diffraction angle of θ and θ', the spectral feedback wavelength λ in the m^{th} order is described by the grating equation

$$m\lambda = \Lambda_{grating}(sin\theta \pm sin\theta') \ . \tag{2.34}$$

Accordingly, by adapting $\Lambda_{grating}$, the beam geometry or the operation order, diffraction gratings provide a high flexibility to tailor the spectral properties. Continuous wavelength tuning is realized by changing θ and θ'. Often, gratings are blazed to maximize the diffraction efficiency in the operating order and minimize IL.

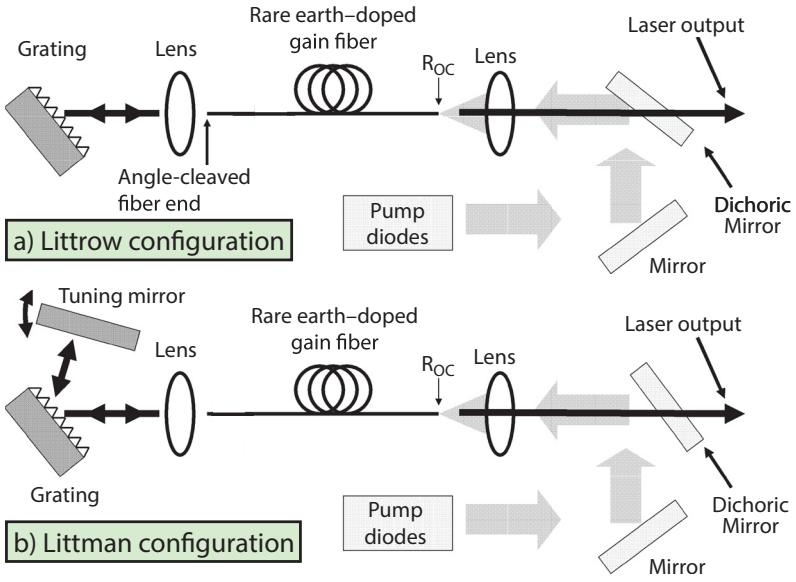

Fig. 2.11: Two widely employed configurations of tunable fiber lasers using diffraction gratings as spectral filter. Part a) illustrates the Littrow design where the incident and output angle are identical ($\theta = \theta'$). Sketch b) illustrates the Littman scheme (also referred to as Littman-Metcalf or grazing-incidence). The cavities comprise the free-space coupled diffraction gratings, lenses to couple and collimate the beam, rare-earth doped fibers as gain elements, an output coupler with reflectivity R_{OC} and dichroic mirrors to separate pump and signal light. [35]

For tunable fiber lasers, the free-space beam path has to be coupled to the optical fiber. As an example, Fig. 2.11 shows two widely employed geometries for diffraction gratings incorporated into a tunable fiber laser. In both schemes, the resonator is mainly build with bulk optics and only the gain element is fiber-based. A lens collimates the fiber output to the grating and couples the feedback signal back to the core. Fig. 2.11a) shows the Littrow configuration with a blazed grating. This simple configuration utilizes the grating directly as an end reflector,

which forms the cavity together with a rectangular cleave (reflectivity R_{OC}) of the active fiber on the other side. The light is retroreflected ($\theta = \theta'$) for a specific wavelength λ. Spectral tuning is based on rotating the grating changing the incidence beam angle $\theta = \theta'$ and giving a different feedback wavelength via equation(2.34). Based on the Littrow configuration, Nilsson et al. demonstrated a single-mode Yb fiber laser with a large tuning range of $73\,nm$ ranging from $1027\,nm$ to $1100\,nm$, a linewidth of $\Delta\lambda_{Laser} \approx 300pm$ and an output power of $2.8\,W$ [108].

Scheme b) in Fig. 2.11 shows the Littmann configuration. The blazed grating is operated under grazing incidence and uses an additional broadband end mirror to retroreflect the diffracted signal. Due to the second interaction with the spectral filter, this configuration tends to give a narrower spectral feedback width. Spectral tuning is achieved by tilting the broadband mirror altering the beam path. Using the Littman configuration, Fan et al. reported a tunable Yb-doped fiber laser [39]. Operating with a narrow linewidth of $\Delta\lambda_{Laser} = 40\,pm$, the Q-switched system covers a huge tuning range of $60\,nm$ from $1080\,nm$ to $1140\,nm$ with multi-mode emission.

While prism-based filters have not attracted lots of research interest over the past decades, they provide easy access to tunable lasers because only standard bulk optics is required. Additionally, the longest tuning range reported with an Yb-doped fiber laser has been achieved with prisms as spectral filters. Hannah et al. reported a vast tuning bandwidth of $152\,nm$ ranging from $1010\,nm$ to $1162\,nm$ [62]. The sensitive free-space coupling to the fiber core required the beam path to be realigned several times to cover the full tuning range.

In general, bulk filters provide good flexibility to adapt the filter characteristics to the requirements of the laser. Particularly diffraction gratings depict a versatile platform enabling large tuning ranges as well as narrow linewidths or high-power operation. However, incorporating bulk elements into a fiber network is compromised by diminishing main benefits of monolithic systems. This not only concerns a compact design and sealed beam paths, but mostly involves the lossy free-space coupling to the waveguide structure, which is sensitive to misalignment and environmental influences.

In contrast, superb robustness with high efficiency and low-maintenance requirements is mainly feasible with fiber-integrated solutions to meet the demands of industrial applications.

2.4.2 Fiberized filters

In order to meet the industrial demand for user-friendly filters that can be easily integrated into fiber networks, engineering efforts in miniaturization and packaging enabled fiberized filter devices. Free-space coupled filters are operated in a sealed package with connectorized interfaces or fiber pigtails for enhanced compatibility and stability. Fiberized tunable filters are commercialized by numerous companies, such as `Micron Optics Inc.`, `Santec Corporation`, `AGILTRON Inc.` or `Gooch & Housego`, using different filtering concepts.

Based on a fiberized diffraction grating, Li et al. realized a tunable all-fiber ring laser in the Tm band with a huge tuning range of $250\,nm$ [92]. The readily spliced filter is specified with a rather large bandwidth of $3\,nm$ (FWHM) and elevated IL of $3\,dB$.

In general, several physical effects can be exploited to realize a pigtailed spectral filter. A prominent example is given by a Fabry-Pérot resonator that uses the interference effects between two plane-parallel glass surfaces to generate distinctive spectral transmission peaks separated by reflection bands. The linewidth, free-spectral range (FSR) and signal contrast can be engineered by the width between the glass surfaces and their reflectivity. The physical principles are discussed in numerous textbooks, e.g. [12].

A pigtailed Fabry-Pérot filter is sketched in Fig. 2.12. The input signal is collimated by a lens, passes through an Etalon and is coupled to the output fiber. The transmission spectrum is tuned by rotating the etalon changing the effective thickness. The filter specifications are typically a tradeoff between linewidth and FSR, which sets the maximum tuning range. Corresponding IL are in the order of $1.5 - 2\,dB$. A tunable fiber laser with a Fabry-Pérot filter has been reported by Zyskind et al. [161]. A tuning range of $61\,nm$ has been achieved in the Er band with a filter FSR of $66\,nm$.

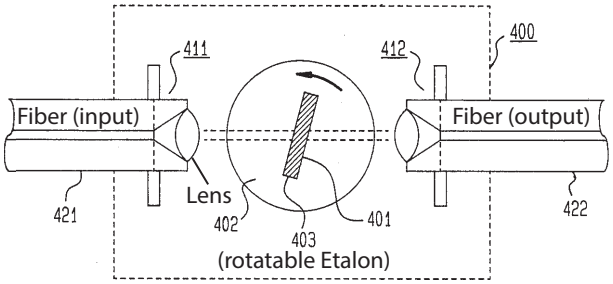

Fig. 2.12: Sketch of a tunable fiber Fabry-Pérot transmission filter with a rotatable Etalon (403) in a sealed housing (400). [44]

Another approach for a fiberized spectral filter utilized for tunable fiber lasers is given by acousto-optic tunable filters (AOTFs) [21]. The concept is based on an electric transducer that generates an acoustic wave in a crystal. The corresponding refractive index pattern diffracts a specific spectral region to the output fiber of the filter. The transmission wavelength can be tuned by the frequency of the acoustic wave. As an example, Yun et al. presented a wavelength swept fiber laser based on an AOTF with a tuning range of $38\,nm$ in the Er band [158].

Due to the commercial interest, fiberized tunable filters may be presented with a confidential design concealing the underlying physical concept. Using a black-box filter may cause artifacts in the tuning behavior which are hard to predict. As an example, Hideur et al. used such a filter from `Keopsys Inc.` in an Yb-doped fiber laser with a tuning range of $60\,nm$ [68]. The tuning range was only covered in discrete steps of $1\,nm$ which the authors supposedly contribute to polarization effects in the filter.

Nevertheless, fiberized tunable filters represent a good technological tradeoff between the functionality of free-space coupled filters and the compatibility with fiber optic networks. Due to the fiber interface, they can be readily spliced enabling fiber-integrated resonators without demanding beam alignment. Still, monolithic filter concepts can be superior in terms of compactness, robustness, user friendliness and IL as well as cost.

2.4.3 All-fiber filters

Aiming for an adjustable monolithic filter, any wavelength-discriminating as well as tunable loss effect in a fiber may be utilized to realize tunable lasers. One example is given by a fiber loop mirror build with fused fiber couplers. The principle is similar to a nonlinear-optical loop mirror known from mode-locked fiber lasers [33, 155]. The spectral sensitivity has been exploited by Li

et al. for a tunable Yb-doped laser [91] with a bandwidth of $20\,nm$. A mechanical polarization controller was used to control the wavelength-selective interferometer. Due to inherent adjacent filter lines, this approach often leads to multi-wavelength emission [127]. Another tuning approach is based on an acoustic horn generating an acoustic wave along a few mode fiber. Mode coupling induces spectral transmission lines that can be tuned by the resonance frequency. Kang et al. have demonstrated wavelength tuning over $48\,nm$ in the Erbium band [77]. Both concepts depict rather academic solutions that did not advance to industrial applications due to usability, manufacturing complexity and stability.

More established all-fiber tuning concepts are based on FBGs as narrowband reflectors inscribed in the core of the fiber (see section 2.2). As already indicated in equation(2.20), their feedback wavelength can be shifted by externally influencing the grating period Λ_{FBG} or n_{eff}. Such temporary modifications can be induced by temperature variations ΔT or strain ϵ. With an FBG as wavelength-selective element in the resonator, the emission wavelength of a laser can be tuned accordingly. Thus, a simplistic tunable all-fiber laser can already be realized by the design in Fig. 2.6. Modifying the temperature or bending the fiber at the FBG, which forms the resonator, induces a variation in λ_L.

In general, the shift $\delta\lambda_{FBG}$ of the feedback wavelength can be modeled by

$$\delta\lambda_{FBG} = \lambda_{FBG}\left[(1-p_e)\cdot\epsilon + \left(\alpha_{glass} + \frac{1}{n_{eff}}\cdot\frac{dn_{eff}}{dT}\right)\cdot\Delta T\right] \tag{2.35}$$

treating the impact of strain and temperature variations in a decoupled manner [79, 114]. It is connected to material properties by the strain-optic constant p_e and the thermal expansion coefficient of glass α_{glass}.

Based on the second term in equation(2.35), temperature variations induce two effects. While α_{glass} considers the weak expansion of the fiber with ΔT, the thermal drift in n_{eff} accounts for about 95% of the temperature induced shift in λ_{FBG} [79]. The combined temperature sensitivity of a standard grating is typically in the order of about $10\,pm/K$ [114]. Enhanced sensitivity can be realized by special coatings [57] or elaborate mounting setups [101] enabling extended tuning bandwidths of several tens of nanometers. In general, the thermal tuning range of an FBG is limited by the stability of the inscribed refractive index pattern. Depending on the fiber material and the inscription method, the working range may extend over several hundreds of kelvin before the grating bleaches out.

The impact of strain manifests in the first term of equation(2.35). Applying compressive or tensile forces induces a relative change of the fiber length physically modifying Λ_{FBG}. Common silica fibers with $p_e \approx 0.22$ show a spectral shift of about $1.0\,nm/mstrain$ at $\lambda_{FBG} = 1300\,nm$ [70]. The maximum tuning range is ultimately limited by the mechanical damage threshold of the fiber with the FBG. Whereas tensile forces are easier to apply by readily stretching the fiber, compression of FBGs potentially offers larger tuning ranges on the cost of more elaborate bending schemes. Silica principally exhibits a 23 times larger damage threshold for compressive forces [53]. By utilizing compression in an elaborate beam-bending technique, a maximum tuning range of an individual FBG is reported with $\delta\lambda_{FBG} = 110\,nm$ in the Er band [105].

Literature provides numerous examples of fiber lasers employing tunable FBGs to adjust λ_L. The longest tuning range has been reported by Akulov et al. reaching $45\,nm$ in the Yb band by mainly compressing the fiber [7]. Song et al. demonstrated even $40\,nm$ tuning range in the Er band with a stretched FBG treated for maximum strength [125]. A similar operation bandwidth of $41\,nm$ at $1550\,nm$ has been demonstrated by Guan et al. with a temperature tuned FBG that used a polymer package to translate temperature changes to strain variations [57].

FBGs provide an excellent basis to develop tunable lasers maintaining all the discussed benefits of all-fiber designs. They can be readily incorporated into monolithic setups by splicing or direct inscription into the active fiber allowing for low IL. Small emission linewidths are feasible with narrowband FBGs. Still, due to the sealed structure, λ_{FBG} can be only tuned by environmental influences. Both discussed methods, i.e. via temperature and strain, feature rather small tuning bandwidths with standard FBGs which cannot exhaust the potential gain bandwidth of rare-earth doped fibers to challenge other tunable sources. Additionally, both tuning mechanisms show limited usability based on either slow tuning (temperature tuned FBGs) or mechanically moving parts (strain tuned FBGs), which restrict the compactness and robustness of the laser.

Maintaining the key advantages of FBGs, dispersion-tuned pulsed lasers based on chirped FBG structures may potentially overcome the limitations. As mentioned in the discussion of equation(2.18), chirped FBG structures feature a spatially varying grating period $\Lambda_{FBG}(z)$ along the fiber axis considered by the phase term $\phi(z)$. Based on equation(2.20), this translates to a spatial dependence in the feedback wavelength $\lambda_{FBG}(z)$ covering in total an extended feedback spectrum. As illustrated in the green box of Fig. 2.13, corresponding filters are a continuously chirped FBG with a steady evolution of $\Lambda_{FBG}(z)$ along a single grating, or a discretely chirped (or step-chirped) FBG array comprising a stack of N standard gratings with a step-wise variation of the feedback wavelength (i^{th} grating: $\lambda_{FBG,i}$). Whereas continuously chirped FBGs are mostly applied to manage the dispersion in mode-locked all-fiber lasers [72,153], FBG arrays are typically employed in quasi-distributed sensing [79]. A small stack of FBGs with intermediate adjustable absorbers between each grating has been also used for wideband switchable lasers offering only a few wavelengths due to limited scalability [88].

The broadband filter feedback is utilized for widely tunable fiber lasers via dispersion tuning. Fig. 2.13 sketches a typical laser design to illustrate the concept of this tuning mechanism. The so called sigma-ring cavity comprises an output coupler (OC), the gain element (i.e. the active fiber), an amplitude modulator controlling the pulse repetition rate (PRR) $f_{PRR} = T_{MP}^{-1}$ via the modulation period T_{MP}, and the reflective FBG structure as spectral filter coupled by a circulator to the ring structure [149]. The distributed feedback of the chirped FBG filter is linked to wavelength-dependent filter response times $T_{filter}(\lambda_{FBG})$, which induce a structural cavity dispersion, i.e. a wavelength-dependent pulse round-trip time (PRTT) T_{RT} in the resonator. Accordingly, steady pulsed emission at different λ_L operates with dissimilar f_{PRR} [17,148,149]. The idea of dispersion tuning is to actively control the PRR for promoting a narrow spectral region out of the broadband filter response as effective feedback wavelength that determines the emission spectrum of the laser.

While this tuning approach may also be realized purely based on waveguide dispersion [20], determining the emission spectrum with a broadband FBG filter enables large tuning ranges

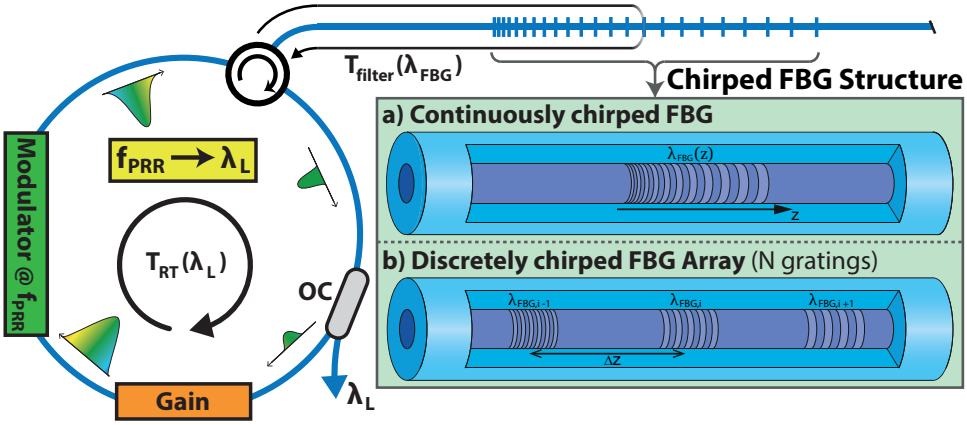

Fig. 2.13: Sketch of a dispersion tuned sigma-ring laser. The chirped FBG structure as broadband filter is implemented via a single continuously chirped FBG or a discretely chirped FBG array comprising a stack of N standard gratings with dissimilar feedback wavelength $\lambda_{FBG,i}$ (i: 1 ... N). Based on the distributed filter feedback, λ_L is tuned in pulsed operation via the repetition rate f_{PRR} that is adjusted with a modulator. (modified from [143])

and precise spectral control. Dispersion-tuned fiber lasers have been initially realized based on continuously chirped FBGs and electro-optical modulators (EOMs) enabling tunable and mode-locked operation in a sigma-ring cavity. While the first implementation is filed by Li et al. with a tuning range of 6 nm in the Er band [89], it has been extended to about 60 nm in the Yb-band recently [80]. Because the fabrication of continuously chirped FBG with large bandwidths is challenging due to the required long FBG lengths, dispersion tuning has been realized recently with discretely chirped FBG arrays [139]. The filter bandwidth can be readily enlarged based on a large-scale inscription of the FBGs during fiber drawing enabling huge grating numbers (see subsection 2.2.2). Hence, not only large bandwidths are feasible, but the discrete spectral sampling also uniquely facilitates tailored tuning ranges based on independently and individually designed response wavelengths $\lambda_{FBG,i}$. Accordingly, this discrete tuning method not only sets the bandwidth record for tunable fiber-integrated lasers with a tuning range of 74 nm in the Yb band, but also demonstrated excellent emission properties over stacked wavelength ranges with adaptable spectral tuning resolutions [143]. However, dispersion tuning in the sigma-ring cavity is connected to a changing PRR along the tuning range as spectral control parameter creating inherent limitations. Particularly for the long delay paths of discrete FBG arrays, the pulse duty cycle varies significantly promoting inconsistent pulse properties (e.g.: pulse energy and duration, peak power) along the tuning range [139]. Additionally, the direct link between f_{PRR} and the emission wavelength is problematic in various applications that, e.g., rely on clocked processes.

3 Tunable Theta Cavity Fiber Laser (TCFL)

The inherent limitations of dispersion tuning in the sigma-ring resonator as discussed in subsection 2.4.3 can be overcome with a new resonator design. The target is to fuse the promising features of dispersion-tuned lasers with a constant PRR over the spectral operation window. Such a system could access a broader application field and potentially offers more stable pulse properties over the tuning range. Accordingly, a new tuning mechanism with discrete FBG arrays has been developed based on a theta-ring cavity. This name is inspired by the Greek letter Θ resembling the shape of this resonator. Its design facilitates a constant PRR over the tuning range due to two filter interactions per round trip compensating for the distributed feedback of the FBG array. By adapting the ideas of dispersion-tuned systems, spectral tuning is controlled via optical gating of pulses. The concept and experimental investigation of the tunable theta cavity fiber laser (TCFL) is presented in this chapter.

3.1 Concept of the tunable theta-ring resonator

In the following section, the developed tuning concept based on the theta-ring cavity and FBG arrays as tailored spectral filters will be introduced in detail. Alternative resonator layouts as well as important aspects for the experimental implementation are discussed. In subsection 4.2.2, an innovative multi-wavelength emission mode will be presented. As part of this thesis, the developed tuning concept with single- and multi-wavelength emission in the theta-ring resonator was filed for a German patent, which has been granted in 2018 [76].

3.1.1 Wavelength tuning via optical gating

The foundation of the novel tuning concept is a theta-ring resonator. Fig. 3.1 sketches the working principle. The theta layout comprises an outer ring structure with a lower and upper loop. Two 3-port circulators connecting the loops ensure unidirectional operation in the ring structure. Hence, the output coupler (OC) features a single laser output port. Exemplarily, the OC and the gain element are placed in the lower loop. The theta layout also features a middle branch coupled to both sides to the outer ring structure by the two circulators. The middle branch includes a modulator and the reflective spectral filter, which is illustrated by a discrete FBG array with N gratings comprising different feedback wavelengths $\lambda_{FBG,i}$ ($i = 1...N$). Continuously chirped FBGs may be also used. By switching between high loss and high transmission with a specific timing, the modulator induces pulsed operation.

The working principle of the tuning concept is highlighted by graph 1 to graph 3 in Fig. 3.1 tracking the spectral signal formation along one round trip. Starting from the gain medium, the active fiber typically emits broadband amplified spontaneous emission (ASE) as sketched in graph 1. The forward propagating part passes via port 2 of circulator 1 to the FBG array. Each grating overlapping the fluorescence spectrum reflects a specific narrowband fraction. Due to the distributed feedback, those wavelengths $\lambda_{FBG,i}$ addressed by the i^{th} grating are returned at

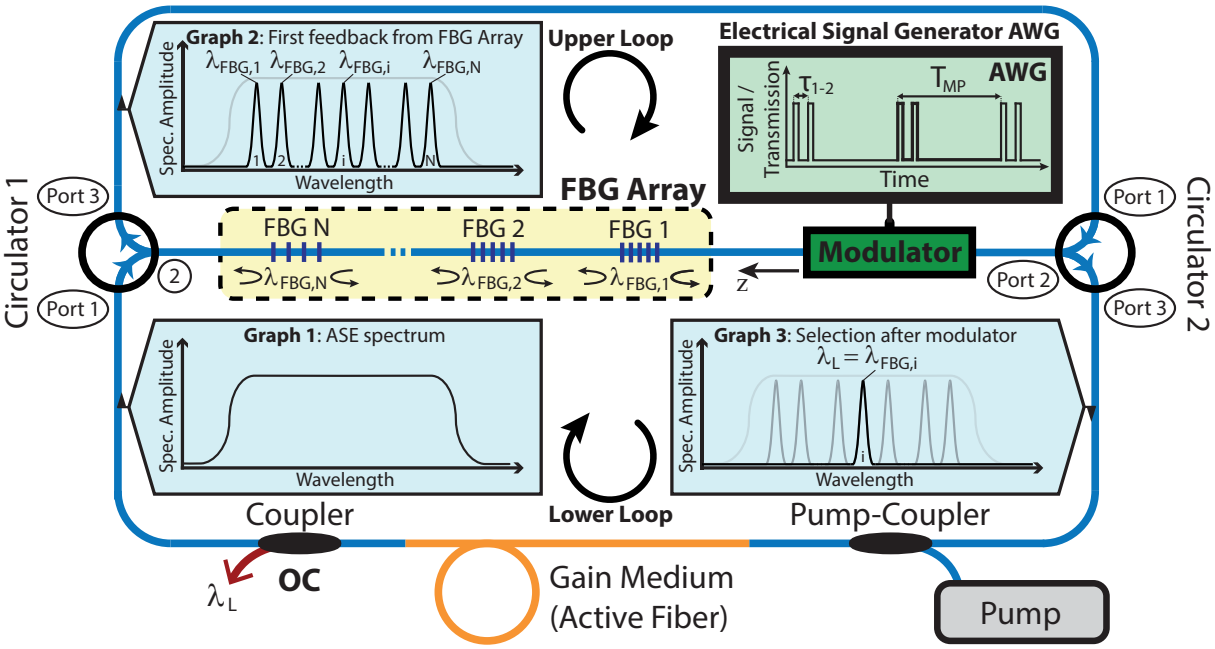

Fig. 3.1: Principle structure of the tunable theta-ring resonator. The outer ring structure exemplarily incorporates the output coupler (OC) as well as the gain medium. The middle branch comprises an FBG array as reflective spectral filter and a modulator to apply optical gating, which is electronically controlled via an electrical signal generator. Two circulators direct the light path coupling the middle branch to the unidirectional upper and lower loop. Graph 1 to graph 3 sketch spectral pulse formation over one round trip. The emission wavelength λ_L is tuned by modifying the electronic delay τ_{1-2}.

dissimilar positions in the FBG array inducing a temporal delay. Spectral regions with weak overlap to a grating pass to the modulator that blocks them due to high IL in the default state. As depicted in graph 2, the feedback spectrum of the FBG array comprising multiple lines propagates via the upper loop to circulator 2 and gets coupled to the middle branch from the right-hand side (port 2). Without considering the modulator, each spectral component $\lambda_{FBG,i}$ interacts again with the corresponding grating reflecting it back to circulator 2 to complete the round trip via port 3 in the lower loop with the gain element.

The two counter-propagating filter interactions in the middle branch compensate for the specific spectral delays acquired due to the distributed feedback. This cycle ensures the same physical path length for each wavelength over one round trip in the resonator. Assuming short FBGs compared to the resonator length L_R, the path comprises one pass through the outer ring structure and two passes through the complete middle branch in total. Neglecting the small impact of chromatic dispersion over typical gain bandwidths of active fibers and supposing steady FBG strengths, each wavelength $\lambda_{FBG,i}$ features an identical PRTT T_{RT} given by equation(2.13) to

$$T_{RT} = \frac{L_R}{c_0} \cdot n_{gr,eff} \ . \tag{3.1}$$

The impact of dispersion is discussed within the experimental study in section 4.1. With the pulse repetition rate f_{PRR} being inversely determined by T_{RT} in steady pulsed emission, the theta-ring cavity layout provides the foundation for a constant PRR over the full tuning range as targeted. Accordingly, compared to the PRR-based dispersion tuning in the sigma-ring resonator, a novel control mechanism is required to effectively narrow down the broadband filter feedback and to tune the laser.

The tuning mechanism in the theta-ring resonator utilizes optical gating. The basis is provided by a modulator that generates pulsed emission by applying short transmission windows. Optical gating aims for presetting a certain timing in the route of the pulses to govern their path in the resonator. This temporal control mechanism promotes a specific operation regime of the laser with a corresponding emission wavelength λ_L by lower propagation losses.

For spectral tuning, this approach exploits the distributed feedback of the chirped FBG filter. Its response time to a pulsed signal with respect to the modulator (located at $z = 0$) is given by

$$T_{filter}(z) = \frac{2z}{c_0} \cdot n_{gr,eff} \ . \tag{3.2}$$

The distributed feedback of the filter induces a spatial dependence of its response wavelength $\lambda_{FBG}(z)$. For the case of a continuously chirped FBG in the area $z > z_0$, this can be described by

$$\lambda_{FBG}(z) = \lambda_{FBG,0} + \gamma \cdot (z - z_0) \ . \tag{3.3}$$

Here, $\gamma = \frac{d\lambda_{FBG}}{dz}$ labels the linear chirp parameter and z_0 the distance of the modulator to the beginning of the filter region, which reflects the wavelength $\lambda_{FBG,0}$. The structure of a discretely chirped FBG array with equidistant spectral and spatial spacing of the gratings can be also approximated by a discretized version of equation(3.3). Eliminating z from equation(3.2) by plugging in equation(3.3) relates the filter response time to its feedback wavelength by

$$T_{filter}(\lambda_{FBG}) = \frac{2n_{gr,eff}}{\gamma c_0}(\lambda_{FBG} - \lambda_{FBG,0}) + \tau_{1-2,min} \ . \tag{3.4}$$

The minimum filter response time $\tau_{1-2,min}$ with respect to the modulator is given by

$$\tau_{1-2,min} = \frac{2z_0 n_{gr,eff}}{c_0} \ . \tag{3.5}$$

The structural dispersion represented by $T_{filter}(\lambda_{FBG})$ gives access to control the effective filter spectrum for pulsed laser oscillations via optical gating. As depicted with the trace in the electrical signal generator of Fig. 3.1, two short transmission windows are applied with a delay τ_{1-2} to each other to determine a specific $T_{filter}(\lambda_{FBG})$. Consequently, an effective feedback wavelength $\lambda_{FBG,i}$, matching the selected response time $T_{filter}(\lambda_{FBG,i}) = \tau_{1-2}$, is promoted by low insertion losses at the modulator transitions. Other wavelengths $\lambda_{FBG,j}$ $(j \neq i)$ are blocked at the second pass through the modulator due to the mismatch $T_{filter}(\lambda_{FBG,j}) \neq \tau_{1-2}$. At those times, the modulator operates at the default high loss state. The resulting spectral clipping is highlighted by the transition between graph 2 and graph 3 of Fig. 3.1 illustrating the impact of optical gating in conjunction with the second filter interaction. This process requires a modulator with proper extinction.

Due to minimized round-trip losses for $\lambda_{FBG,i}$, this wavelength survives one round trip and gets further amplified in the lower loop. In order to build up a strong laser signal by stimulated emission of radiation over several round trips, optical gating with the two transmission windows needs to be applied repeatedly with period $T_{MP} = \frac{T_{RT}}{m}$ matching a fraction of the PRTT with

$m \in \mathbb{N}$ as the modulation order. The PRR of the laser operates at the inverse modulation period T_{MP}.

Summarizing the working principle, optical gating presets the time of flight τ_{1-2} in the distributed filter favoring a specific feedback wavelength $\lambda_{FBG,i}$ by lower effective IL. Thus, laser oscillations are spectrally locked to the corresponding grating determining the emission wavelength $\lambda_L = \lambda_{FBG,i}$. The laser automatically jumps on the operation mode with the highest effective round-trip gain at λ_L considering also the losses. Following this scheme, the emission can be tuned to another wavelength $\lambda_{FBG,j}$ by electrically changing τ_{1-2} to the respective filter response time $T_{filter}(\lambda_{FBG,j})$. Thus, the delay τ_{1-2} operates as spectral tuning parameter in the theta-ring resonator locking λ_L to the specific feedback wavelengths of the FBG array.

3.1.2 Alternative resonator layouts

The functionality of the tunable theta-ring resonator described in subsection 3.1.1 can be realized in various cavity layouts. First of all, individual components may be repositioned in the cavity to adapt the characteristics of the system. This mainly concerns the OC as well as the modulator. The latter is underlying some boundary conditions to still ensure the described functionality. In general, tuning via direct optical gating in the theta layout requires two transmission windows that are applied with an isolated filter interaction of the circulating laser signal in between. This gives access to control the time of flight in the filter structure and thus tune the effective feedback spectrum. While this can be realized with a single modulator in the middle branch as discussed in subsection 3.1.1, the theta-ring resonator would also work with two modulators located, e.g. in the upper and the lower loop, respectively. Accordingly, each modulator would only trigger a single transmission window with an adjustable delay to the other. On the expense of an additional component, this configuration could enhance ASE suppression or further eliminate parasitic pulse paths in the cavity.

Reducing the number of cavity elements, each of the circulators could also be replaced by a 2x2 fused fiber coupler that utilizes the 4^{th} port as OC port to extract the laser signal. However, the OC ratio could only be adjusted on the expense of elevated IL of the middle branch. If the isolation, ensuring unidirectional operation in the ring structure, is not sufficient, a plain isolator could be included as well. Another design variation considers various gain media. They could be arranged in parallel paths coupled by wavelength-division multiplexers (WDMs) to enlarge the gain bandwidth. An additional option is to divide the amplification to two gain elements, placed in the lower and upper loop respectively to be more resilient to elevated IL of the filter.

Following the main idea of the two counter-propagating filter interactions per round trip, an alternative scheme to the theta-ring design is depicted in Fig. 3.2. Instead of two 3-port circulators, this layout utilizes a single 4-port circulator to direct the pulse path reducing complexity. Such a figure-of-eight scheme is widely used for mode-locked fiber lasers to implement, e.g., nonlinear loop mirrors using fused fiber couplers [59].

Starting from the gain media in Fig. 3.2, the pulse propagates to the left-hand side of the FBG array via circulator port 2. Any transmitted fraction is blocked at the AOM (default state at high loss) whereas the reflected pulse passes via port 3 to the right-hand side of the FBG

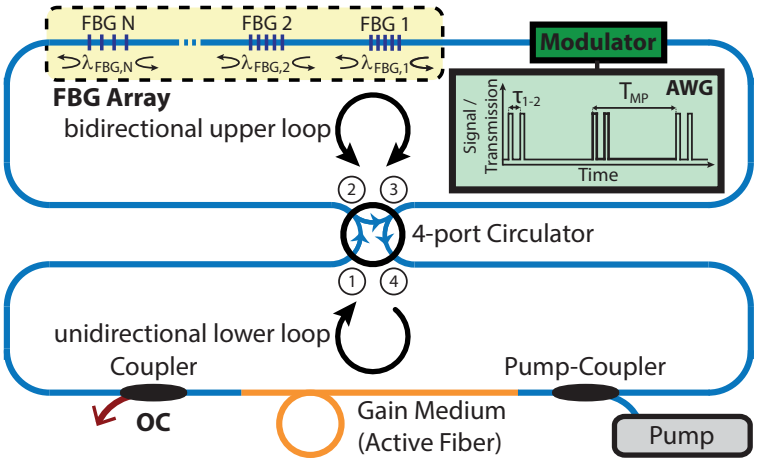

Fig. 3.2: Alternative resonator design following a figure-of-eight laser layout using a 4-port circulator. The emission spectrum is controlled by optical gating applying the same principles as presented for the theta-ring resonator.

array ensuring two counter-propagating filter interactions. In the same way as in the theta-ring resonator, optical gating is applied via two transmission windows with adjustable delay τ_{1-2} for controlling of the effective response spectrum. The modulator placed on port 3 of the circulator promises best gain isolation. Subsequently, the spectrally filtered pulse transfers to the lower loop via port 4 of the circulator completing the round trip. Hence, while the lower loop is passed unidirectional, the upper loop is operated bidirectional.

The working principle is based on the same ideas as the presented theta-ring layout. Even though, 4-port circulators became readily available in the $1\,\mu m$ band (e.g. offered by `Advanced Fiber Resources Ltd.`), they are rather exotic and barely available in many spectral regions. Thus, tuning in the figure-of-eight-like configuration has limited relevance and is not investigated experimentally.

The considerations in this chapter are also valid for tunable multi-wavelength operation as discussed in subsection 4.2.2.

3.2 Experimental setup

The experimental study of the proposed tuning concept is conducted based on Yb-doped fiber lasers. Due to the commercial demand, the corresponding spectral region around $1060\,nm$ offers a good availability of fiber components, such as circulators, couplers or modulators with industry-leading specifications.

The principle experimental setup is sketched in Fig. 3.3 following the scheme discussed in subsection 3.1.1. It is a fiber-integrated setup without free-space signal paths featuring the full integrity of fiber optic networks. The resonator has been implemented both, in a non-PM design, and in a PM design solely with polarization maintaining components. Based on PM circulators operating only in the slow polarization axis, the latter features linearly polarized output as beneficial in diverse applications, e.g. in nonlinear-frequency generation. Except of the FBG array and the active fiber in the non-PM case, the system has been built with commercial fiber components, employing $125\,\mu m$ (d_{clad}) single-mode fibers.

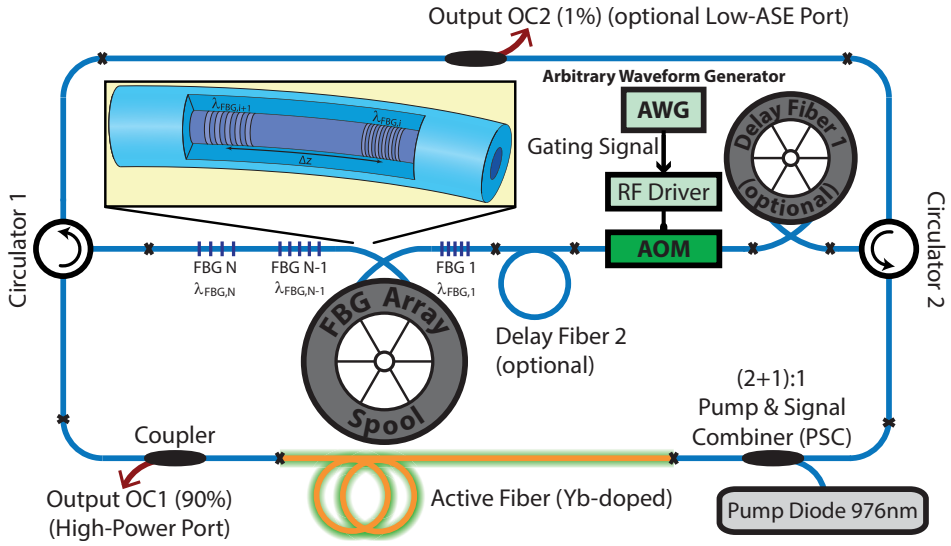

Fig. 3.3: Principle experimental setup of the tunable Yb-doped TCFL. Depending of the desired tuning range, different FBG arrays are used as discrete spectral filters. Optical gating is realized with an acousto-optic modulator (AOM) controlled by a LabVIEW driven arbitrary waveform generator (AWG). The fiber-integrated setup is implemented both in a non-PM layout and a PM layout.

Active fiber: As gain medium, Yb-doped silica fibers are employed emitting around $1.06\,\mu m$. Based on the considerations in 2.3.3, both systems, the non-PM setup and the PM setup, are developed with a cladding-pumping geometry. A more gradual absorption of the pump light along the active fiber generates rather low population inversions ($n_2 \ll 0.5$) beneficial for large tuning bandwidths. Additionally, cladding-pumping is based on multi-mode pump diodes that offer high pump-powers at low cost. A pump diode emitting at around $976\,nm$ is used for pumping the active fiber coupled by a pump-signal combiner. The non-stabilized diode is operated on a thermoelectric cooler to actively control the temperature ensuring good spectral overlap with the narrowband Yb absorption line (see Fig. 2.9). Whereas the non-PM system employs a common in-house developed fiber (`IPHT 1099sAF2`: $d_{core} = 7\,\mu m$, $d_{clad} = 125\,\mu m$, core-$NA \approx 0.12$, Yb concentration $0.18 mol\%$ in aluminosilicate, length $\approx 7\,m$), the PM setup uses a commercial fiber (`LIEKKI Yb1200-6/125DC-PM`, core-$NA = 0.12$, length $\approx 5.5\,m$). The corresponding lengths ensure pump light absorption of around 90%.

Output coupler (OC): The OC is implemented based on fused fiber couplers from `Gooch&Housego` or `Advanced Fiber Resources Ltd.` using `HI 1060` fiber (non-PM setup) or `PM 980` fiber (PM setup). The main OC (OC1) is placed after the active fiber ensuring high output powers and reduced nonlinear distortions for the circulating laser signal. While different coupling ratios have been investigated, best efficiency and stability is achieved with a specified OC ratio of 90%. An optional second OC (OC2) is placed in the upper loop to monitor pulse formation along the round trip by tapping the spectrally pre-filtered signal. Due to the low coupling ratio of 1%, the PM version utilizes a fast-axis aligned coupler.

Circulators: The two circulators are models from `Advanced Fiber Resources Ltd.` build with `HI 1060` fiber (non-PM setup) or `PM 980` fiber (PM setup). They feature low IL (per port $\approx 0.5\,dB$) and high isolation ($> 30\,dB$ at the center wavelength) ensuring unidirectional propagation on the outer ring structure. The PM version works in fast-axis-blocked mode to facilitate linearly polarized output of the TCFL.

FBG array: The FBG array determines the main spectral features of the laser including particularly the spectral operation window of λ_L. During the experimental study, several FBG array designs have been employed depending on the aim of the investigation. Due to their significance to the tuning concept, they have been inscribed in-house with tailored characteristics for the TCFL. This particularly concerns the addressed spectral operation window, feedback linewidths, spatial FBG separation Δz and reflectivity. The implemented filter designs are introduced during the discussion of the corresponding study. A list of all the FBG array designs is provided in Appendix B.

The inscription procedure follows the methodology of reference [13]. Because standard fibers (`1060XP` fiber in the non-PM setup or `PM 980` fiber in the PM setup) are used due to low coupling losses and low-cost, some FBG arrays have been inscribed in hydrogen loaded fibers to enhance photosensitivity and shorten the exposure time during the inscription. With a fixed FBG length of about $1\,cm$, the reflectivity of a grating at $\lambda_{FBG,i}$ is adjusted via the exposure time. In order to ensure consistent FBG properties along the FBG array, PM gratings have been inscribed in rotationally aligned fibers to avoid any disturbances of the inscribing laser beam arising from the PM stress elements.

Modulator: The modulator is implemented by a fiber-coupled acousto-optic modulator (AOM) driven by a RF (radio frequency) driver. Based on an acoustic wave generated in a crystal, a diffraction pattern switches the light beam between the first diffraction order (transmission state) and zeroth order (default state at high-loss). Further details are given in literature [109]. Compared to faster electro-optic modulators (EOM) working with spectrally sensitive interference effects, AOMs feature an excellent extinction (typically >50dB) over ultra-broad bandwidths due to the default state at high loss. Furthermore, they may handle higher optical powers. AOMs typically achieve rise times of several tens of nanoseconds.

The rise time of the modulator is a crucial property for the optical gating approach. It impacts the filter design by determining the required FBG spacing Δz. The switching speed of the AOM needs to be sufficiently quick to slice out a particular grating response while suppressing the feedback of adjacent FBGs. Vice versa, depending on the required extinction criteria, the spatial FBG separation must ensure a minimum delay between adjacent gratings matching at least the order of magnitude of the AOM rise time t_R. The temporal delay is linked to the Δz via v_{gr} (compare equation(2.13)). As a rule of thumb, $1\,m$ of FBG separation roughly corresponds to $10\,ns$ delay in the reflected signal (roughly assuming $n_{gr,eff} = 1.5$).

Due to the importance of the rise time, the effective switching speed of the implemented AOMs is experimentally characterized. The modulation of a CW light signal injected into the AOM is measured with a photodiode (bandwidth $5\,GHz$) connected to an oscilloscope (`Tektronix DPO70604C`, bandwidth $6\,GHz$). An arbitrary waveform generator (AWG) applies an electrical control pulse with an adjustable width as envelope function to the RF driver switching between loss state and transmission state accordingly. Fig. 3.4 shows the temporal transmission behavior depending on the electrical gate width (GW) τ_{GW} for the two AOM models used in this study. Both AOM versions are specified with a minimum IL of about $2.5\,dB$ to $3.5\,dB$. Graph a) depicts the non-PM AOM from `Gooch&Housego` (`G&H`). It features a measured rise and fall time of $t_R \approx 25\,ns$ (10% level to 90% level). Towards shorter GW $\tau_{GW} \leq 2 \cdot t_R$, the absolute transmission

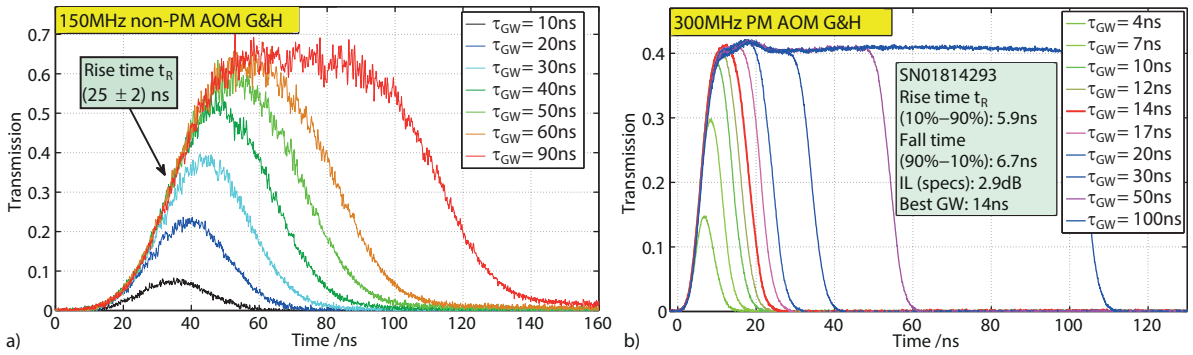

Fig. 3.4: Temporal characteristics of AOMs used as modulators in the theta-ring resonator. Graph a depicts a 150 MHz polarization insensitive version used in the non-PM laser setup and graph b refers to a recently released 300 MHz AOM with optimized rise time used in the PM laser setup. The different traces are recorded for varying gate widths (GW) τ_{GW} of the electrical control signal to find suitable driving parameters.

of the AOM gradually collapses due to the limiting switching speed. Graph b) exemplarily shows a recently released AOM from `G&H` featuring industry-leading rise times below 10 ns. The measurement confirms rise times around $6-7\,ns$ and an optimal gate width of $\tau_{GW} \approx 14\,ns$ combining lowest IL with shortest optical pulse durations. For $\tau_{GW} > 2 \cdot t_R$, the traces feature a typical transmission plateau of the optical pulse since the acoustic wave is fully established in the crystal. AOMs of this model are utilized for the PM laser layout enabling smaller FBG separations due to the feasibility of very short optical gates and thus shorter cavity lengths.

Electrical control of optical gating: In order to realize the proposed optical gating scheme with the modulator, the AOM needs to be operated with a corresponding electrical control signal determining the temporal transmission behavior. As highlighted in Fig. 3.1, the laser is driven by a periodic signal comprising two gating windows with delay τ_{1-2}. Working in the first modulation order $m = 1$ throughout the study, the modulation period T_{MP} has to be matched to the PRTT T_{RT} to enable circulating laser pulses. The tuning parameter τ_{1-2} needs to be freely adjustable to facilitate spectral tuning. Additionally, the periodic gating signal is required to be upgradable by further gating windows with adjustable timing and amplitudes as introduced in section 4.2 for tunable multi-wavelength emission.

To facilitate all those demands, an arbitrary waveform generator (AWG, `Tektronics AFG3252C`) enabling customized electrical signals that can be tailored with highest flexibility to drive the laser. Due to the complexity of the driving signal, especially for triggering multiple emission wavelengths as discussed in subsection 4.2.5, a `LabVIEW`-based control program has been developed that conveniently translates the gating parameters (e.g. T_{MP}, τ_{1-2} or τ_{GW}) to the corresponding electrical trace. Thereby, the emission properties of the system can be remote-controlled with a computer. Programmable operation also enables automated measurements. For extensive studies of the emission characteristics, major measurements have been performed with an advanced control program automatically tuning the desired gating parameters and triggering data acquisition (optical spectrum analyzer (OSA) for spectral measurements, oscilloscope for temporal measurements).

Typical resonator specifications: Even though, the detailed experimental setups vary for the conducted studies, the cavity layout features characteristic dimensions. The resonator typically

extends over a cavity length L_R between $70\,m$ and $200\,m$. This estimation comprises $5\,m$ to $7\,m$ of active fiber, $1\,m$ of pigtail length on each fiber component (in total $18\,m$) and two times the length of the employed FBG array. As further discussed in the experimental section, two sections of optional delay fiber (`1060XP` fiber in the non-PM setup or `PM 980` fiber in the PM setup) may be included along the round trip to manage the pulse path and suppress parasitic operation regimes. With an estimated propagation time of $5\,ns$ per $1\,m$ (assuming $n_{gr,eff} = 1.5$, equation(2.13)), the PRTT $T_{RT} = T_{MP}$ ranges from about $350\,ns$ to $1000\,ns$, corresponding to a PRR of $f_{PRR} \approx 1...3\,MHz$. Depending on the size of the FBG array and the included delay fiber, different PRR can be realized.

The round-trip loss for pulses can be estimated based on the IL of each component. Due to two filter interactions per round-trip, the gratings in the FBG array are designed with high reflectivity (mostly 90% - 99%) ensuring decent round-trip losses. Depending on the specific layout, round-trip losses add up to about $20\,dB$ (detailed: $10\,dB$ at OC1, $(2 \cdot 0.5)\,dB$ at each circulator, $(2 \cdot 3)\,dB$ with two passes through the AOM, and roughly $2\,dB$ for the two filter interactions, splice losses, OC2 as well as general propagation losses).

3.3 Tunable single-wavelength operation

In order to experimentally demonstrate the working scheme of the proposed tuning method in the TCFL, the first part aims to establish spectrally filtered laser emission that can be tuned over the full operation bandwidth of the FBG array. During this study, peripheric operation regimes are discussed that may occur in the TCFL, potentially compromising the emission properties. With their origin connected to inadequate cavity configurations, design considerations are derived for the resonator to restrict the TCFL to the desired operation regime at λ_L. In the second part, the resulting TCFL configuration is investigated extensively regarding characteristic emission properties of this tuning approach. Together with the discussion of the impact of various operation parameters on the output characteristics, the study presents the performance outlining the prospects of the novel concept. Some results of this section have been published in reference [140].

3.3.1 Design considerations of the resonator

The proposed tuning mechanism in the TCFL is based on promoting the desired operation regime with the emission wavelength λ_L. Optical gating is applied to preset the corresponding pulse path. However, the branched design of the theta-ring resonator, comprising the outer ring structure and the middle branch, may open up parasitic sub cavities inducing unintended emission features. Based on the limited isolation of the circulators as well as multiple transmission windows at the AOM, the impact ranges from compromising side peaks to unwanted peripheric operation regimes. The cavity design underlies certain constraints to suppress parasitic side effects forcing the system to operate on the desired emission characteristics at λ_L. In the following, major design aspects and side effects are discussed that have been investigated during establishing tunable operation in the TCFL to unravel the full potential of the tuning approach.

The study includes spectrally overlapping FBGs as well as the importance of cavity dimensions to avoid unambiguous wavelength selection and parasitic pulse regimes.

3.3.1.1 Establishing spectral tuning in the TCFL

Initial experiments are performed based on a basic non-PM TCFL working with FBG array A. This filter comprises 10 gratings with a spatial spacing of $3\,m$ and a spectral separation of about $1\,nm$ ranging from $1069\,nm$ to $1060\,nm$ in declining order. The gratings of the filter have been inscribed targeting maximum reflectivity $R > 99\%$ to minimize round-trip losses (reflectivity spectrum, see Fig. 3.6b). Verifying the proposed tuning mechanism, the aim of this configuration was to establish spectrally filtered lasing that can be switched via τ_{1-2} along the feedback wavelengths of FBG array A. Recorded for T_{MP} matched to the PRTT, Fig. 3.5a shows emission spectra for different τ_{1-2}. In case of $\tau_{1-2} = 50ns$, the emission shows a distinct laser line at $\lambda_L = 1068.7\,nm$ matching the feedback wavelength $\lambda_{FBG,1}$ of FBG 1. Changing τ_{1-2} to $80\,ns$ (green trace), λ_L jumps to the adjacent grating forming a distinct peak at $\lambda_{FBG,2} = 1067.7\,nm$. This spectral evolution confirms basic tunability verifying the proposed tuning mechanism.

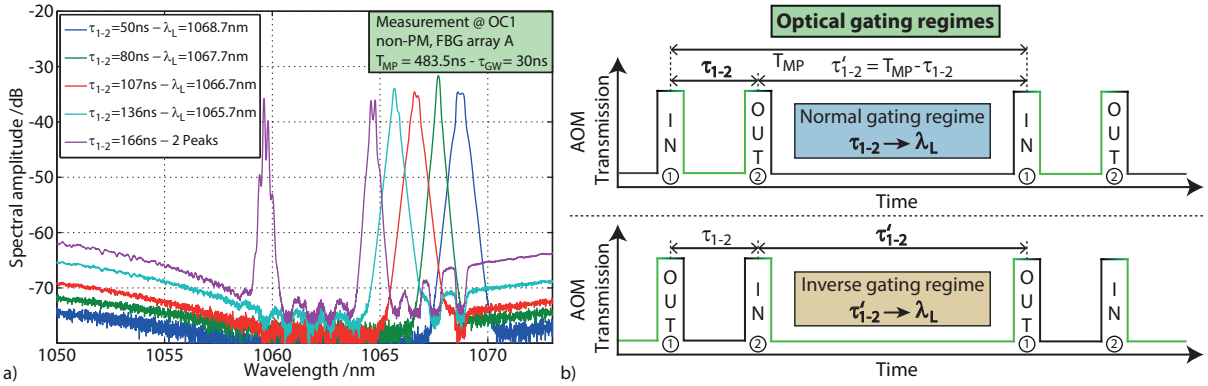

Fig. 3.5: Graph a) pictures the emission spectra of the first generation of the TCFL for varying τ_{1-2} demonstrating basic tunability. Part b) illustrates the ambiguity in the optical gating signal of the TCFL. The green fractions of the traces frame the interaction period of the pulse with the filter. Whereas in the inverse regime, τ'_{1-2} presets the time of flight in the filter, the desired normal regime works with τ_{1-2} to determine λ_L. The transition between normal and inverse gating regime is observed at $\tau_{1-2} = 166\,ns$ in graph a) with two spectral peaks.

3.3.1.2 Criterion for unambiguous spectral tuning

The spectral tuning parameter τ_{1-2} controls the delay between the two optical gating windows determining the time of flight in the filter section. The gating signal is applied with a fixed period at T_{MP} to establish circulating pulses in the cavity. However, due to the periodicity, the order of the gates is ambiguous. This results in two optical gating regimes as illustrated in part b) of Fig. 3.5. The two graphs sketch the optical gating signal of the AOM. Defining the time of flight in the filter, green sections highlight potential periods when laser pulses interact with the FBG array after passing through the AOM. In the desired normal gating regime at the top, the first transmission window ('IN') per period injects the pulse to the FBG array and the second gate ('OUT') picks a specific grating response determining λ_L. With the periodicity of

the optical gating signal, the laser may also favor the equivalent inverse gating regime (lower graph). In this case, the second gate of each period works as injecting gate ('IN') and the first gate of the succeeding period selects the response of the filter ('OUT'). Accordingly, the inverse delay

$$\tau'_{1-2} = T_{MP} - \tau_{1-2} \tag{3.6}$$

determines the time of flight in the filter selecting λ_L. In general, both regimes are equivalent. Gain competition defines the operating regime.

The occurrence of both regimes is pictured in Fig. 3.5a. Following the structure of the FBG array, trace one at $\tau_{1-2} = 50ns$ to trace four at $\tau_{1-2} = 136ns$ show a steady decline of λ_L in steps of about $1\,nm$. The system is governed by the desired normal gating regime. Going to trace five at $\tau_{1-2} = 166ns$, two spectral emission lines are observed at $1064.7\,nm$ and $1059.7\,nm$. Increasing τ_{1-2} a bit more, the emission line at $1059.7\,nm$ wins the gain competition (not in picture). In principle, with τ_{1-2} gradually increasing in the normal gating regime, the emission wavelength of the laser would be expected to scan from FBG 1 to FBG 10 in discrete steps of $1\,nm$. While the emission at $1064.7\,nm$ is linked to FBG 5 triggered by the normal gating regime, the occurrence of lasing at $1059.7\,nm$ filtered by FBG 10 marks the transition to the inverse gating regime. This can be verified by the applied gating parameters. The transition of the regimes has been observed at $\tau_{1-2} = 166ns$ where the emission of FBG 5 is expected. With $T_{MP} = 483.5\,ns$ matching the PRTT in the resonator, $\tau'_{1-2} = T_{MP} - \tau_{1-2} = 317.5ns$. On the other side, with an FBG spacing of $3\,m$ corresponding to a delay of about $30\,ns$ between adjacent gratings, FBG 10 is actually expected to occur at a time of flight in the filter section of $50\,ns + 9 \cdot 30\,ns = 320\,ns$. This estimation matches the value of τ'_{1-2} of trace five. Accordingly, while driving the laser with $\tau_{1-2} = 166ns$ corresponding to $1064.7\,nm$, the inverse gating regime at $\tau'_{1-2} = 317.5\,ns$ overlaps to the filter response time of FBG 10 at $1059.7\,nm$. Due to the stronger net gain at this wavelength (see Fig. 2.10a or ASE background in Fig. 3.5a), the inverse regime stars to win the gain competition for further increasing τ_{1-2}.

The example in Fig. 3.5a demonstrates the challenge with the two potential gating regimes. The spectral emission might jump unpredictably to another grating preventing to cover the full tuning range. Because the process is driven by gain competition, it is sensitively dependent on environmental influences and other operation parameters of the laser including particularly the pump power which originally is not associated to spectral tuning. Additionally, the laser pulse occurs delayed by τ'_{1-2} in the inverse regime. Accordingly, for direct spectral tuning via τ_{1-2}, the laser is desired to operate solely in the normal gating regime to fully unravel the potential spectral tuning bandwidth.

The inverse gating regime is avoided with a modified resonator configuration. The setup needs to prevent the inverse delay τ'_{1-2} to address another grating response time within the demanded working regime of τ_{1-2}. No overlap in the gating regimes is guaranteed as long as the scan range of τ_{1-2} is only linked to τ'_{1-2} which are still larger than $\tau_{1-2,max}$. This parameter $\tau_{1-2,max} = \tau_{1-2,N}$ represents the response time of the N^{th} grating determining the longest time of flight in

the filter section. Based on the definition in equation(3.6), this is ensured as long as the overall resonator length satisfies the condition

$$T_{MP} > 2 \cdot \tau_{1-2,max} \tag{3.7}$$

Considering the finite optical gating window widths $\tau_{GW,opt}$ in the experiment, a more reliable condition for no overlap in the gating regimes would be $T_{MP} > 2 \cdot \tau_{1-2,N} + \tau_{GW,opt}$. In a plain picture, the resonator length must be significantly larger than twice the length of the FBG array. This can be achieved by placing a delay fiber anywhere in the resonator except of between the AOM and the FBG array. As indicated in Fig. 3.3, an efficient implementation would be by delay fiber 1, where the physical length effectively doubles due to a double pass arrangement in the middle branch. Succeeding experiments are based on an extended resonator to address the full tuning range in the normal gating regime.

In principle, an alternative criterion can be established for the case of very short FBG arrays compared to the residual resonator. Inversing the previous condition, τ'_{1-2} always needs to be smaller than the minimum filter response time $\tau_{1-2,min} = \tau_{1-2,1}$ of FBG 1. This results in the setup condition $\tau_{1-2,min} > T_{MP}/2$ ensuring that within the working range of τ_{1-2}, τ'_{1-2} does not match the time of flight of another filter wavelength. This case is only considered in theory, since practical cavity dimensions in the experiment match with the initial considerations.

3.3.1.3 Spectral overlap of FBGs

The non-PM resonator has been modified to comply with the criteria of equation(3.7). An additional piece of passive delay fiber is incorporated adding 115 m of resonator length. With a matched $T_{MP} = 1041.18\,ns$ to the new PRTT, Fig. 3.6a shows the corresponding emission spectra of the TCFL, scanning τ_{1-2} along the response spectrum of FBG array A. Up to $\tau_{1-2,max} = \tau_{1-2,10} \approx 312\,ns$, the system is governed by the normal gating regime. A tuning range of 9 nm has been achieved as defined by the FBG array. Covering all 10 feedback lines of the filter design, the full functionality of the tuning concept is verified.

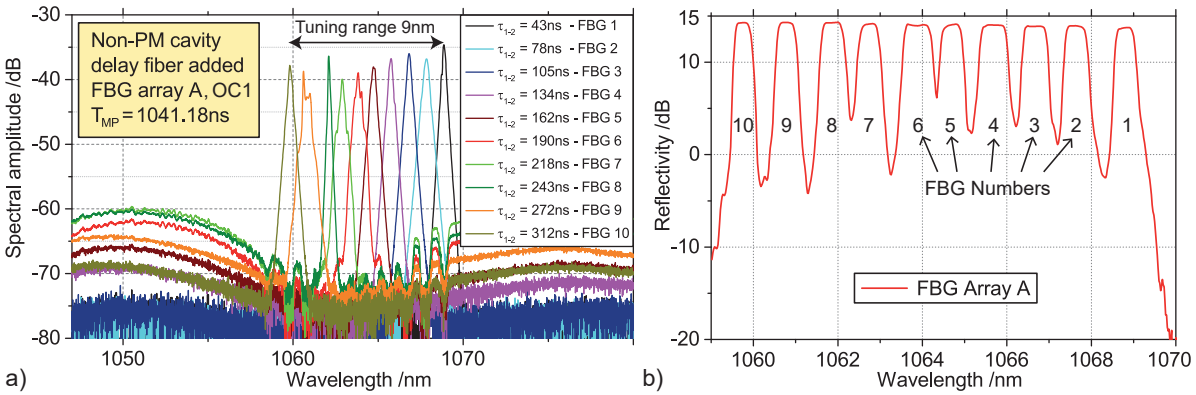

Fig. 3.6: Graph a) shows the emission spectra of the non-PM resonator with added delay fiber. A tuning range of 9 nm has been achieved by scanning τ_{1-2} over all the gratings. Graph b) shows the reflectivity spectrum of FBG array A referenced to the feedback of a plain fiber cleave (0 dB level at $R \approx 4\%$).

The emission characteristics feature diverse line shapes, varying amplitudes and an elevated ASE background for a few wavelengths. They are explained by the characteristics of FBG array A. Fig. 3.6b shows the measured reflectivity spectrum referenced to a plain fiber cleave ($0\,dB$ level at $R \approx 4\%$, $14\,dB$ to $15\,dB$ correspond to $R \approx 100\,\%$). The spectrum comprises 10 feedback peaks corresponding to the 10 gratings as labeled. Because this FBG design solely targets maximized reflectivity reducing IL, the feedback lines are saturated forming a peak plateau with a broad line shape. The FWHM (full width at half maximum) exceeds $500\,pm$. In contrast to the FBG feedback lines, the emission lines of the laser in Fig. 3.6a exhibit a rather sharp peak with linewidths of about $250 - 300\,pm$ (FWHM). Gain competition pushes small features within the broad feedback plateaus of the FBGs to narrow down the laser emission. However, with the laser locked to a specific grating, small fluctuations may cause spectral variations within the broad feedback line of the FBG. Combined with the averaged acquisition of an OSA, the spiky emission lines of e.g. grating 9 are explained by this effect.

The degrading spectral amplitudes and elevated ASE background for central emission lines in Fig. 3.6a are also connected to the spectral width of the filter elements. In conjunction with the small spectral FBG spacing of $1\,nm$, adjacent gratings feature a spectral overlap in the response spectrum. As highlighted in Fig. 3.6b, dips between adjacent feedback lines do not drop to the noise floor of the measurement. Especially between grating 2 and 3 and 4, 5 and 6 or 7 and 8, the dips stay above the $0\,dB$ level (equivalent to $R > 4\%$) indicating significant spectral overlap. The detailed overlap including potentially spectral side lobes could only be quantified by measuring each grating solely.

In the TCFL, spectral overlap between gratings induces elevated effective insertion losses of the filter structure. Parts of the laser pulse are reflected by a neighboring FBG exhibiting a different time of flight in the filter section. With those fractions being detuned to the optical gating signal, they are blocked at the AOM. Additionally, spectrally overlapping FBGs may form small Fabry-Pérot sub-resonators further degrading the filter feedback. Elevated insertion losses reduce the efficiency of the laser. This is mostly represented by degrading spectral amplitudes as well as clearly enhanced ASE background around e.g. $1050\,nm$ when the system is operated at FBGs in the center. For FBG 7, the spectral amplitude dropped by more than $5\,dB$ compared to FBG 1 with only $20\,dB$ of signal contrast to the ASE background (at FBG 1: $40\,dB$).

Due to two counter-propagating filter interactions and the distributed feedback from the FBG array, the TCFL is prone to spectrally overlapping filter segments degrading its efficiency. To overcome the limitations of FBG array A that has been inscribed within the strong-grating regime (see subsection 2.2.1), a new filter has been designed targeting spectrally isolated FBG responses. Together with larger spectral gaps between adjacent gratings, this is achieved by narrower feedback linewidths. It is mainly controlled by the strength of the imprinted index modulation $\overline{\Delta n_{eff}}$ (correlates with the exposure time) because the overall grating length is technologically limited to about $1\,cm$ [13, 14]. Accordingly, the tradeoff between strong reflectivity (see equation(2.21)) and narrow linewidths (see equation(2.22)) is adjusted via the exposure time of the FBG. Following these considerations, succeeding FBG arrays are exposed right to the point where the feedback strength starts to saturate targeting a high-reflective regime in proximity to the weak-grating limit.

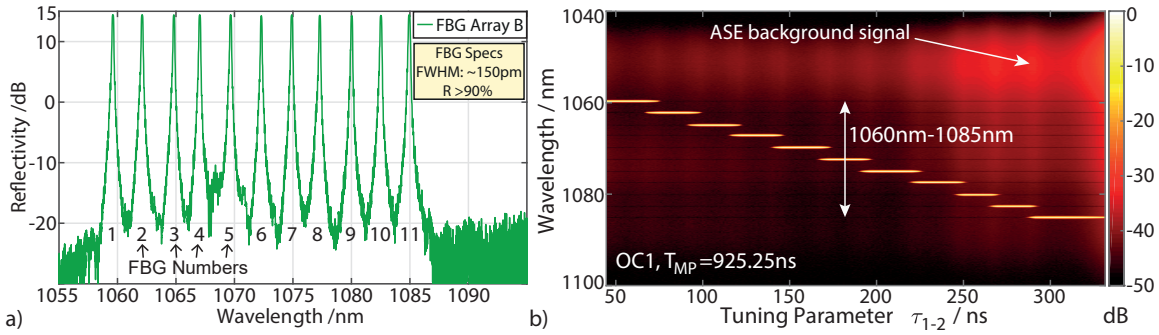

Fig. 3.7: Graph a) depicts the reflectivity spectrum of FBG array B referenced to a plain fiber cleave. It features a broader operation bandwidth and narrower linewidths of each grating. The tuning spectrogram in graph b) illustrates the spectral emission behavior of the laser over the full tuning range. Due to a gradual scan of τ_{1-2}, the intensity plot representation also resolves the dynamics in the tuning behavior, i.e. transitions between different λ_L.

The feedback spectrum of FBG array B is depicted in Fig. 3.7a. It comprises 11 gratings featuring a broader tuning range of 25 nm within the Yb band with a step size of 2.5 nm. By measuring the IL in transmissive direction, the reflectivity is estimated to $R \approx 95 - 98\,\%$. With minor impact on the feedback strength, the width $\Delta\lambda_{FBG}$ reduced significantly compared to FBG array A measuring about 150 pm. More importantly, the grating responses showing sharp lines are spectrally well decoupled with dips down to the noise floor. The experimental linewidth exceeds the theoretical limit given by the weak-grating approximation (see equation(2.24), $n_{eff} = 1.45$, reduced effective length $L_{FBG} \approx 8\,mm$ due to apodization effects) by a factor of 3 indicating the proximity to the desired regime.

Incorporating FBG array B into the non-PM TCFL, the spectral emission characteristics are illustrated in Fig. 3.7b. The tuning spectrogram shows the evolution of the emission spectrum along a gradual scan of τ_{1-2} in steps of 1 ns revealing the full spectral tuning properties including the transition zones. Bright regions in the intensity plot highlight large spectral amplitudes. Accordingly, the emission wavelength is discretely tuned from one grating to the other covering an extended bandwidth of 25 nm. Simply by changing the FBG array applying two standard splices, the spectral operation window of the laser is fully changed demonstrating the benefits of FBG array tuned lasers. With the new filter design, the full tuning range is covered with steady line shapes, narrow linewidths of about 150 pm (FWHM) following the FBG feedback spectra and high signal contrast of about 40 dB throughout the operation window. As a small feature, the ASE floor shows darker horizontal lines at the spectral locations of the other FBGs indicating dips in the background signal due to the filter effect in the middle branch.

Due to finite optical gate widths $\tau_{GW,opt}$, each emission wavelength has an extended operation window in τ_{1-2} corresponding roughly to the spatial separation between adjacent FBGs. The short transition zones exhibit two neighboring emission wavelengths at a time (occurring delayed by the spatial FBG spacing). Looking towards applications and further studies, τ_{1-2} will be altered in adapted steps sizes to directly tune along the single-wavelength emission with maximum signal contrast skipping the transition zones. Still, with no parasitic emission lines throughout the scanned range of τ_{1-2}, the TCFL is reliably coupled to the feedback of the FBG array. Hence, laser oscillations are tightly locked to the filter feedback confirming proper operation of the tuning mechanism.

Further emission characteristics of the TCFL are discussed in subsection 3.3.2. In summary, FBG array B significantly improved the emission properties supporting the presented design targets for filters in tunable TCFLs. Still, avoiding spectrally overlapping FBGs to ensure high filter efficiencies in the TCFL puts constraints on the achievable spectral resolution of the discrete tuning concept. The spectral gap between FBGs dictating the spectral sampling needs to exceed the feedback linewidth of the gratings. Sharp FBG responses are required for high tuning resolutions.

3.3.1.4 Parasitic pulse echos at output coupler OC1

Another parasitic effect is depicted by pulse echos that might occur at the OC ports, e.g. OC1. The corresponding pulse path in the resonator is sketched in Fig. 3.8. A pulse echo at OC1 can arise from the first filter interaction of each round trip. As highlighted in part a) of Fig. 3.8, the incoming pulse from circulator 1 with a wavelength $\lambda_L = \lambda_{FBG,j}$ is reflected at FBG j to pass to the upper loop. Due to the finite peak reflectivity $R < 100\,\%$ and narrow linewidth of the grating, a small fraction of the pulse with an effectively broader line shape is transmitted towards the AOM. Commonly, the modulator is in the default loss state to block this pulse duplicate. However, in case the travel time of the reflected pulse in the upper loop to the modulator ($\tau_{Filter,j} + \tau_{up}$) matches the propagation time $\tau_{Trans,j}$ of the parasitic filter transmission from grating j to the modulator, both signals arrive coincidentally when the first optical gating window switches to high transmission. Synonymously, the round-trip time in the lower loop (including the middle branch) matches τ'_{1-2}. The weak pulse echo couples via circulator 2 to the lower loop where it is amplified in the gain medium. Accordingly, a considerable pulse echo is expected at OC1 arriving with a delay τ'_{1-2} to the original pulse.

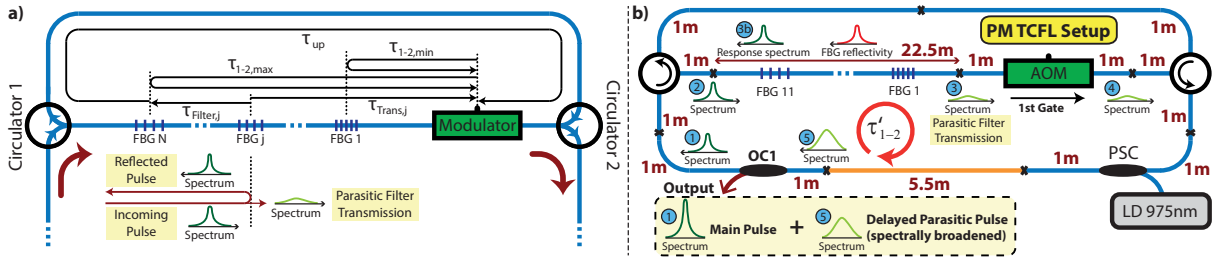

Fig. 3.8: The cavity schemes illustrate the pulse paths causing a parasitic pulse echo at output coupler OC1. Part a) sketches the pulse interaction at FBG j ($\lambda_L = \lambda_{FBG,j}$), where the reflected signal is accompanied by a parasitic filter transmission due to the finite FBG reflectivity. Scheme b) shows the setup of the implemented PM TCFL (without any additional delay fiber) and FBG array C highlighting the cavity dimensions (red numbers). Following the order of the blue circles, the formation of the parasitic pulse echo (5) is illustrated starting from the original pulse at OC1 (1). At the output, both signals add up delayed by τ'_{1-2}.

This effect has been reproduced experimentally while investigating the initial PM TCFL setup as sketched in Fig. 3.8b. As spectral filter, FBG array C has been used that is introduced in detail in subsection 3.3.2 (see Fig. 3.13). Notably, the gratings exhibit a peak reflectivity of $90 - 95\,\%$ leaving a parasitic transmission of about $5 - 10\,\%$. The formation of the parasitic pulse echo at OC1 is spectrally highlighted via small graphs along the pulse path sorted by blue numbered circles. The original pulse at OC1 (1) passes to the FBG array (2) where it gets

reflected (3b). A considerable fraction (exhibiting a broadened linewidth) transmits (3), passes through the AOM via optical gate 1 (4) and gets amplified in the lower loop (5) to couple out at OC1 delayed by τ'_{1-2} to the original pulse.

As depicted in Fig. 3.9, the experimental emission characteristics of the PM TCFL with FBG array C have been recorded via the tuning spectrogram (graph a), logarithmic scale) and temporal tuning trace (graph b), linear scale). In both intensity plots, τ_{1-2} is scanned incrementally ($1\,ns$ steps) over a wide range covering the normal gating regime as well as the inverse gating regime. The occurrence of the latter prevents to exploit the full potential tuning range of FBG array C ($50\,nm$) as discussed previously. Since both regimes are equivalent, the spectral tuning trace in graph a) mirrors over the scan. In the time domain, the pulse trace in the inverse gating regime shows a temporal shift over the tuning range because the measurement is triggered with respect to the normal gating regime (linked to optical gate 2) maintaining steady pulse positions.

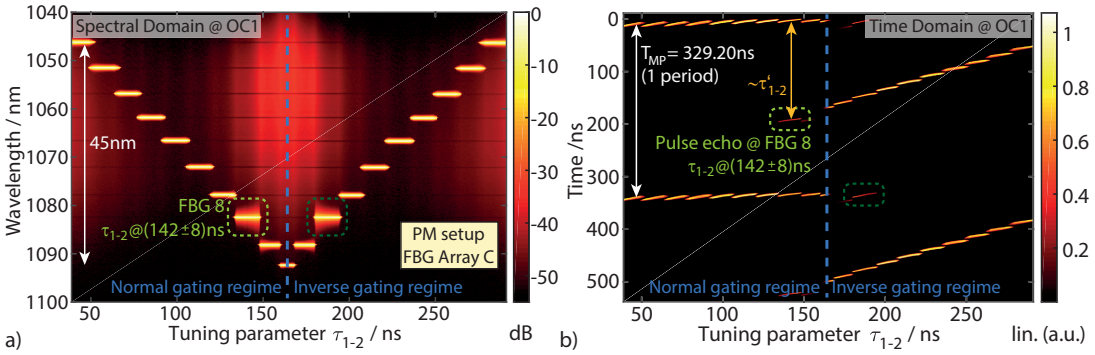

Fig. 3.9: Graph a) and b) show the spectral and temporal emission properties, respectively, for the PM TCFL with FBG array C. For $\tau_{1-2} < 165\,ns$, the system works in the normal gating regime. At FBG 8, a parasitic pulse echo occurs in the time domain delayed to the main pulse. In the spectral domain, this results in a spectrally broadened line shape.

The parasitic pulse echo becomes apparent in the green dashed boxes occurring at FBG 8. In the range of $\tau_{1-2} = (142 \pm 8)\,ns$, the spectral line shows significant broadening on the edges compared to the other emission lines. In a subsequent experiment, $3.5\,m$ of delay fiber was included in the middle branch temporarily, shifting this broadening effect to FBG 9 and 10. Accordingly, the broadening cannot be traced back to specific FBG properties. Looking in the temporal domain of graph b), the emission at FBG 8 features a parasitic pulse echo in between the main pulses of two succeeding periods i.e. pulse round trips. The echo is marked by a green dashed box occurring with a delay of about $188\,ns$ after the main pulse. This parasitic effect reproduces in the same way in the inverse gating regime as marked with the dark green dashed boxes in Fig. 3.9.

Comparing the observed timing of the parasitic echo to the resonator dimensions given in Fig. 3.8b (red numbers), the lower loop of the resonator accumulates to a length of about $38.5m$ matching a propagation time of about $192.5\,ns$. In the experiment, the parasitic pulse occurred in the region around $\tau_{1-2} = (142 \pm 8)\,ns$ resulting in $\tau'_{1-2} = (187.2 \pm 8.0)\,ns$. This value matches the predicted pulse round-trip time in the lower loop indicating experimentally that the broadening results from an amplified echo of the original pulse at OC1.

With an amplitude of about 40 % compared to the main pulse, this parasitic effect becomes considerable in the time domain potentially degrading the output properties. Besides a maximized FBG reflectivity, the pulse echo can be suppressed by a suitable laser design. The underlying condition for the occurrence of that pulse echo is given by

$$\tau_{Filter,j} + \tau_{up} = \tau_{Trans,j} \ . \tag{3.8}$$

In order to provide no operation regime of the laser satisfying this condition, resonator dimensions may be adapted. The criteria results from the pulse paths in the resonator. Considering the case of the longest transition time through the filter ($\tau_{Trans,N} = \frac{1}{2}\tau_{1-2,max}$ =maximum, $\tau_{Filter,N} = 0$), an upper limit to avoid the parasitic regime is given by $\tau_{up} > \frac{1}{2}\tau_{1-2,max}$. For the inverse case ($\tau_{Trans,N}$ = minimum = $\frac{1}{2}\tau_{1-2,1}, \tau_{Filter,N}$ = maximum = $\frac{1}{2}(\tau_{1-2,max} - \tau_{1-2,min})$), the other limit is given by $\tau_{up} < \left(\tau_{1-2,min} - \frac{1}{2}\tau_{1-2,max}\right)$. This case is considerable when the difference results in a positive value ($\frac{1}{2}\tau_{1-2,max} < \tau_{1-2,min}$), i.e. comparably short FBG arrays. In conclusion, the parasitic pulse echo may only occur within the limits of

$$\tau_{1-2,min} - \frac{1}{2}\tau_{1-2,max} \leq \tau_{up} \leq \frac{1}{2}\tau_{1-2,max} \ . \tag{3.9}$$

Resonator dimensions must be chosen accordingly for τ_{up} and the FBG array length to suppress this parasitic regime at OC1 ensuring unspoiled emission properties.

On the contrary, if the criteria in equation(3.9) is not considered and the parasitic pulse echo occurs by chance at $\tau_{1-2} = \tau'_{1-2} = \frac{1}{2}T_{MP}$, the effect becomes resonant over multiple round trips with a subcavity in the lower loop potentially destroying spectrally filtered emission.

3.3.1.5 Parasitic pulse echos at output coupler OC2

Another parasitic echo may be observed at OC2. Similar to the pulse echo at OC1, it arises from a parasitic filter transmission at the FBG array during the second filter interaction. The corresponding signal propagates with low losses via circulator 1 to OC2 where it appears as a weak pulse echo of the main signal delayed by the round-trip time in the upper loop (including the middle branch path). Starting from output coupler OC2, the path of the parasitic signal in the upper loop is highlighted by a red arrow in Fig. 3.10a. The sketched setup depicts the non-PM resonator with FBG array B. Labeled along the red arrow, the corresponding IL experienced by the parasitic signal along circulator 2, the AOM (switched to transmission state, optical gate 1), the filter (in transmission direction) and circulator 1 add up to about 20.5 dB to 25.5 dB. This corresponds to the expected minimum attenuation compared to the main pulse at OC2.

The experimental observation of this effect is depicted in Fig. 3.10b showing the temporal emission behavior in logarithmic scale over the tuning range measured at OC2. The graph pictures about 1.5 periods of the laser emission with two horizontal yellowish traces showing the main pulses and two red traces as the corresponding echo. Matching to the origin of the echo, its temporal delay to the main pulse is steady, measuring around 438 ns. However, the amplitude of the echo is about 30 dB to 35 dB below the main pulses. The difference to the

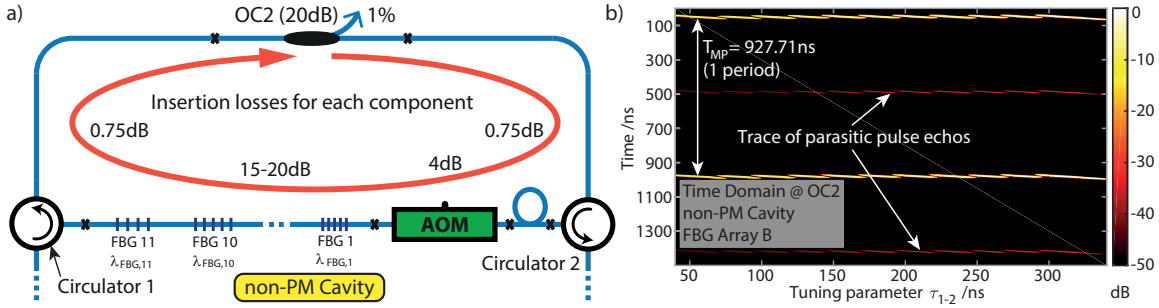

Fig. 3.10: Part a) sketches the upper loop of the TCFL in the non-PM configuration indicating the pulse path of a parasitic echo effect at output coupler OC2. The graph in part b) pictures the experimental observation of the parasitic pulses (reddish traces) at OC2 measured in the time domain along the complete tuning range.

expected attenuation might be explained by higher experimental IL at the modulator due to short GW (compared to the AOM rise time) as well as additional loss sources like splices and the propagation through the FBG array and delay fiber.

The weak amplitude of this effect including the negligible impact on the spectrum sets low priority to incorporate additional precautions to suppress it. Even though, the parasitic pulse, occurring throughout the tuning range, does not rely on any resonance effect with the timing of the optical gates, it is not experiencing any further amplification. Thus, in contrast to the echo at OC1, it is much weaker without any degradation in laser efficiency. Still, if it is desired to be further suppressed, higher reflectivity of the gratings as well as a different OC2 position (e.g. between circulator 2 and PSC, see Fig. 3.3) are options. Another alternative is offered by shifting the AOM in between circulator 1 and the FBG array inducing a resonance condition like discussed for OC1 with the current AOM position. With an AOM at both positions in the middle branch, the echos could be suppressed completely inducing more complexity and losses.

3.3.2 Emission properties and tuning characteristics

In the following, characteristic emission properties of the TCFL will be discussed. As labeled for each measurement, the studies have been conducted with different cavity setups, i.e. the non-PM design and the PM design. Hence, the operation parameters may not always be equivalent.

3.3.2.1 General tuning characteristics

An overview over the characteristic operation behavior of the TCFL is provided in Fig. 3.11. For a specific tuning step, i.e. $\tau_{1-2} = 112\,ns$ locking the laser to FBG 3 ($\lambda_L = 1064.8\,nm$), the measured electrical gating signal (a), the corresponding emission spectrum (b), the pulsed signal in the time domain as an overview (c) as well as a zoomed in version on the pulse (d) are shown. Additionally, the emission spectrum (e) and corresponding pulse shape (f) are highlighted for another tuning step at $\tau_{1-2} = 170.5\,ns$ representing the transition zone between two emission wavelengths. For a complete overview covering both cases, a video is included in the multimedia appendix illustrating the behavior over the full tuning range (file name: *Single-Wavelength-Tuning.mp4*). By incrementally scanning τ_{1-2}, the correlation between electrical gating signal and the emission spectrum is highlighted.

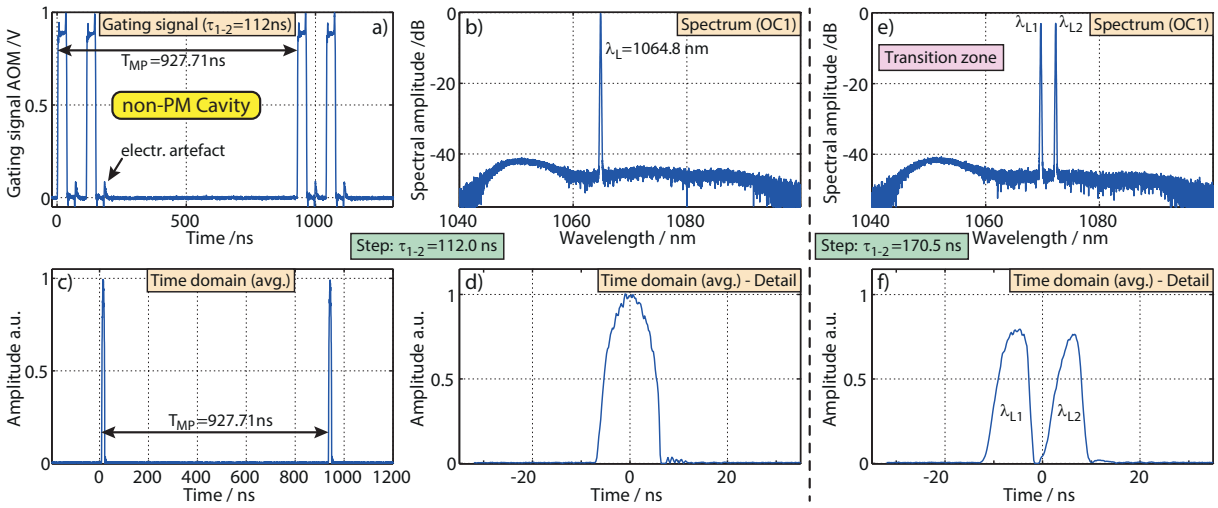

Fig. 3.11: Graph a) shows an exemplary measurement of the electrical gating signal applied to the non-PM TCFL with FBG array B at $\tau_{1-2} = 112\,ns$. The corresponding emission properties are pictured in b) (spectrum), c) (time domain, overview) and d) (time domain, detailed). While this measurement was recorded with TCFL locked to a single emission wavelength, graphs e) and f) feature the spectral and temporal emission trace at $\tau_{1-2} = 170.5\,ns$, which corresponds to the transition regime between two wavelengths. The emission behavior over the complete tuning range is illustrated in a video that is attached in the multimedia appendix (name: *Single-Wavelength-Tuning.mp4*).

Graph a) in Fig. 3.11 pictures the electrical gating signal over more than one period, driving the AOM. It shows the two gating windows for $\tau_{1-2} = 112\,ns$ with a gate width adjusted to $\tau_{GW} = 35\,ns$. The corresponding emission spectrum of the laser in b) shows a sharp emission line at $\lambda_L = 1064.8\,nm$ matching the feedback wavelength of grating 3. The broad ASE background peaking at around $1050\,nm$ is superbly suppressed giving a signal contrast of more than $40\,dB$. The ASE peak position matches well with the modeled gain characteristic in subsection 2.3.3 with a target population inversion n_2 of around 9% for extended tuning bandwidths. Combining the low ASE background with the narrow laser linewidth, which even at the $-40\,dB$ level stays below $600\,pm$, the tunable system features excellent spectral emission properties. In conclusion, adding up to the tuning characteristics in Fig. 3.7b, the presented filtering mechanism works very reliable and efficient with the laser being tightly locked to the spectral feedback of the target FBG. Without any parasitic lasing peaks and high signal contrast, the well confined spectral emission properties are maintained throughout the tuning range.

The overall temporal emission behavior is illustrated in Fig. 3.11c. The laser works with pulsed emission at the PRR matching the adjusted T_{MP}. Neither any side pulses nor an elevated background are visible. The detailed pulse shape is depicted in graph d). It features a parabola-like shape with steep edges to both sides. The pulse duration τ_{pulse} (FWHM) in this case is about $8\,ns$ to $9\,ns$ matching the magnitude of the AOM rise time. As discussed in subsection 4.1.2, the symmetric pulse shape depends on a finely tune T_{MP} and is not fully maintained over the tuning range. Small offsets in T_{MP} cause minor asymmetric distortions in the pulse shape (also shown in the video *Single-Wavelength-Tuning.mp4*).

To analyze the emission also in the transition zone between two laser wavelengths λ_{L1} and λ_{L2}, graph e) and f) show the emission spectrum and pulse shape at $\tau_{1-2} = 170.5\,ns$. As the spectrum (e) confirms, the laser emission is simultaneously locked to FBG 5 ($1069.5\,nm$) and

FBG 6 (1072.0 nm). The spectral power is equally distributed between both wavelengths with the amplitudes dropping to about 50% (3 dB) compared to the single emission line. In this transition zone, the system still operates with well suppressed ASE background and without any parasitic lines. The occurrence of this transition zone is connected to the spatial FBG spacing in the filter design being adjusted to the optical gate widths at the AOM.

In the time domain (f), the simultaneous oscillation of two emission wavelengths in the transition zone causes two pulses temporally separated by about 12 ns. This delay arises from the distributed FBG array feedback. Its magnitude is linked to the spatial FBG separation convolved by the effective optical gate width at the AOM. Even though, the transition zone enables two emission wavelengths at a time, this operation regime does not depict an adjustable dual-wavelength emission. Being locked to the neighboring emission line, both wavelengths cannot be tuned independently. Additionally, the two emission wavelengths occur with fixed timing temporally separated to each other. A novel dual-wavelength regime with simultaneous and independently tunable operation will be introduced in section 4.2.

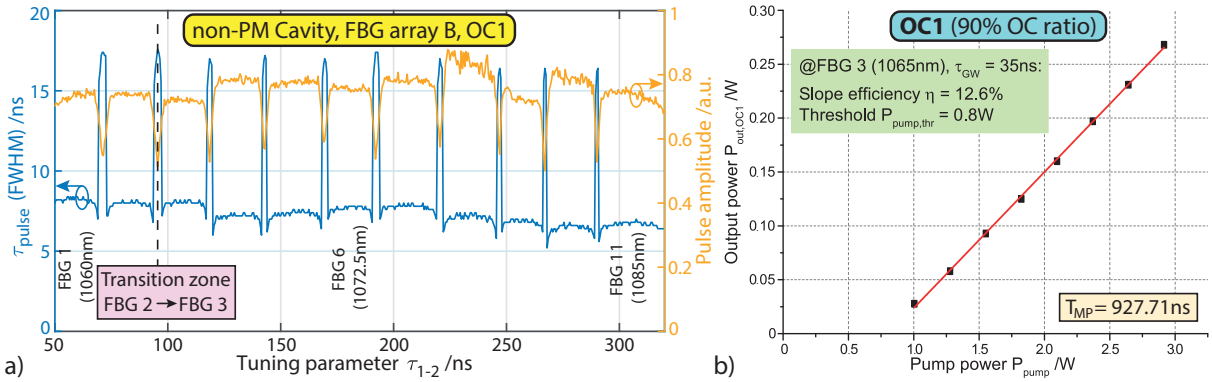

Fig. 3.12: Plot a) highlights specific temporal emission characteristics comprising the pulse duration (left-hand side scale) and pulse amplitude (right-hand side scale) over an incremental scan of τ_{1-2}. Graph b) shows the power characteristics at OC1 recorded exemplarily at λ_L locked to FBG 3 at 1065 nm.

Analyzing the pulse duration (blue) and its amplitude (orange) more closely, Fig. 3.12a plots their behavior over the full tuning range of FBG array B recorded with constant T_{MP}. Both traces show 11 plateau zones separated by peaks (τ_{pulse}) or dips (pulse amplitude), which arise as measurement artifacts in the transition zones between two emission lines. These characteristic effects are typical in measurements incrementally scanning τ_{1-2}. The 11 plateau zones depict the emission locked to the corresponding grating showing broad and stable operation zones in τ_{1-2} for each wavelength. Over the tuning range, the pulse duration varies slightly in the region around 7 ns to 8 ns. Remarkably, the pulse duration is clearly shorter than the rise time of the modulator (25 ns), i.e. the width of the optical gates. Characteristically for the TCFL, optical gating with two temporal filter interactions per round trip lowers the pulse duration compared to the tunable sigma-ring laser with a pulse duration of about 30 ns to 40 ns when operating with similar modulator characteristics [143]. For the pulse amplitude, the variations over the tuning range vary within a 7% window. FBG 8 shows an elevated and noisy temporal amplitude.

The variations in the time domain arise from varying working points of the laser set, e.g., by the FBG reflectivity, effective spectral gain and dispersion-based drifts in the OC coupling ratio of fused couplers as well as in the PRTT (see subsection 4.1.2). Pulse amplitude fluctuations

are additionally promoted by each fluctuation of τ_{pulse} due to rather steady pulse energies and powers over the tuning range. Nevertheless, due to the theta cavity design, both parameters are substantially more stable as for the tunable sigma-ring laser [139]. Due to the changing duty cycle over the tuning range in the sigma layout, variations of more than 20 % had been observed for the pulse parameters covering even a shorter tuning range of only 18 nm [139]. Thus, the TCFL layout enables much more stable emission properties.

For a comprehensive discussion of the system properties, Fig. 3.12b depicts the corresponding power characteristics. Still, the aim of this study is not connected to any efficiency optimizations or power scaling advances since fiber-based master oscillator power amplifier (MOPA) schemes are well established to boost the output power of a seed source with a specific functionality [74, 110], such as tunability [144]. For the measurement, the emission of the TCFL is exemplarily locked to grating 3 at around 1065 nm. Other emission wavelengths showed similar characteristics. The output power reaches up to 270 mW. The limit is set by the inset of significant spectral broadening due to the long resonator length ($L_R \approx 190\,m$). Most experiments are conducted in the optimum working window at an output power of about $50 - 100\,mW$. Considerable round-trip losses of the system ($\approx 20 - 23dB$) lead to a rather limited slope efficiency of about 12.6% with a pump threshold of about 0.8 W. If required, an optimized resonator would enable enhanced power characteristics. Completing the analysis, with the inverse PRR of $T_{MP} = 927.71\,ns$ and an output power of $P_{out,OC1} \approx 100\,mW$, the pulse energy results to $E_{pulse} = P_{out,OC1} \cdot T_{MP} = 93\,nJ$. For the measured pulse duration of $\tau_{pulse} = 8\,ns$ at FBG 3, the pulse peak power is estimated to $P_{peak} \approx E_{pulse}/\tau_{pulse} = 11.6\,W$.

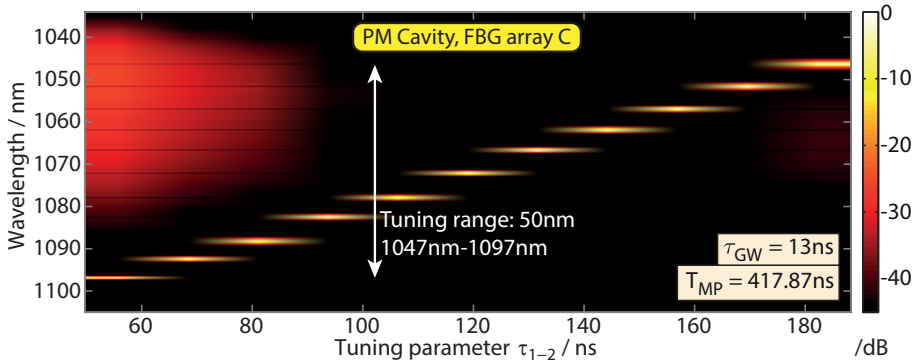

Fig. 3.13: The tuning spectrogram shows the maximum tuning range achieved with the TCFL. The tuning parameter is scanned in 10 discrete steps matching the FBG separation. A maximum tuning bandwidth of 50 nm is realized limited by FBG array C [142].

The maximum tuning range of the presented tuning concept has been achieved with the PM TCFL and FBG array C. This filter comprises 11 gratings covering a bandwidth of 50 nm from 1047 nm to 1097 nm based on a spectral spacing of 5 nm. The spatial separation between adjacent gratings is 1.3 m adapting to the faster rise time of the PM AOM (see Fig. 3.4b). The reflectivity of the FBGs reaches 90%-95%.

Fig. 3.13 shows the corresponding tuning spectrogram. It confirms a discrete tuning range of 50 nm corresponding to FBG array C. In the longer wavelength range of λ_L (i.e. $\tau_{1-2} < 90\,ns$), the ASE background peaking at around 1050 nm increases due to the mismatch between gain maximum and λ_L. Fitting to the considerations in subsection 2.3.3, the emission line at $\lambda_L =$

1097 nm just exceeds the laser threshold showing a 3 dB drop in the spectral amplitude. For the center tuning range, the emission properties show the characteristic high signal contrast surpassing 45 dB.

While the tuning range of 50 nm is solely limited by the bandwidth of FBG array C, the ASE background signal rising at the edges of the scan range indicates some potential to further extend the tuning bandwidth by about 10 nm-15 nm on the shorter wavelength side ($< 1047\,nm$). This matches the model in subsection 2.3.3 predicting a potential tuning range of about 65 nm.

3.3.2.2 Emission characteristics at output couplers OC1 and OC2

Depending on the OC position along the resonator loop, the TCFL offers freedom to extract adapted output signals featuring different characteristics. Based on the different locations of OC1 and OC2 in the cavity, this is highlighted in Fig. 3.14 with 4 plots showing the emission spectrum and pulse shape at OC1 (a and b) and OC2 (c and d) for an arbitrary tuning step at $\tau_{1-2} = 133\,ns$. Similar as for Fig. 3.11, a video visualizes the behavior over the full discrete tuning range of the non-PM TCFL with FBG array B (see multimedia appendix, file name: *Single-Wavelength-TuningOC1&OC2.avi*).

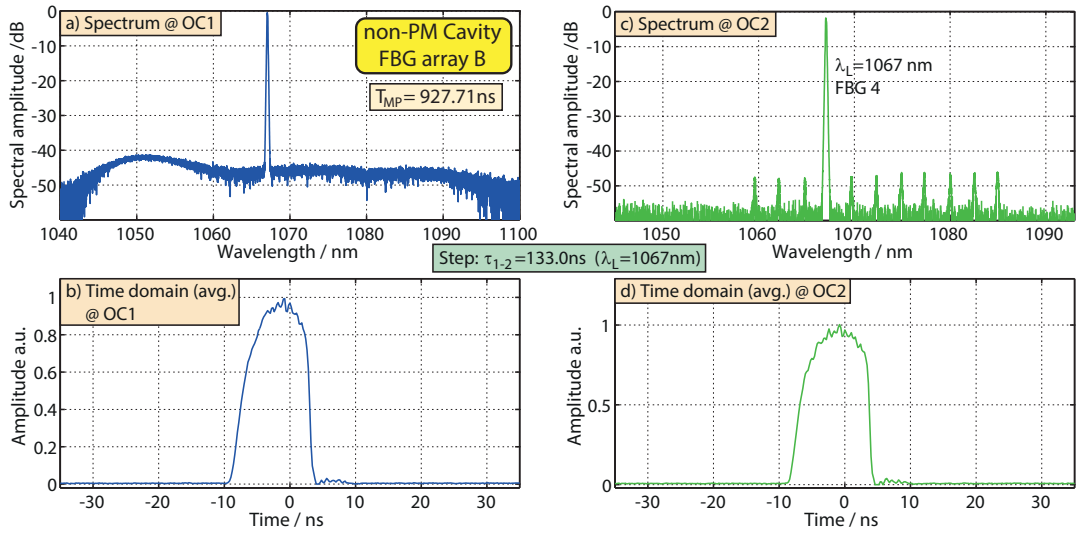

Fig. 3.14: The graphs exemplarily compare the emission characteristics at $\tau_{1-2} = 133\,ns$ of OC1 and OC2 recorded with the non-PM resonator and FBG array B. Plot a) and c) represent the spectral domain and plot b) and d) show the averaged pulse in the time domain. The emission behavior over the complete tuning range is covered in a video that is attached in the multimedia appendix (file name: *Single-Wavelength-TuningOC1&OC2.avi*).

Comparing the temporal emission at OC1 (c) and OC2 (d) in Fig. 3.14, the pulse shapes basically resemble each other showing a pulse duration of about 9 ns and a steeper edge on the right-hand side. This indicates minor pulse variations with steady characteristics along the round trip. In the spectral domain, OC1 (a) and OC2 (b) show the same sharp emission line at $\lambda_L = 1067\,nm$ with the system locked to FBG 4. However, OC2 features a much high ASE suppression. The broad background peak at 1050 nm at OC1 is completely absent at OC2. Only the weak ASE responses from the other gratings become apparent in the background signal at OC2 reaching an overall ASE suppression above 45 dB. This behavior is conform with the

modeled pulse formation in Fig. 3.1. Because propagation of a signal in the upper resonator branch is exclusive for spectral components that are reflected by the discrete spectral filter, this part of the cavity is immune to any broadband ASE background generated by the active fiber. In contrast, OC1 located behind the active fiber experiences neither spectral, nor temporal ASE filtering resulting in a weak but broad background signal. In case the residual ASE responses from the neighboring FBGs are desired to be fully suppressed at OC2, an AOM might be added between circulator 1 and the FBG array applying the optical gating function during the first filter interaction. With combined spectral and temporal filtering beforehand, OC2 would deliver a signal free of an ASE background for unrivaled contrast.

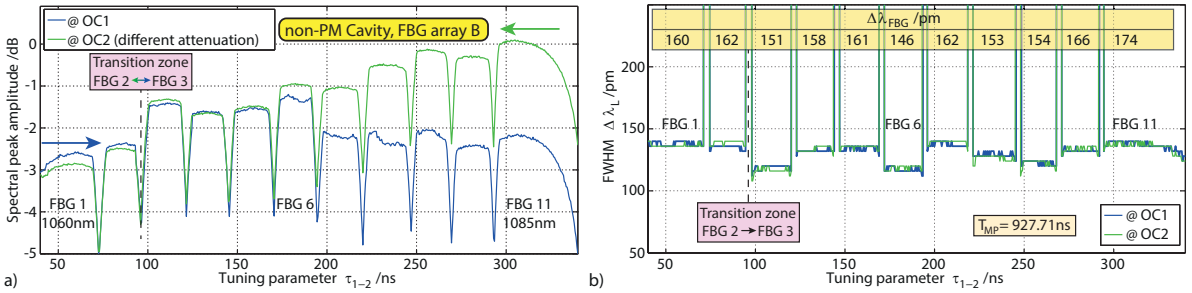

Fig. 3.15: The plots highlight spectral emission properties of the non-PM TCFL along an incremental scan of τ_{1-2} and compare them between OC1 and OC2. Graph a) features the spectral peak amplitude. The colored arrows indicate the read-out order of the gratings with respect to the corresponding OC port. Graph b) shows the laser linewidth $\Delta\lambda_L$ (FWHM) with the corresponding feedback linewidth of each FBG given in the yellow table. The transition zones along τ_{1-2} between different gratings contain measurement artifacts (dips in graph a) and peaks in graph b)).

With resembling pulse properties in the temporal domain at OC1 and OC2, the spectral characteristics are further analyzed over the tuning range as depicted in Fig. 3.15. Graph a) highlights the evolution of the spectral amplitude over both OC ports whereas plot b) analyzes the spectral linewidth $\Delta\lambda_L$. Comparing the spectral amplitudes at the plateaus of the gratings along τ_{1-2}, OC1 shows moderate spectral amplitude variations within a window of $\pm 0.75\,dB$. Those fluctuations are mostly driven by the spectral gain distribution as well as dispersion in the OC coupling ratio, but also show some correlation with the measured linewidth of the emission lines in graph b. The latter is clearly visible at e.g. FBG 3 with a rather narrow linewidth ($< 130\,pm$) and peaking spectral amplitude. At OC2, the spectral amplitudes are additionally superimposed by a steady decay of about $3\,dB$ between $1085\,nm$ and $1060\,nm$. This additional distortion arises from the dispersion in the OC ratio as well as the IL of a single filter interaction including the FBG reflectivity and effective propagation losses. The slope of this loss along the tuning range correlates with the propagation length of the corresponding wavelength λ_L within the filter section. Arrows with matching colors indicate the read-out order of the filter with respect to the corresponding OC port. Accordingly, the strongest spectral amplitude at OC2 (green trace) is reached with FBG 11, which is the closest grating to circulator 1 and thus to OC2. However, standard propagation losses in the commercial filter fiber (`Thorlabs 1060XP`, specified loss $< 2.1\,dB/km$ at a wavelength of $980\,nm$ [4]) over $50\,m$ are expected to be about $0.1dB$ and thus, are much weaker than the observed loss effect. Accordingly, the main loss may arise from spectrally insensitive scattering effects of the signal when passing through the other gratings in the filter structure. This loss may be caused by transversal grating inhomogeneities. Due to the

spectral orientation of the FBG array, each grating can promote e.g. cladding mode coupling on the shorter wavelength side [135]. In contrary at OC1, the spectral amplitude variations are partly balanced due to the second filter interaction as well as operating the amplification of the active fiber in saturation.

Evaluating the spectral linewidths $\Delta\lambda_L$ in graph b) of Fig. 3.15, they vary between $120\,pm$ and $140\,pm$ along the tuning range (specified resolution of OSA: $20\,pm$). This small variation correlates mostly with the raw feedback linewidth $\Delta\lambda_{FBG}$ of the FBGs which is given in the yellow table at the top (e.g. see FBG 3 and FBG 6). In general, the laser linewidth is about 20% reduced compared to the filter response due to the double spectral filtering in each round trip. Supporting the statement of minor pulse evolution effects and steady pulse parameters along the round trip, the linewidth shows negligible differences between OC1 and OC2 port. The traces in Fig. 3.15b mostly resemble each other.

With the two OC ports, the laser features some flexibility to either extract a powerful signal at OC1 with a decent efficiency, or with advanced spectral purity at OC2. Thus, OC1 is referred to as 'High-Power Port' and OC2 as 'Low-ASE Port' (see Fig. 3.3). Due to the difference in the coupler tapping ratios, OC2 measures an output power $P_{out,OC2}$ of about $\approx 0.08\%$ compared to OC1 using the non-PM resonator configuration in Fig. 3.3. As previously discussed, the output power could be further boosted in a MOPA configuration.

3.3.2.3 Spectral sweep speed

A characteristic property of tunable lasers is the sweep speed considering how fast the wavelength can be switched. While most common tuning concepts are rather slow due to inert processes controlling the emission spectrum such as mechanically moving elements (e.g. rotating diffraction gratings, see Fig. 2.11, strain tuned FBGs, see subsection 2.4.3) or temperature effects (temperature tuned FBGs, see subsection 2.4.3), electrically tuned systems benefit from the speed evolution of electronics in the 20th century. Tunable lasers with quick sweep speeds are required in fields like optical coherence tomography (OCT) [159] and sensing [84]. Additionally, enhanced wavelength switching speeds are beneficial for differential absorption Lidar (DIAL) [83, 154]. Sweep speeds of multiple kHz are required.

To evaluate the performance of the tunable TCFL, the wavelength switching speed is analyzed for the PM cavity with FBG array C. An automated routine is developed in LabVIEW to trigger a temporal measurement in the moment of switching. A second channel of the AWG is activated synchronously to the modification of the optical gating signal at channel one, triggering the new emission wavelength. An overview of the switching behavior is given in Fig. 3.16a showing a screen shoot of the oscilloscope measurement. The magenta trace features the optical gating signal and the yellow trace the measured laser output. Due to the large time frame ($40\,ms$) and the time scale of the gating features ($\approx 10\,ns$), the traces only resolve the envelop function of both signals. The TCFL is exemplarily switched from $\tau_{1-2} = 144.2\,ns$ ($\lambda_L = 1062\,nm$, FBG 8) to $\tau_{1-2} = 106.4\,ns$ ($\lambda_L = 1078\,nm$, FBG 5).

The measurement reveals an electrical black out zone of the AWG. In the moment, when the new arbitrary trace containing the information of the updated gating signal is read in, the AWG

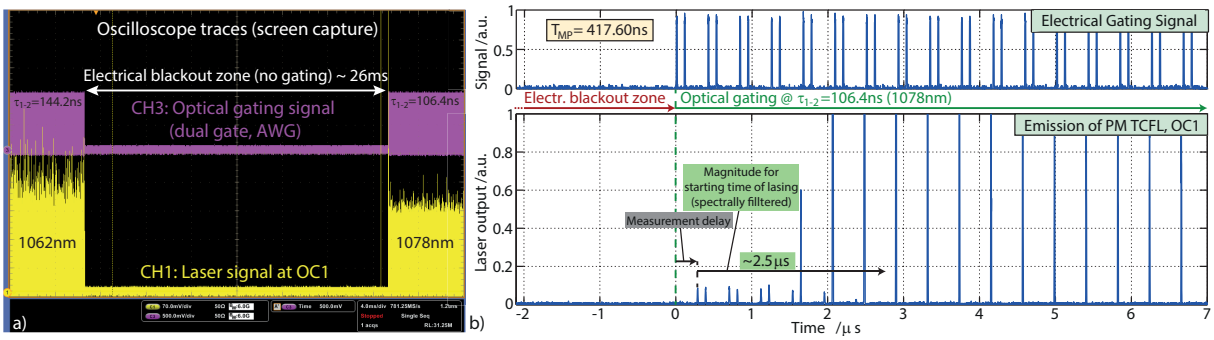

Fig. 3.16: The temporal measurement in a) pictures the experimental switching behavior of the PM TCFL based on the electrical gating signal (magenta trace, oscilloscope channel CH3) and laser output signal (yellow trace, oscilloscope channel CH1). The laser is switched from $\lambda_L = 1062\,nm$ to $\lambda_L = 1078\,nm$ via adjusting τ_{1-2} at the AWG featuring an electrical blackout zone. In b), a detailed plot highlights the switch-on behavior at $1078\,nm$ with the signal of CH3 at the top (gating signal) and CH1 at the bottom (laser output).

terminates any operation for about $26\,ms$. This time frame corresponds to about 62.000 round trips in the cavity. In this period, the AOM maintains the default loss state blocking any lasing at OC1 as expressed in the yellow trace. After the gating signal starts to operate, the laser works on the new emission wavelength ($\lambda_L = 1078\,nm$). The electrical disruption of the driving gating signal prohibits any proper measurement of the physical switching speed between two emission wavelengths of the TCFL. The reason of this behavior is connected to the versatility of the AWG that is not optimized for quick alterations to the arbitrary waveform. With an adapted electrical driving generator, this artificial black out zone could be avoided.

Nevertheless, the potential switching speed of the TCFL can be estimated by analyzing the starting behavior of the system at the new wavelength. This is shown in detail in Fig. 3.16b plotting the inset of the optical gating signal adjusted to $\tau_{1-2} = 106.4\,ns$ in the top graph and the corresponding output signal of the laser in the bottom graph. The time scale is referenced to the activation of the gating signal. The two first optical gates appear with an artificial measurement delay (propagation time of optical and electrical signals) as two weak amplified ASE pulses in the bottom graph. While this pair of ASE pulses resembles over the first three cavity round trips, from round trip 4 on ($> 1.5\ \mu s$), the second ASE pulse quickly wins the competition growing to a strong laser signal while the first pulse vanishes. This transition marks the laser getting locked to the desired pulse path and emission wavelength at $1078\,nm$. After about $2.5\ \mu s$ or 6 round trips in the cavity, the signal fully established operating solely over gate 2 (target gate for tunable operation). Avoiding the inverse gating scheme or other parasitic pulse paths, no signal is measured anymore in the time slot of gate 1.

This measurement highlights the pulse formation in the TCFL to start from the ASE background that, after some round trips of spectral filtering and succeeding amplification, quickly evolves to a powerful laser signal at the desired emission wavelength. The spectrally filtered laser pulse is established after less than 10 resonator round trips resulting in a quick start up time of $< 5\,\mu s$.

The complete switching speed between two random wavelengths potentially happens in the same time scale if the electrical blackout zone is avoided with an optimized gating signal generator. In this case, the alteration in the optical gating signal to a new τ_{1-2} would eliminate the former emission wavelength after one round trip at the AOM (mismatch with the new target time of

flight in the filter section) and the pulse at the new wavelength starts up similarly as measured in Fig. 3.16b. Thus, wavelength switching speeds approaching $100\,kHz$ could be feasible with adapted electronics. Shorter resonators could even go beyond.

3.3.2.4 RF power spectrum analysis

Pulsed sources are commonly analyzed by an RF power spectrum measurement. The precise repetition rate as well as the quality of the pulse train is evaluated potentially revealing parasitic signal components. Such measurements are conducted with electrical spectrum analyzers (ESA). Alternatively, the measurement at the TCFL has been conducted with an oscilloscope working with sufficient memory depth to record long pulse trains (up to $40\,ms$). The RF power spectrum is obtained via post-processing data by a Fourier transform. The resulting frequency distribution represents the temporal emission spectrum of the measured laser intensity trace. The record length defines the frequency resolution. Selected RF emission spectra are plotted in Fig. 3.17 measured with the non-PM TCFL and FBG array B. OC1 and OC2 show identical features.

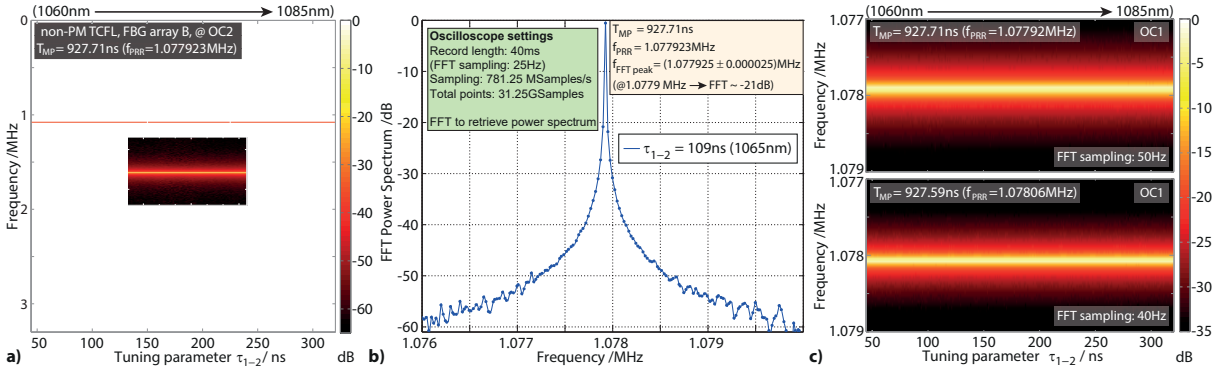

Fig. 3.17: The graphs feature the RF frequency analysis of the TCFL performed via an extended temporal measurement ($\geq 20\,ms$) with an oscilloscope and postprocessing data by a fast Fourier transform (FFT) analysis. Plot a) shows the FFT power spectrum along the complete spectral tuning range of the TCFL with an inset zooming in on the fundamental frequency peak. The other sharp frequency lines represent higher orders. Graph b) pictures a zoomed in power spectrum on the fundamental frequency peak recorded at $\tau_{1-2} = 109\,ns$ comparing the peak frequency with the adjusted $T_{MP} = f_{PRR}^{-1}$. Part c) shows two intensity plots demonstrating how the peak RF frequency shifts with respect to T_{MP} maintaining unperturbed characteristics over the spectral tuning range.

The intensity graph a) illustrates the RF power spectrum up to $3.3\,MHz$ along the full tuning range of the laser. The graph shows 3 very narrow horizontal lines. They correspond to the fundamental operation frequency at around $1.08\,MHz$ and two higher orders at multiples of f_{PRR}. A zoomed inset highlights the fundamental emission line. For a single tuning step ($\tau_{1-2} = 109ns$), graph b) focuses on the fundamental emission frequency of the laser. With enlarged record length ($40ms$), the frequency sampling resolution reaches $25\,Hz$. The spectrum peaks at $f_{FFTpeak} = (1.077925 \pm 0.000025)\,MHz$. This accurately matches the applied modulation period T_{MP} driving the laser with a theoretical frequency of $f_{PRR} = 1.077923\,MHz$. The superbly narrow width of the fundamental frequency is highlighted by a drop in the frequency amplitude of more than $20\,dB$ within the sampling resolution of $25\,Hz$ to both sides of the peak.

Concluding on graph a) and b), the pulsed emission of the TCFL works with excellent purity due to the absence of any non-harmonic frequency components over the full dynamic range ($\approx 60\,dB$)

of the measurement. The peak frequency perfectly follows the driving modulation frequency. Furthermore, the RF spectrum shows no dependence on the emission wavelength maintaining the same shape over the full tuning range and ensuring a steady pulse train. This confirms the novel theta cavity layout to fully ensure the targeted constant PRR over the complete tuning range of the dispersion-tuned laser.

Graph c) investigates the impact of slightly tuning T_{MP} on the RF power spectrum of the TCFL. While the initial value of $T_{MP} = 927.71\,ns$ correlates with a symmetric parabola-like pulse shape when operating the laser at FBG 3 ($1065\,nm$), T_{MP} is detuned for the lower graph to $T_{MP} = 927.59\,ns$ shifting the characteristic pulse shape to FBG 11 ($1085\,nm$). The link between pulse shape and T_{MP} is discussed in subsection 4.1.2. The two RF spectra zooming in on the fundamental frequency line over the full spectral tuning range are recorded for the TCFL operated at the two values of T_{MP}, respectively. Matching superbly the corresponding driving frequencies, the variation in T_{MP} directly translates to a slightly different RF peak frequency shifting by about $140\,Hz$. In both cases, the frequency line shows no dependency on λ_L over the tuning range.

Even though the theta cavity layout ensures matching physical resonator lengths for all emission wavelengths, some spectral sensitivity on the RF spectrum could have been expected due to chromatic dispersion in the propagation properties of pulses in the fiber. Different emission wavelengths propagate with mismatching pulse speeds $v_{gr,eff}$ and thus exhibit slightly detuned PRRT T_{RT}. However, the measurement indicates this effect to be cleaned of by the AOM enforcing a constant PRR over the tuning range perfectly following the periodic driving signal. This also explains why the TCFL works with a different PRR when T_{MP} is changed even though the resonator length is identical. Due to steady temporal filtering by the optical gates in each round trip, pulses in the laser adapt to small mismatches between T_{MP} and T_{RT} emitting with the frequency of the external master clock. This flexibility to electrically modify the PRR is connected to the finite optical gate durations which will be investigated in subsection 3.3.3.

3.3.3 Impact of gating parameters on the laser emission properties

Whereas the TCFL is spectrally tuned via τ_{1-2}, the impact of other gating parameters, i.e. T_{MP} and τ_{GW}, on the emission properties of the laser is investigated in the following.

3.3.3.1 Modulation period

The prerequirement to run the TCFL in tunable pulsed emission is to drive optical gating with a modulation period T_{MP} adjusted to the actual PRTT T_{RT}, corresponding to the resonator length. In the following, the working range of T_{MP} is analyzed regarding its sensitivity towards small mismatches. Fig. 3.18 discusses fundamental laser emission properties which are analyzed over a small scan range of T_{MP}. The experimental study is conducted with FBG array B and the non-PM TCFL that is exemplarily locked to FBG 3. The x-axes label the deviation ΔT_{MP} of the applied modulation period T_{MP} to the default parameter $T_{MP,0}$. The latter is defined by maximum spectral signal contrast assuming the best match with the actual T_{RT} at

this wavelength. Likewise, $T_{MP,0}$ also ensures symmetric parabola-like pulse shapes as shown in Fig. 3.11. The correlation between T_{MP} and the pulse shape will be further discussed in subsection 4.1.2.

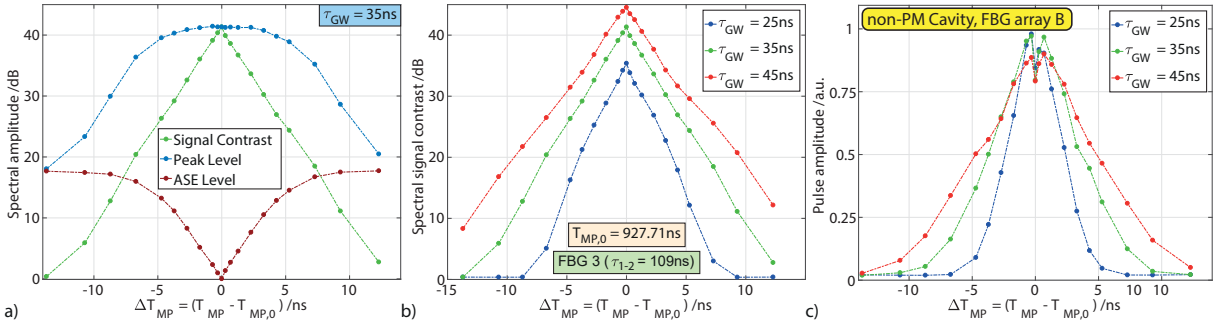

Fig. 3.18: The graphs illustrate the sensitivity of specific emission properties regarding variations in T_{MP}. Whereas the default modulation period $T_{MP,0}$ for an exemplary configuration of the non-PM TCFL with FBG array B operated at FBG 3 ($1065\,nm$) is given by $T_{MP,0} = 927.71\,ns$ (defined by best signal quality and symmetric pulse shape), the behavior of specific emission properties is illustrated regarding deviations $\Delta T_{MP} = T_{MP} - T_{MP,0}$ in the driving modulation period T_{MP}. Graph a) depicts the spectral peak amplitude (blue trace) and ASE background level (red trace) as well as their difference resulting in the effective spectral signal contrast (green trace). Part b) plots the sensitivity of the latter for different gate widths τ_{GW}. In graph c), the normalized temporal pulse amplitude is highlighted.

Graph a) in Fig. 3.18 highlights the spectral signal contrast (green trace) resulting from the difference between the peak amplitude (blue trace) and the maximum ASE background level (red trace) at around $1050\,nm$. As defined before, the signal contrast peaks at $\Delta T_{MP} = 0\,ns$ coinciding with the highest suppression of the ASE background as well as the center of the broad peak amplitude maximum. With this setting, the TCFL works with a matched modulation period to the PRTT ensuring highest efficiency of the optical gating in each round trip. Thus, with minimized round-trip losses, the stored energy in the active fiber is extracted most effectively by the circulating laser signal resulting in best ASE suppression. The overall signal contrast in this setting is about $41\,dB$.

For detuning in T_{MP}, i.e. $|\Delta T_{MP}| > 0\,ns$, the curves in graph a) follow a symmetric behavior to both sides. Without any difference between increasing or decreasing T_{MP} from its default value, the degradation in the signal contrast is mainly a loss-driven feature and not connected to other effects, e.g. in pulse formation due to dispersion. With a mismatched T_{MP}, the optical gates are applied slightly off to the actual arrival times of pulses at the AOM inducing increased gating losses over consecutive round trips. The finite duration of the optical gates still maintains lasing over some range. Whereas the peak level in graph a) has a broad operation window, the ASE background level benefits sharply from a well matched T_{MP}. The resulting signal contrast follows a nearly linear degradation (in logarithmic scale) with any mismatch. For a detuning of $|\Delta T_{MP}| > 10\,ns$, the signal contrast drops below $10\,dB$ killing laser operations. With this setting, laser pulses run non-resonant to the optical gates within 3-4 round trips, prohibiting pulse formation. This matches well to the discussed starting behavior of the TCFL in Fig. 3.16. If a threshold limit of $25\,dB$ in the signal contrast is applied, the investigated TCFL has a working window of 1% that T_{MP} needs to be matched to the PRTT.

With this working window being enabled by the finite optical gate widths in the first place, its range depends on the adjusted gate widths τ_{GW}. Graph b) in Fig. 3.18 plots three curves of

the spectral signal contrast recorded for different τ_{GW}. Two effects become apparent. Firstly, fitting to the discussed behavior, the operation window in T_{MP} becomes broader for increasing GWs. With broader optical gates, the TCFL gets more resilient to detuning in T_{MP}. Secondly, larger GW enable higher signal contrast. Due to a comparably large rise time of the non-PM AOM ($t_R \approx 25ns$, see Fig. 3.4a), larger GW enhance the peak transmission reducing losses and ultimately enhancing the signal contrast.

Underlining the importance of a proper working range in T_{MP}, it crucially enables tunable operation in the TCFL with a constant T_{MP}, i.e. PRR, over the full tuning range. Based on the investigated resonator configurations, dispersion-based variations in T_{RT} are in the order of $< 1\,ns$ over typical tuning bandwidths of rare-earth doped active fibers (see subsection 4.1.2).

In graph c) of Fig. 3.18, the temporal pulse amplitude is plotted in linear scale for three different GWs, varying ΔT_{MP} as before. The reduced sensitivity for detuning T_{MP} is resembled for increasing GW. Matching to the spectral signal contrast, the pulse amplitude also peaks around $\Delta T_{MP} \approx 0\,ns$. However, analyzing the center range in detail, the temporal amplitude features a sharp local minimum being surrounded by a maximum on each side. This is connected to the pulse shape variations with T_{MP} as discussed in subsection 4.1.2. Only at $\Delta T_{MP} = 0\,ns$, a symmetric parabola-like pulse shape is observed. For mild detuning in T_{MP}, the pulse becomes slightly asymmetric with a steepening effect reducing the duration τ_{pulse}. This results in enhanced amplitudes. Stronger detuning in T_{MP} again degrades losses quickly reducing the pulse amplitude.

3.3.3.2 Gate widths

The gate width τ_{GW} electrically controls the duration of the transmission windows at the modulator. Its impact of specific emission properties is highlighted in Fig. 3.19. The measurements are averaged over the accessible tuning range of the non-PM TCFL with FBG array B.

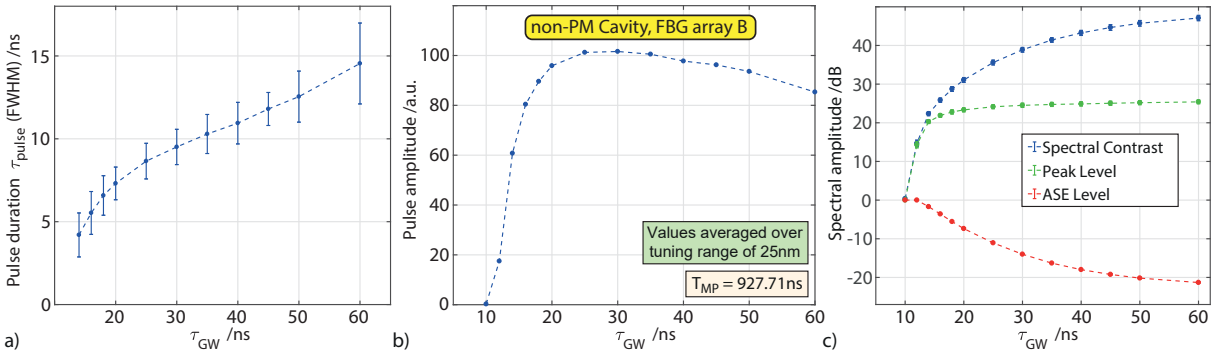

Fig. 3.19: The impact of specific emission properties is illustrated regarding adjusted widths τ_{GW} of both optical gates. Plot a) features the pulse duration, plot b) the pulse amplitudes, and part c) illustrates the spectral signal contrast (blue trace) obtained by subtracting the ASE background peak level (red trace) from the peak amplitude level (green trace). The values are averaged over the operating tuning range.

Setting the strength of temporal filtering, τ_{GW} provides means to electrically tune the pulse duration τ_{pulse}. This is experimentally demonstrated in Fig. 3.19a). The gate width has been varied from $14\,ns$ to $60\,ns$ directly adjusting the pulse duration between about $4\,ns$ to $15\,ns$. This behavior has already been observed in the tunable sigma-ring cavity achieving a larger

tuning range of $10\,ns$ to $60\,ns$ [143]. Due to higher losses and double temporal filtering, pulse durations and their tuning potential reduced in the TCFL. Nevertheless, this feature provides additional freedom in remote-controlling the emission properties of the TCFL in order to flexibly tailor them to the demands of applications.

As shown in graph b), this characteristic also impacts the pulse amplitude (at a constant pump power level). The trace shows a peak value at about $30\,ns$ determining the best compromise between shorter pulses for large peak power as well as decent losses at the AOM due to the limited rise time. For $\tau_{GW} < 25\,ns$, severe IL start to kick in at the AOM ($t_R \approx 25ns$, see Fig. 3.4a) degrading the output power. At $\tau_{GW} = 10\,ns$, lasing cannot be maintained anymore. The strong rise of IL at the AOM in this regime also explains the disruption from the linear relation between τ_{pulse} and τ_{GW} for $\tau_{GW} < 25\,ns$ in graph a). In the range $\tau_{GW} > 40\,ns$, IL at the AOM do not vary so much with τ_{GW} but pulses still extend slowly causing the amplitude to decline again. Due to this behavior, τ_{GW} is mainly operated between $25\,ns$ and $35\,ns$.

Similar as in Fig. 3.18a), Fig. 3.19c) depicts the behavior of the spectral signal contrast (blue trace) calculated as difference of the spectral peak amplitude (green trace) and ASE background (red trace). Due to the described loss behavior at the AOM with declining GW, the spectral contrast in the laser signal rises for increasing τ_{GW}. While at $\tau_{GW} < 25\,ns$, the incline happens quickly, it gradually saturates for values $\tau_{GW} > 40\,ns$ following the transmission behavior of the AOM. In this range, the loss sensitive ASE background still reduces slowly towards saturation.

3.3.4 Summary

In this section, tunable operation in the TCFL has been established demonstrating a wide tuning bandwidth of up to $50\,nm$ solely limited by the employed FBG array. Avoiding the discussed peripheric operation regimes in the resonator, the tuning approach features excellent emission properties over the full tuning range. The tuning characteristics follow the discrete spectral characteristics of the FBG array without any parasitic emission lines confirming the tight locking of laser oscillations to the filter feedback. The tuning mechanism enables an excellent spectral signal contrast, reaching values beyond $45\,dB$, and narrow linewidths ($< 150pm$). Depending on the OC position, signals with decent output power ($\sim 100\,mW$ at OC1) or without any broad ASE background (OC2) can be extracted. Extending the prospects of the tuning approach, the impact of the optical gating parameters has been investigated providing some potential to finely tune the temporal emission properties. This concerns the pulse duration, which is adjusted via the gate widths τ_{GW} of the transmission windows, as well as the repetition rate defined by the modulation period. Whereas for the given experimental configuration, a working window of $\pm 1\%$ has been confirmed for T_{MP} to establish laser oscillations in the TCFL, the RF spectrum analysis confirms the repetition rate to perfectly follow the applied modulation period along the tuning range. With the fast starting behavior establishing the spectrally filtered pulses over a few round trips, the TCFL also qualifies for applications demanding elevated sweep speeds beyond $10\,kHz$.

4 Advanced operation concepts of the TCFL

The concept of the fiber-integrated TCFL combines various unique properties, such as the programmable operation enabled by the optical gating approach, and the prospect for tailored tuning ranges due to the discrete filter design. They provide the basis to target advanced operation regimes of the TCFL beyond a plain tunable single-wavelength light source. Highlighting the flexibility of the presented laser concept, in the following, two examples are discussed to extend and generalize this tuning approach. These advanced operation concepts provide the potential to access further application fields. In the first part, the correlation between pulse shape variations and the applied modulation period T_{MP} is investigated introducing a new method for the direct measurement of fiber dispersion properties. In the second part, independently tunable multi-wavelength emission of synchronized pulses is studied based on modifying the driving optical gating signal of the TCFL.

4.1 Dispersion analysis of fibers

During the investigation of the tunable 1-λ emission, pulse shape variations have been observed depending on the applied modulation period T_{MP}. In the following, this effect is studied more extensively tracking its origin in the fiber dispersion over one round trip evolving along the tuning range. Conducting a numerical and experimental study for a particular fiber under test, the prospect is highlighted to exploit this feature for establishing a novel method to characterize the dispersion of unknown fibers with a plain and direct temporal measurement.

4.1.1 Motivation

As introduced in subsection 2.1.3, the fiber dispersion is a crucial physical property required to describe the propagation of short pulses through a system. The characterization of fiber dispersion has created growing attention with the rise of mode-locked fiber lasers generating pulse durations in the picosecond and femtosecond regime with an extended linewidth. One of the key design challenges concerns the dispersion management determined by the characteristics of each component [45]. The overall cavity round-trip dispersion dictates the pulse formation process setting the operation regime of ultrashort pulsed lasers. Furthermore, tailored dispersion designs enable fibers to drive subsequent spectral broadening and simultaneous pulse compression down to the single-cycle regime [10]. Harvesting the full potential of nonlinear interactions in waveguides, fiber-based super continuum generation is governed by the dispersion properties accessing multi-octave spanning emission bandwidths [36, 66]. On the other side, specific fibers in telecommunications are designed with low dispersion to suppress pulse broadening limiting the bandwidth in data transition.

The importance of fiber dispersion in the design of pulsed sources created a significant demand for experimental characterization. Most methods rely on an indirect measurement, such as in white light interferometry [121] or spectral phase interferometry [34]. While they usually require only

short lengths of fibers and operate over extended bandwidths, they employ elaborate analysis procedures to retrieve the fiber dispersion. Additionally, interferometry-based approaches are prone to environmental influences demanding protected lab conditions. On the other side, a direct temporal measurement is known based on the pulse delay technique [26]. The difference in propagation time through the fiber for pulses at various wavelengths is measured corresponding to the dispersion. Due to the small time scales, hundreds of meters of fiber length are required (temporal resolution in the range of $50\,ps$) [25].

By analyzing the dispersion dependency with a direct measurement during the pulse formation process within the TCFL, a higher sensitivity regarding the required fiber lengths could be possible with the novel approach.

4.1.2 Pulse shape variations over the tuning range

Based on two counter-propagating filter interactions in each round trip, the theta cavity layout enables FBG array tuned lasers operating with a steady physical resonator length over the tuning range. Accordingly, with solely the gating delays (e.g. τ_{1-2}) controlling the emission wavelengths, a constant modulation period of the optical gating signal can be applied. This is supported by Fig. 3.18 demonstrating an extended operation window in T_{MP} to maintain laser operations at each λ_L. A rather rough matching accuracy is required to the actual PRTT within a $\sim 1\,ns$ zone to preserve high spectral signal contrast. Additionally, as demonstrated with the RF analysis in Fig. 3.17, the repetition rate of the laser precisely follows T_{MP} enabling a constant PRR over the tuning range. Concluding on both analyses, the operation window in T_{MP} provides some flexibility to tune the PRR without significant impact on spectral emission properties.

The insensitive behavior of the RF power spectrum with respect to actual emission wavelength is not trivial. While the TCFL layout matches the physical resonator length for all λ_L, it does not compensate for fiber dispersion effects impacting on the optical path lengths in the resonator. Still, the TCFL adapts to the master clock driving the optical gating signal due to steady temporal filtering. On the other side, a clear sensitivity of the precise T_{MP} on the actual pulse shape has been observed. This effect is depicted in Fig. 4.1. It will provide the foundation to analyze the net cavity dispersion.

Fig. 4.1a shows three pulse shapes recorded with a steady emission wavelength ($\lambda_L = 1047\,nm$, PM TCFL) for incrementally varied T_{MP}. The green trace shows a parabola-like symmetric pulse shape which is connected to the default modulation period $T_{MP,0} = 412.978\,ns$ at this λ_L, supposedly matching the precise PRTT. The blue and red trace feature asymmetric pulses correlating with a detuned T_{MP}, i.e. $\Delta T_{MP} = T_{MP} - T_{MP,0} \neq 0\,ps$. Graphs b) and c) depict the same scenario recorded along the tuning range at different emission wavelengths. In each case $T_{MP,0}$ is updated to ensure symmetric parabola-like pulses at the respective λ_L. The traces for $\Delta T_{MP} = T_{MP} - T_{MP,0} \neq 0$ show the same characteristic pulse steepening features as in graph a).

The origin of the observed pulse deformations at $\Delta T_{MP} \neq 0\,ps$ is connected to a weak mismatch in the applied modulation period at the modulator to the precise PRTT in the resonator at the

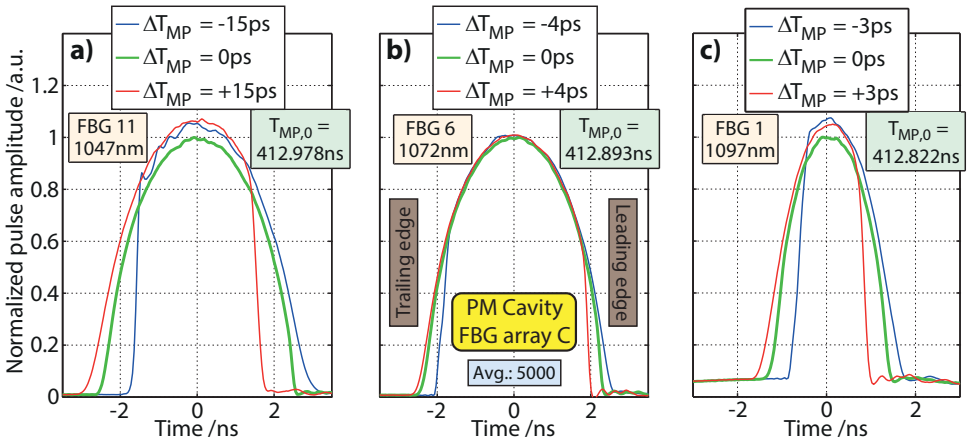

Fig. 4.1: Graph a) plots pulse shapes emitted at OC1 by the PM TCFL locked to FBG 11 (beginning of spectral tuning range) of FBG array C. The three traces correspond to three different modulation periods indicated by the detuning $\Delta T_{MP} = T_{MP} - T_{MP,0}$. The central modulation period $T_{MP,0}$ at FBG 11 ($\lambda_L = 1047nm$) ensures symmetric parabola-like pulses whereas detuning $\Delta T_{MP} \neq 0\,ps$ causes steepening on either side. Graphs b) and c) show corresponding features measured at FBG 6 at $\lambda_L = 1072\,nm$ (center of tuning range) and FBG 1 at $\lambda_L = 1097\,nm$ (end of tuning range). With the changing emission wavelengths from graph a) to c), the central modulation period $T_{MP,0}$ decreases by $156\,ps$.

corresponding wavelength. In the regime of negative ΔT_{MP}, the trailing edge of the pulses shows some steepening. In an illustrative picture, this is explained by repetitive pulse clipping at the modulator applying the optical gating signal. In this regime of $T_{MP} < T_{MP,0}$, the modulation period is smaller than the actual PRTT in the cavity causing the trailing edge of the pulse to get slightly clipped by the transmission windows. In contrast, for $T_{MP} > T_{MP,0}$, the leading edge experiences clipping because pulses arrive at the modulator prior to the opening of the optical gates. Notably, those pulse variations can be reliably observed for detuning in T_{MP} of less than $|\Delta T_{MP}| = 5\,ps$ indicating a sensitivity of this effect in the lower picosecond scale.

Importantly, the shift in the emission wavelength from Fig. 4.1a to Fig. 4.1c correlates with a drift in $T_{MP,0}$ that has been verified for each spectral tuning step. Over the tuning range of $50\,nm$, it decreases by $\Delta T_{MP,0} = -156\,ps$. The origin of this dependency is found in the net cavity dispersion dominantly defined by the fiber characteristics. While the sign of the shift (decreasing $T_{MP,0}$ for increasing wavelength) fits to the normal dispersion regime ($D_\lambda < 0$) at $1\,\mu m$, the magnitude in $\Delta T_{MP,0}$ can be theoretically estimated by the relation

$$\Delta T_{MP,0} \approx D_\lambda \cdot L \cdot \delta\lambda_L \ . \tag{4.1}$$

Assuming a single mode step-index fiber similar to the models employed in the PM TCFL, a typical dispersion parameter is given by $D_\lambda = -38\frac{ps}{nm \cdot km}$ (specified at $\lambda = 1060\,nm$ for `Corning HI 1060` fiber, [1]). Based on $T_{MP} \approx 413\,ns$, the resonator length is estimated by equation(2.13) to $L = 85\,m$ ($n_{gr,eff} \approx 1.45$). Along the tuning range of $\delta\lambda_L = 50\,nm$ in the PM TCFL, the expected shift in $T_{MP,0}$ is computed to $\Delta T_{MP,0} = -161.5\,ps$ matching the experimental measurement within a deviation of 3.5%. Accordingly, the observed shift in $T_{MP,0}$ may be explained by the fiber dispersion. It induces slightly different propagation speeds of the pulses along the tuning range resulting in a drift of the precise PRTT in the TCFL. Matching to this claim, the direction of pulse shape variations is inverted in the $2\,\mu m$ emission band, which

has been verified with a Tm-doped TCFL. Due to anomalous dispersion ($D_\lambda > 0$) in this regime, $T_{MP,0}$ increased with the emission wavelength. With a dispersion managed cavity layout aiming for a vanishing mean D_λ, the TCFL could work at a steady default modulation period along the tuning range. Due to the comparably broad operation window in T_{MP}, this is not relevant for most application fields.

For further analysis, a quantitative measure is required to grasp the pulse shape variations and objectively determine $T_{MP,0}$ along the tuning range of λ_L. Comparing the pulse shapes in the graph of Fig. 4.1, two main characteristics may be utilized: while the pulse amplitude tends to increase for detuned $T_{MP} \neq T_{MP,0}$ due to the steepening effect shortening the pulses, the shape also shows higher asymmetry as noted before. The asymmetry in the pulse shape Pulse(t) can be analyzed by a normalized self-convolution I_C as defined by

$$I_C(t) = \frac{\int_{-\infty}^{+\infty} \text{Pulse}(\tau) \cdot \text{Pulse}(t-\tau) d\tau}{\int_{-\infty}^{+\infty} \text{Pulse}(t) \cdot \text{Pulse}(t) dt} \,. \tag{4.2}$$

Whereas the denominator normalizes the result by the equivalent of the pulse energy, the negative τ for the second factor in the nominator reverses the pulse shape so that the integral is maximized for highest symmetry in Pulse(t). The integration borders are formally given by $-\infty$ and $+\infty$, but in the experiment, the function is limited by the length of the recorded trace.

For maximized synchronicity in the pulses, the peak of $I_C(t)$ needs to be maximized. Accordingly, to automatically retrieve $T_{MP,0}$ at a given emission wavelength of the TCFL, T_{MP} is scanned in fine increments recording the respective pulse traces Pulse(t). For each measurement, the peak value $\widehat{I}_C$ of $I_C(t)$ is determined. Plotting $\widehat{I}_C$ along the scanned range in T_{MP} gives an overall maximum, matching $T_{MP,0}$ with the highest pulse symmetry.

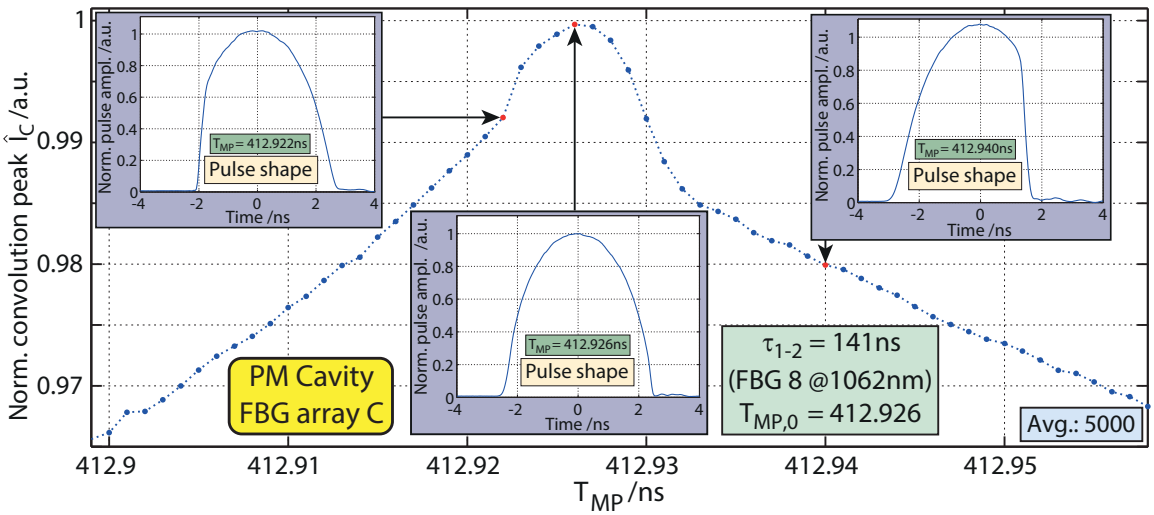

Fig. 4.2: The main graph plots the convolution trace depending on T_{MP} recorded with the PM TCFL exemplarily locked to FBG 8. Inset graphs highlight the correlation with pulse shape variations along the curve. The peak of the correlation curve matches $T_{MP,0}$ resulting in a symmetric parabola-like pulse shape.

Fig. 4.2 evaluates the behavior of the normalized convolution peak for a fixed emission wavelength of $\lambda_L = 1062\,nm$. The evolution of $\widehat{I}_C(T_{MP})$ is correlated with the corresponding pulse shapes plotted in three inset graphs. As shown with the center inset graph at $T_{MP} = 412.926\,ns$, the maximum of $\widehat{I}_C$ results in a symmetric parabola-like pulse shape defining $T_{MP,0}$ for this emission wavelength. The maximum value of the normalized convolution peak curve approaches 1, indicating high overall symmetry. Reducing T_{MP} at the AWG by $4\,ps$ (left-hand side inset), the pulse shape features mild onset of steepening at the trailing pulse edge. For increasing T_{MP} by $14\,ps$ from the default value, stronger steepening occurs on the leading edge. It has also been verified that similar values in $\widehat{I}_C(T_{MP})$ to either side of $T_{MP,0}$ show similar strengths in the steepening of the pulse shape. The overall shape of the curve is monotonic in both sides of the maximum peak level, respectively, indicating a well behaving criterion without local extrema.

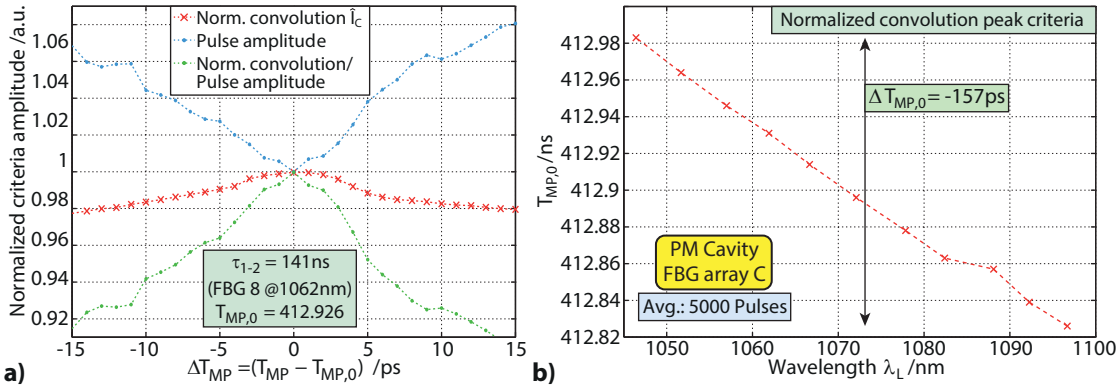

Fig. 4.3: Plot a) compares three exemplary features to quantify the pulse shape variations with T_{MP} computed for a measurement at $\lambda_L = 1062\,nm$ (FBG 8). The blue trace tracks the normalized pulse amplitude, the red trace the normalized convolution peak criterion and the green trace a combined value dividing the convolution criterion by the corresponding normalized pulse amplitude. The extrema in each curve coincide at $T_{MP,0}$. Graph b) depicts a measurement of the default modulation period $T_{MP,0}$ for each emission wavelength of the PM TCFL (different conditions as in graph a), highlighting the evolution along the tuning range due to dispersion. The normalized convolution peak criterion was employed for the automated measurement sampling T_{MP} in increments of $1\,ps$.

Fig. 4.3a compares different criteria to analyze the pulse variation versus the detuning ΔT_{MP}. They are investigated to retrieve $T_{MP,0}$ at a given wavelength. The graph is obtained exemplarily at $\lambda_L = 1062\,nm$. Whereas the red trace corresponds to the previously discussed convolution peak criterion, the blue trace depicts the normalized pulse amplitude. It increases for detuning in T_{MP} within the plotted range due to the asymmetric steepening effect. The minimum coincides with the maximum of the convolution trace resulting in a matching value in $T_{MP,0}$. Based on both characteristics, a joint criterion (green trace) is also added by dividing the normalized convolution peak by the pulse amplitude achieving stronger sensitivity. However, whereas all criteria agree well proving their applicability, the pulse amplitude criterion shows small deviations from the monotonic behavior to both sides from the minimum. In other examples, those deviations appeared stronger giving multiple maxima that degraded the reliability in determining $T_{MP,0}$. This behavior also transferred to the combined criterion (green trace). Hence, despite the increased computational effort and limited sensitivity, the monotonic behavior in the normalized convolution peak function is chosen as robust criterion to further analyze pulse shape evolution and track down $T_{MP,0}$ along the tuning range by also scanning τ_{1-2}.

An exemplary measurement is featured in Fig. 4.3b. The drift in $T_{MP,0}$ has been investigated along the tuning range of the PM TCFL applying the normalized convolution peak criterion. It proves a clear shift in the default modulation period with each discrete spectral step indicating a nearly linear behavior over this spectral bandwidth. Merely the point at $\lambda_L = 1087nm$ deviates due to a measurement artifact (for instance caused by a varying FBG reflectivity). In good agreement to the analysis in Fig. 4.1, the overall shift $\Delta T_{MP,0}$ obtained with this fully automated measurement routine amounts to $-157\,ps$ corresponding to the dispersion characteristics of the overall cavity. This analysis provides the basis to investigate the dispersion of an arbitrary fiber-under-test (FUT) as discussed in subsection 4.1.4.

4.1.3 Numerical simulation of dispersion in step-index fibers

The dispersion properties of the employed fibers in the TCFL are not provided by the manufacturer and barely mentioned in literature. In order to obtain reference data, numerical simulations are conducted to model the dispersion behavior of the employed fibers based on their released specifications. A modal analysis has been performed with a commercial mode solver implemented in `COMSOL Multiphysics`® to compute the effective refractive index n_{eff} of the fundamental mode (LP_{01}). By scripting the procedure with `MATLAB`, the spectral operation window of the TCFL at around $1\,\mu m$ was scanned to obtain the spectral dependency in $n_{eff}(\lambda)$ concealing the information about the fiber dispersion properties.

The fibers are modeled by an idealized step-index profile as shown in Fig. 2.1. Any substructures in the coating, such as stress elements of the PM layout, are neglected due to a weak impact on the core mode. Assuming undoped silica as typical cladding material, the refractive index n_{clad} is modeled by fused silica. The chromatic material dispersion is considered by the corresponding Sellmeier equation (parameters at a temperature of 20°C given in [98]). The core refractive index is calculated based on the specified core-NA of the corresponding fiber by applying equation(2.1). Due to the typically weak doping concentration of the silica-based core, any dispersion effects in the core-NA are neglected. The fiber dimensions, i.e. r_{core} and r_{clad} are taken from the specifications of the corresponding fibers.

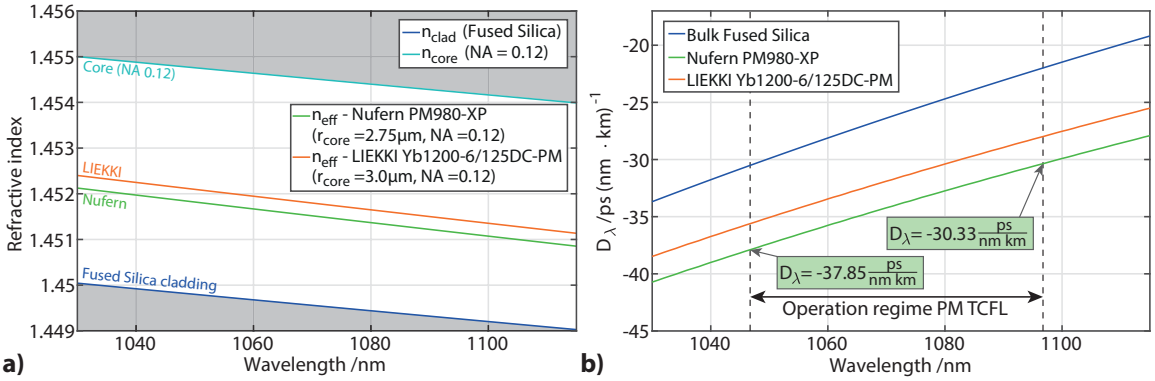

Fig. 4.4: The graphs depict the results from the modal analysis of two step-index fibers from the PM TCFL (`Nufern PM980-XP`, `LIEKKI Yb1200-6/125DC-PM`) computed by `COMSOL Multiphysics`® and `MATLAB`. Plot a) pictures the calculated effective refractive indices of the fundamental modes along the wavelength scale. Graph b) shows the corresponding dispersion analysis plotting the dispersion parameter D_λ versus the wavelength for bulk silica as well as the two fibers.

Studying the dispersion impact mainly in the PM TCFL, two fibers are analyzed numerically, forming major parts of the cavity. Namely, the passive fiber `Nufern PM980-XP` and the YDF `LIEKKI Yb1200-6/125DC-PM` are investigated with the specifications provided in [2, 3]. The fiber `Nufern PM980-XP` is also studied experimentally with the TCFL in subsection 4.1.4. Fig. 4.4a shows the calculated n_{eff} for both fibers versus the wavelength. Fiber parameters are provided in the legend. Additionally, the corresponding core and cladding refractive indices are included. As expected for guided core modes, they frame the theoretical limit for the traces of the computed fibers ($n_{clad} < n_{eff} < n_{core}$, see subsection 2.1.3). Matching to the larger core size, the LIEKKI fiber exhibits a slightly larger n_{eff}.

Based on the retrieved $n_{eff}(\lambda)$, the fiber dispersion is computed by applying equation(2.16). The results for both fibers are shown in Fig. 4.4b. In order to highlight the pure contribution of material dispersion (based on $n_{clad}(\lambda)$), the computed dispersion curve of bulk fused silica is added (blue trace). The deviation to the green and orange trace, depicting the overall dispersion of both fibers, is caused by the waveguide dispersion. Due to the smaller core size and tighter confinement, the `Nufern` fiber features a stronger waveguide dispersion.

Considering the tuning range of the PM TCFL with FBG array C, the operation window is highlighted by two black dashed lines. With the `Nufern` fiber as the most prominent fiber in the laser design, the corresponding values for D_λ are noted on the edges of the tuning range. This results in a mean dispersion parameter over the tuning range of $D_{\lambda,theor.} = (34.09 \pm 1.75)\frac{ps}{nm \cdot km}$, which will be compared to the experimental measurement in subsection 4.1.4. The inaccuracy of the simulation results is derived based on tolerances in the fiber specifications (assuming $r_{core} = (2.75 \pm 0.25)\mu m$ and $NA = 0.12 \pm 0.01$). The corresponding tolerance traces in D_λ are plotted in Fig. 4.6b.

4.1.4 Dispersion measurement of fibers in the TCFL

The high sensitivity of the pulse shape variations to the actual T_{MP} may be exploited to measure the dispersion of optical fibers. This will be discussed based on the investigation of two fiber samples FUT1 and FUT2. Providing a reference to the numerical simulation results (subsection 4.1.3), they are from two different batches of the fiber model `Nufern PM980-XP`.

Measurement procedure

To measure the dispersion of a specific FUT in the TCFL, two experiments are conducted. In a first step, the plain TCFL is analyzed considering its characteristic overall dispersion behavior as reference measurement. Thus, the unknown properties of other components in the cavity, such as the modulator and circulator, are also taken into account for. In the second step, a FUT is spliced to the TCFL extending the resonator. By comparing the dispersive character of both cavities, the dispersion of the FUT can be isolated, excluding any effect from the other resonator parts. For both layouts, the TCFL is tuned in discrete steps of τ_{1-2} through the spectral tuning range of the FBG array. For each step, a sub-scan in T_{MP} is conducted measuring the averaged pulse shapes of the emitted signals. By applying the normalized convolution peak criterion for each spectral tuning step, the evolution of the default modulation period $T_{MP,0}(\lambda)$ is retrieved.

Applying this procedure for both, the reference cavity and the cavity with the FUT, the sole dispersive response of the FUT can be evaluated.

Fig. 4.5 illustrates this process for the example of analyzing FUT1 and FUT2. Graph a) shows three traces corresponding to the plain reference cavity (red) as well as this TCFL extended by FUT1 (blue) and FUT2 (green), respectively. Both samples are spliced at the position of delay fiber 1 as marked in Fig. 3.3. Being located in the middle branch, their effective length doubles potentially offering higher sensitivity in the measurement. Because the resonator lengths between the three measurements differ strongly, the modulation period operates at different magnitudes for each case. Due to the dissimilar time scales, the measurements of FUT1 and FUT2 are highlighted in the insets zooming in on the respective traces. The evolution of $T_{MP,0}$ considering the dispersive character of the overall cavity follows the discussion for Fig. 4.3b. The inset graphs confirm the shift of $T_{MP,0}$ over the tuning range.

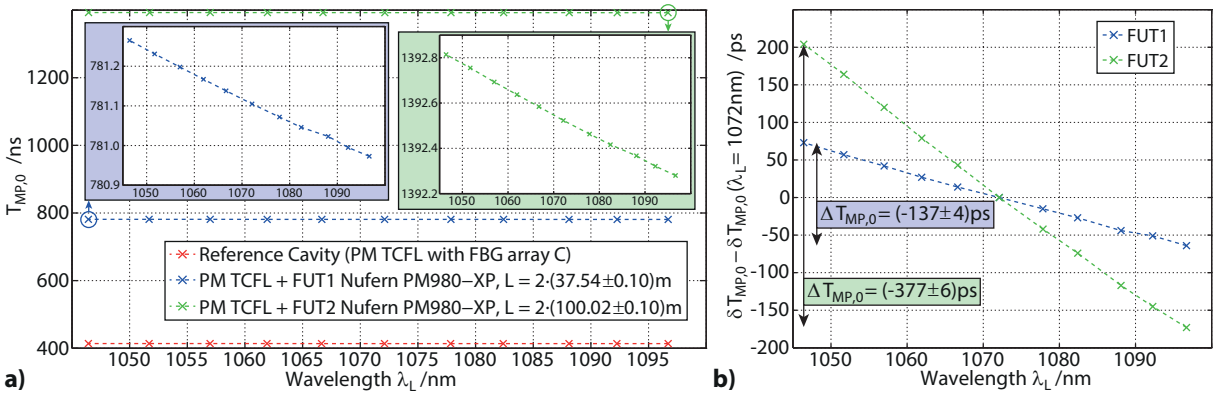

Fig. 4.5: The graphs analyze the evolution of $T_{MP,0}$ over the tuning range for two FUT samples. Graph a) shows the measured $T_{MP,0}$ for the PM TCFL in the reference layout as well as with two FUT samples. Two inset graphs highlight the detailed trace for FUT1 (blue) and FUT2 (green). Plot b) pictures the evaluated relative change $\delta T_{MP,0}$ by subtracting FUT1 as well as FUT2 from the reference measurement. By also subtracting $\delta T_{MP,0}(\lambda_L = 1072\,nm)$ measured at FBG 6 (considers the mean change in $T_{MP,0}$ due to the additional fiber length), the plain dispersion effect is isolated for FUT1 ($\Delta T_{MP,0} = (-137 \pm 4)ps$) and FUT 2 ($\Delta T_{MP,0} = (-377 \pm 6)ps$). The error bars are estimated from the convolution curves considering their slopes as well as reproducibility.

In order to isolate the sole dispersive contribution of the corresponding FUT sample, the reference trace (red) in Fig. 4.5a is subtracted from the corresponding measurement trace of FUT1 as well as FUT2. The result is the absolute change $\delta T_{MP,0}(\lambda)$ induced in $T_{MP,0}$ by the FUT. This is illustrated for both fiber samples in Fig. 4.5b. Either trace is also corrected by an offset value ($\delta T_{MP,0}$ at $\lambda_L = 1072\,nm$) considering the different fiber lengths. Accordingly, the dispersive contribution for both measurements can be analyzed in the same time scale. The curves, depicting the isolated dispersive response of the fiber samples, show a nearly linear behavior linked to the comparably small measurement bandwidth. Due to the longer length, the effect of FUT2 is significantly larger. It features a larger slope inducing a shift in $T_{MP,0}$ by $\Delta T_{MP,0} = (-377 \pm 6)ps$. The negative sign considers the declining evolution. In comparison, FUT1 causes a drift by $\Delta T_{MP,0} = (-137 \pm 4)ps$. The errorbars are estimated from the convolution curves by evaluating reproducibility and slope. The error in $T_{MP,0}$ for the samples in Fig. 4.5a is about $\pm 1\,ps$ (matching the sampling density) for the red and blue trace, and $\pm 2\,ps$ for the green trace. The larger absolute error in the measurement of FUT2 is connected to a reducing

sensitivity of the pulse shape variations for longer cavities. This is highlighted in Fig. 4.6a depicting the convolution peak ($\widehat{I}_C$) traces for a specific λ_L at different resonator lengths versus the normalized change of the modulation period on the x-axis. Longer resonator lengths (i.e. larger $T_{MP,0}$) seem to level off the pulse asymmetry effects with detuning in T_{MP}. Thus, while longer fibers are expected to reduce the relative measurement errors due to a stronger absolute dispersion impact of the FUT, this effect is partly counterbalanced by a reduced accuracy in the recorded $T_{MP,0}$. Enlarging the fiber lengths of the FUT does not improve the measurement accuracy in the same magnitude.

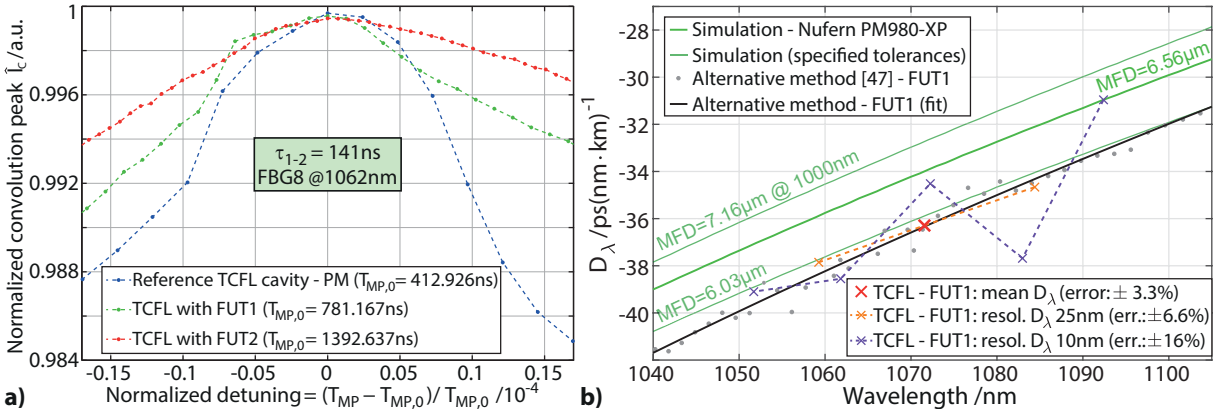

Fig. 4.6: Graph a) shows the sensitivity of the employed convolution peak criterion on the normalized detuning magnitude in T_{MP} for different resonator lengths of the PM TCFL. The traces indicate a reducing slope of the normalized convolution peak curve for larger mean $T_{MP,0}$ (i.e.: longer resonators). Plot b) shows the measured dispersion parameter D_λ for different spectral resolutions (resol.) applying the TCFL. The simulation results based on `COMSOL Multiphysics`® (including an error analysis with the specified tolerances of the `Nufern PM980-XP` and the corresponding MFD at 1000 nm) as well as the dispersion values measured for FUT1 with an alternative experimental method [47] (recorded D_λ points as well as fitted dispersion curve) are attached as references. Considering the limited resolution of the TCFL analysis, the graph confirms excellent agreement between both experimental measurements and some offset to the plain simulation model.

Data evaluation

With the measured values in $\Delta T_{MP,0}$ directly correlating with the dispersive response of the FUT, the mean dispersion of the samples can be calculated based on the experimental data obtained with the TCFL. Solving equation(4.1) for D_λ gives the relation

$$D_\lambda \approx \frac{\Delta T_{MP,0}}{L \cdot \delta\lambda_L} \tag{4.3}$$

to compute the effective fiber dispersion for FUT1 and FUT2 over the tuning range $\delta\lambda_L$ via a linear approximation. Prior to the measurement, the length L of the fibers is precisely determined with a spooling machine. The double pass arrangement in the middle branch is considered by doubling the measured lengths. The results of the experiments are summarized in table 4.1.

While FUT1 features a slightly smaller dispersion ($D_{\lambda,exp.} = (-36.3 \pm 1.2)\frac{ps}{nm \cdot km}$) compared to FUT2 ($D_{\lambda,exp.} = (-37.5 \pm 0.7)\frac{ps}{nm \cdot km}$), both values roughly agree within their combined measurement accuracy. FUT2 features a smaller relative error of ±1.9% due to the longer fiber length. Recalling the simulated value $D_{\lambda,theor.} = (34.09 \pm 1.75)\frac{ps}{nm \cdot km}$ for the `Nufern PM980-XP` fiber, the experimental results indicate larger absolute dispersion values compared to

Parameter	**FUT1**	**FUT2**
L	$2 \cdot (37.54 \pm 0.10)m$	$2 \cdot (100.02 \pm 0.10)m$
$\delta\lambda_L$	$(50.27 \pm 0.04)nm$	$(50.27 \pm 0.04)nm$
$\Delta T_{MP,0}$	$(-137 \pm 4)ps$	$(-377 \pm 6)ps$
$D_{\lambda,exp.}$	$(-36.3 \pm 1.2)\frac{ps}{nm \cdot km}$	$(-37.5 \pm 0.7)\frac{ps}{nm \cdot km}$
relative error in $D_{\lambda,exp.}$	3.3%	1.9%
$D_{\lambda,exp.}$ (alternative method [47])	$(-36.4 \pm 0.3)\frac{ps}{nm \cdot km}$	$(-37.0 \pm 0.3)\frac{ps}{nm \cdot km}$

Table 4.1: Experimental results of dispersion measurements including a comparison to an alternative method [47]. For the latter, error bars are estimated from the standard deviation of a polynomial fit (3rd order) to the obtained D_λ values. As presented in subsection 4.1.3, the numerically simulation resulted in a value of $D_{\lambda,theor.} = (34.09 \pm 1.75)\frac{ps}{nm \cdot km}$.

the numerically modeled plain step-index fiber. With a deviation of about 10% and an overall error bar of 7% between both values, FUT2 shows a systematic deviation in the dispersion parameter compared to simulations. In principle, this may be caused by an oversimplified numerical model, deviating fiber specifications or a systematic error in the dispersion analysis with the TCFL. To investigate the origin and validate the measurement with the TCFL, further investigations are discussed in the following.

An example dispersion measurement for the `Nufern PM980-XP` fiber is given in literature [8]. Analyzing the dispersion for a mode-locked fiber ring laser, a GVD parameter of $\beta_2 = 24\frac{ps^2}{km}$ is provided at $\lambda = 1030\,nm$ (without mentioning measurement errors). For comparison to the simulations in subsection 4.1.3, β_2 is extracted from the numerical data at the respective wavelength by applying equation(2.16) and equation(2.17) giving $\beta_2 = 22.96\frac{ps^2}{km}$. Hence, the experimental value in literature also indicates to a larger absolute dispersion of the tested fiber matching to the experimental observation with the TCFL. The deviation between literature and the simulations in subsection 4.1.3 amounts to about 4%.

Still, to verify the measurement results with the TCFL and potentially confirm the small deviation between FUT1 and FUT2, an alternative measurement method has been implemented and applied to both fiber samples. The concept is based on spectral interferometry with a broadband supercontinuum source. The method has been set up based on reference [47] presenting an interferometric setup with a signal arm with the FUT, and a reference arm with a matching optical path distance. Compared to [47], the concept is extended by a polarizer in the path of the light source and a PM fiber coupler as beam splitter for characterizing polarization dependent components such as the `Nufern PM980-XP`. The measurement of the interference trace between signal and reference path is conducted with an OSA. As with the TCFL, the interferometer is calibrated with a reference measurement prior to the investigation with the FUT samples.

Short samples of FUT1 as well as FUT2 (lengths of about $40\,cm$) have been analyzed with this dispersion measurement concept. The results for the effective dispersion parameter $D_{\lambda,exp.}$ extracted for the tuning range of the TCFL are attached to table 4.1. The error bars are estimated by the standard deviation of a polynomial fit to the obtained measurement data not considering any systematic distortions. The obtained values in $D_{\lambda,exp.}$ match well to the measurement results obtained with the TCFL. For both, FUT1 and FUT2, they agree within the corresponding error bars confirming the larger absolute dispersion compared to the numerical

results. The deviation between both experimental methods for FUT1 is about 0.3% and for FUT2 1.3%. Accordingly, the proposed dispersion analysis with the TCFL is verified.

The different experimental dispersion values between FUT1 and FUT2 observed with the TCFL as well as the reference method [47] is connected to different fiber batches sold by `Nufern`. The supplier provided data sheets to the fiber samples revealing different MFDs of 7.1 μm for FUT1 and 6.6 μm for FUT2 (measured at $\lambda = 980\,nm$). The smaller MFD of FUT2 may explain the slightly larger absolute dispersion parameter as experimentally indicated. This is supported by the simulated green dispersion traces included in Fig. 4.6b. All three traces are labeled by the corresponding MFD at $\lambda = 1000\,nm$ extracted from the modal analysis. A smaller MFD of about 500 μm may cause an absolute increase in D_λ of about 5% fitting qualitatively to the deviation between FUT1 and FUT2. Therefore, the difference in $D_{\lambda,exp.}$ between both samples may exhibit a physical origin. More extensive conclusions cannot be drawn based on the obtained measurement accuracies.

With the dispersion measurement in the TCFL confirmed over the full tuning range, the spectral resolvability is investigated based on the provided emission wavelengths in the PM TCFL with FBG array C. While so far, the overall shift $\Delta T_{MP,0}$ has been evaluated over the full tuning range, this value can be also analyzed for intermediate steps in λ_L enabling spectrally resolved dispersion characteristics. The results of this analysis are plotted in Fig. 4.6b for FUT1. FUT2 featured similar characteristics. The graph shows dispersion traces obtained with the TCFL for three different spectral resolutions. While the red cross highlights the overall $D_{\lambda,exp.}$ as provided in table 4.1 (measurement bandwidth: $50\,nm$), the orange trace is analyzed for a spectral step size of $25\,nm$ and the purple trace for a step size of $10\,nm$. For the corresponding analysis, $\Delta T_{MP,0}$ has been evaluated incrementally over the tuning range for the given step size. As an example, the purple trace is obtained by assessing $\Delta T_{MP,0}$ for λ_L locked to the FBG 1, 3, 5, 7, 9 and 11, respectively. The adapted spectral step size is considered via $\delta\lambda_L$ calculating spectrally resolved values for D_λ by equation(4.3). Since the absolute errors in $\Delta T_{MP,0}$ do not scale, the relative inaccuracies increase for higher spectral resolutions as proven in the legend of Fig. 4.6b with the noted error values. For comparison, Fig. 4.6b also includes the simulation results for the `Nufern PM980-XP` fiber (including error traces considering specification tolerances, see subsection 4.1.3) as well as the dispersion curve measured for FUT1 based on the method in [47]. The discrepancy between those two curves proves either shortcomings in the numerical fiber model or deviating parameters of the drawn fiber.

Analyzing the traces of the TCFL in Fig. 4.6b, they match to the black trace measured with the alternative method within the corresponding error bars. However, especially the purple trace obtained for a spectral step size of $10\,nm$ shows significant fluctuations, not following the shape of typical dispersion curves. These deviations to the black trace are caused by the comparably poor resolution in D_λ for such a small spectral step size because the dispersion impact in the TCFL is rather weak over $10\,nm$ increments, transferring to the measurement sensitivity. While scaling the FUT length improves the sensitivity, the degrading slopes in the normalized convolution curve as discussed for Fig. 4.6a may prohibit significantly enhanced resolutions. Accordingly, the dispersion measurement with the TCFL cannot provide spectrally resolved dispersion curves as obtained by competing measurement approaches. The measurement accuracy in D_λ suffers

strongly from small spectral analysis ranges. Nevertheless, the orange curve indicates that the slope of dispersion curves may be obtained over extended spectral ranges.

In conclusion, the experiments proved the applicability of the TCFL to a direct temporal dispersion measurement by evaluating the emitted pulse shapes. With this concept measuring the overall resonator round-trip dispersion, the dispersive properties can be quantified for fiber-optic components as well as specific fiber samples.

Limitations and applicability of dispersion measurements with the TCFL

In any case, the elements under test need to satisfy a few conditions to be suitable for this dispersion measurement approach. Most notably, they need to feature reasonable transmission. The basis of the measurement with the TCFL is to establish laser oscillations in any case. Adding lossy components, such as specific microstructured fibers with high propagation losses, could prohibit to even generate any laser pulses. This criterion is also connected to proper coupling losses, which are usually ensured with decent spliceability of the additional component. Due to overall round-trip losses in the realized TCFL exceeding $20\,dB$, the element under test should feature losses of less than $10\,dB$. In a loss-optimized cavity layout, additional losses of up to $25\,dB$ could be bearable. Also partly connected to the losses, the FUT needs to be available with reasonable length. Due to the direct temporal measurement with limited accuracy (in the experiment: $\geq 1\,ps$), the minimum detectable length is in the range of a few meters. This limit is derived from an example. Assuming a FUT with $D_\lambda = 40ps(nm \cdot km)^{-1}$, a tuning range of $\delta\lambda_L = 50\,nm$ and an effective delay due to the dispersive distortion of $\Delta T_{MP,0} \geq 10\,ps$ for a profound measurement, the minimum length for the FUT is about $5\,m$. Compared to the previously mentioned pulse delay technique [26] working with hundreds of meters of FUT, this is a significantly shorter length of fiber to draw conclusions about the dispersive character with a direct measurement. Including the fiber in the middle branch of the TCFL (e.g. at the position of delay fiber 1, see Fig. 3.3) doubles the sensitivity.

Satisfying these conditions, the element can be characterized within certain conceptual limitations regarding the accessible parameter regimes. The dispersion analysis is spectrally limited to the restricted gain regions of laser active materials, such as rare-earth doped fibers. Thus, octave spanning dispersion curves cannot be obtained with the TCFL approach. This is contrary to methods relying on spectral interferometry working with broadband supercontinuum sources [115]. Additionally, the spectral domain is sampled discretely with the TCFL. Together with the limited sensitivity as shown in the experiment, high spectral resolutions and rapidly evolving dispersion features are not detectable.

On the other side, this concept utilizes a simple measurement of pulse shape features to directly retrieve the dispersion parameter for a component. Compared to other techniques evaluating temporal delays over hundreds of meters of fibers [25], it features a higher sensitivity. The pulse formation process within the TCFL enhances the dispersive effect. Absolute measurement accuracies in the picosecond scale are demonstrated in the experiment without using high-end electronics. The analysis with the TCFL enables the evaluation of resonator round-trip dispersions. For spliceable components, it provides quick and easy access to determine the overall dispersion regime without any additional alignment of a measurement. Furthermore,

when working with PM components, the dispersion in the different axes is also swiftly addressable by splicing it to the operating polarization axis of the TCFL.

In conclusion, the TCFL may not outperform common dispersion analysis concepts in terms of measurement accuracy, bandwidth or applicability. But it provides a simple and neat tool for specific measurement scenarios. If a suitable laser resonator is available, multiple components may be quickly investigated for their coarse dispersion characteristics, e.g. in quality management categorizing their performance. Even solely analyzing the temporal delays (without retrieving D_λ) enables quick conclusions to be drawn about the dispersion regimes. Additionally, with the measurement concept relying on laser operations, the dispersion magnitude of active fibers can be evaluated within their gain region that is commonly absorbing for passive methods. Due to the spectral operation windows, this approach could be of particularly interest for general applications related to fiber lasers.

4.2 Tunable multi-wavelength emission

This part is devoted to a unique operation mode enabled by the TCFL featuring independently tunable multi-wavelength emission of inherently synchronized pulses from a single fiber oscillator. The basis is provided by the constant pulse repetition rate over the tuning range in the theta cavity layout as well as the flexibly programmable optical gating scheme.

In the following, this regime is introduced featuring a modified optical gating function. The experimental demonstration focuses mainly on the investigation of discretely tunable dual-wavelength (2-λ) emission. Besides the discussion of further design challenges for the TCFL, an extensive study of pulse synchronicity is conducted with a modified time-delay spectrometer. This tool enables an enhancement in the pulse overlap between both emission wavelengths to address new application fields, such as nonlinear frequency mixing. Furthermore, scaling the number of emission wavelengths beyond a 2-λ operation is discussed. Parts of the methodology and the results are published in references [141, 145].

4.2.1 Motivation

Multi-wavelength lasers have been reported with diverse filtering techniques including free-space coupled diffraction gratings [42], interferometric transmission filters based, e.g., on an all-fiber Mach-Zehnder configuration [22], superstructured FBGs [157] and cascaded FBG reflectors [61, 90]. In [90], Li et al. employ a similar ring cavity design as presented in this work, however, they rely on polarization-controlled tuning to switch between single-wavelength emission and fixed dual-wavelength emission.

Most research efforts have been directed towards tunable 2-λ sources facing a broad application range that covers, e.g., spectroscopic measurements [50], atmospheric sensing [123] and nonlinear biomedical applications [55] including coherent anti-Stokes Raman (CARS) scattering microscopy [54]. Furthermore, applying tunable 2-λ lasers to pump nonlinear frequency conversion processes, flexibly tunable sources may open up other spectral ranges that are difficult to access with standard gain media. Addressing diverse applications in spectroscopy, dual-wavelength

lasers are used to realize tunable THz [73,130,156] and mid-Infrared (MIR) [51,64,134] sources. Hence, tunable dual-wavelength sources are reported with diverse approaches including the superposition of two laser oscillators [51] or configurations with a free-space-coupled optical parametric oscillator (OPO) [49, 156], all-fiber OPO [55], polarization multiplexing combined with birefringent filters [126,128], and two FBGs with a variable attenuator [95,152].

4.2.2 Concept of multi-wavelength emission

The foundation for tunable multi-wavelength emission in the TCFL is provided by the theta-ring resonator layout that features a steady PRR for each wavelength $\lambda_L = \lambda_{FBG,i}$. Additionally, the optical gating approach can be adapted to drive multiple pulse paths referring to different emission wavelengths.

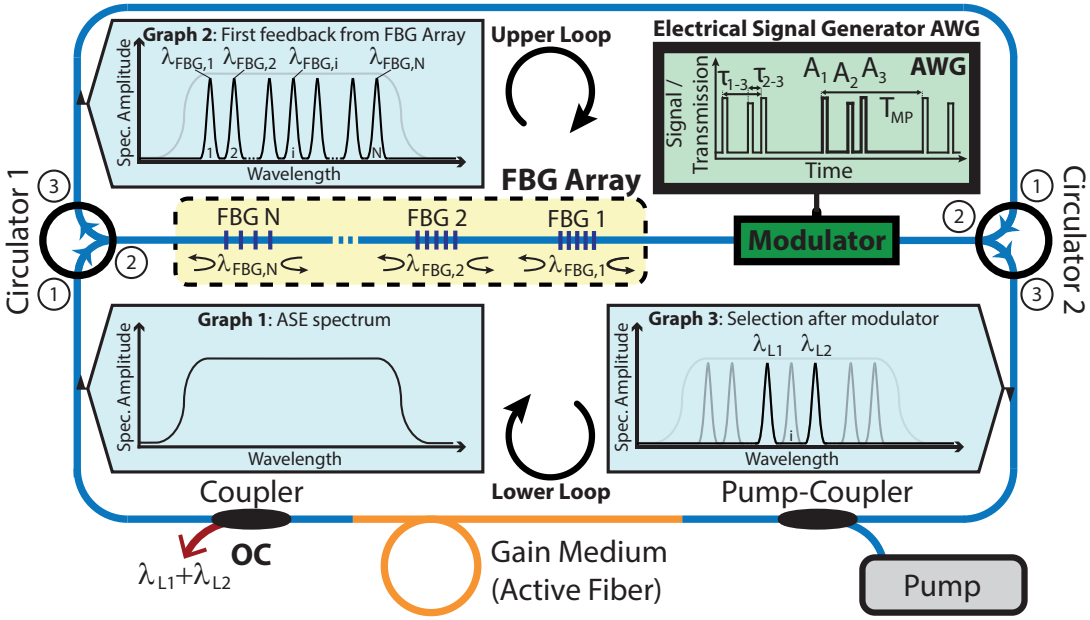

Fig. 4.7: Operation scheme of tunable multi-wavelength emission on the example of two emission wavelengths λ_{L1} and λ_{L2}. Dual-wavelength mode is triggered by optical gating with three transmission windows promoting two response times from the FBG array for low round-trip losses. Whereas the amplitudes are controlled by A_1 to A_3, the wavelengths are independently tuned via τ_{1-3} and τ_{2-3}. Graph 1 to graph 3 sketch spectral pulse formation over one round trip.

As depicted in Fig. 3.1, tunable single-wavelength (1-λ) emission is triggered via two transmission windows at the modulator. Promoting a single response time $T_{filter}(\lambda_{FBG,i})$ via τ_{1-2}, they isolate a single grating response determining λ_L. In contrast, Fig. 4.7 illustrates the operation principle of multi-wavelength emission on the example of dual-wavelength (2-λ) generation in the theta-ring oscillator. The idea is to add an additional third transmission window to the optical gating signal at the modulator. Accordingly, presetting the time of flight in the filter structure, two response times $T_{filter1}(\lambda_{FBG,i})$ and $T_{filter2}(\lambda_{FBG,j})$ can be favored by low round-trip losses providing the basis to lock laser oscillations to two wavelengths $\lambda_{L1} = \lambda_{FBG,i}$ and $\lambda_{L2} = \lambda_{FBG,j}$. In an illustrative picture, the first transmission gate at the modulator injects the pre-filtered spectrum to the FBG array with all the filter lines depicted in graph 2. Each grating reflects the corresponding wavelength returning the ensemble back to the modulator. As

discussed previously, the distributed feedback introduces specific delays $T_{filter}(\lambda_{FBG,i})$ so that each wavelength pulse arrives at a different time at the modulator. In order to promote two wavelengths for lasing, the modulator needs to switch transmission gate 2 and 3 according to the corresponding filter response times $T_{filter1}$ and $T_{filter2}$ to transmit the pulses to the lower loop as highlighted in graph 3 of Fig. 4.7. Exemplarily, $\lambda_{FBG,i-1}$ and $\lambda_{FBG,i+1}$ are sketched as emission wavelengths. Again, laser oscillations build up over multiple round trips with the modulation period $T_{MP} = \frac{T_{RT}}{m}$ ($m \in \mathbb{N}$).

In this framework, the two pulses at $\lambda_{FBG,i}$ and $\lambda_{FBG,j}$ would propagate with a fixed delay $|T_{filter2}(\lambda_{FBG,j}) - T_{filter1}(\lambda_{FBG,i})|$ in the lower loop of the theta-ring resonator. This delay is compensated during the first filter interaction in the succeeding round trip synchronizing both wavelengths in the upper loop. However, without any loss of generality, the OC is exemplarily included in the lower loop as set up in Fig. 4.7. Thus, the inverse operation regime with the two wavelengths running synchronized in the lower loop and delayed in the upper loop is preferred for the study of this mode. Accordingly, the optical gating signal in Fig. 4.7 evolves as follows: the first transmission window gates the wavelength pulse $\lambda_{L2} = \lambda_{FBG,i+1}$ to the FBG array, the second transmission window gates $\lambda_{L1} = \lambda_{FBG,i-1}$ and the third transmission window gates the joint filter response that overlaps in time after the interaction with the FBG array. The electrical gating parameters τ_{1-3} and τ_{2-3} operate as spectral tuning parameters. They preset the corresponding filter response times $T_{filter1} = \tau_{2-3}$ and $T_{filter2} = \tau_{1-3}$ selecting λ_{L1} and λ_{L2}, respectively. Because τ_{1-3} and τ_{2-3} are adjusted individually, λ_{L1} and λ_{L2} can be tuned independently from each other indicating a unique spectral flexibility of the TCFL. With the constant PRTT for each wavelength $\lambda_{FBG,i}$, the multi-wavelength emission is inherently synchronized. In order to balance the effective spectral gain in the cavity at λ_{L1} and λ_{L2}, the amplitudes A_1, A_2 and A_3 of the optical gating signal can be adjusted electrically to apply individual losses to each wavelength. Even with the dominant homogeneous line broadening in active fibers, this enables matched amplitudes for each wavelength pair over the tuning range.

Following up on the introduced tuning idea, the optical gating scheme shows a unique scalability to even more emission wavelengths. In principle, extending the gating signal to $p + 1$ ($p \in \mathbb{N}$, $p \leq N$) transmission windows could promote the filter response times of p feedback wavelengths $\lambda_{FBG,i}$ of the FBG array for p spectral lasing lines. They feature individually adjustable amplitudes (by the amplitudes of the optical gating signal) and synchronized pulsed emission at the OC. The practical number of emission wavelengths is merely limited by technological challenges, such as gain competition effects in the active fiber.

Summarizing, the theta-ring resonator together with the programmable optical gating scheme provides a unique flexibility to unambiguously operate the system in tunable 1-λ or independently tunable multi-wavelength emission of synchronized pules. Based on the same resonator setup, the different modes are conveniently triggered by electrically changing the optical gating signal. Whereas the timing of the gating windows determines the emission wavelengths, their electrical amplitudes balance the spectral intensity of the corresponding emission line even considering the spectral gain characteristics of the active medium.

As an example. the 2-λ mode is driven by applying three transmission windows with specific delays. They independently select two emission wavelengths λ_{L1} and λ_{L2} that can propagate with low round-trip losses to form a 2-λ laser emission.

In general, the dual-wavelength mode could be also triggered by four transmission windows at the modulator - one pair for each emission wavelength. As a benefit, the adjustable delay between the pairs of optical gates could even enable two tunable laser lines emitted with precisely adjustable time delay giving even more freedom to tailor the emission of the laser. This specific mode, however, is not considered in the experimental study.

4.2.3 Tunable dual-wavelength emission

The experimental study is based on the setups presented in section 3.2 utilizing the modified optical gating scheme with three transmission windows.

4.2.3.1 Proof of concept

The demonstration of the proof of principle is conducted with the non-PM TCFL employing FBG array B as filter. The modified optical gating signal comprising three optical gates with variable timings (τ_{1-3} & τ_{2-3}), normalized amplitudes (A_1, A_2 & A_3), GWs (τ_{GW1}, τ_{GW2} & τ_{GW3}) and the modulation period T_{MP} is remote-controlled by a LabVIEW driven software applying the corresponding optical gating waveform to the AOM. Fig. 4.8 shows two exemplary settings with the generic optical gating signals in the top graph and the corresponding emission spectra in the graph at the bottom. The time scale of the gating signals is referenced to the third gate (A_3) as trigger mark that is supposed to collect the joint filter response at λ_{L1} and λ_{L2} propagating synchronized to OC1 in the lower branch.

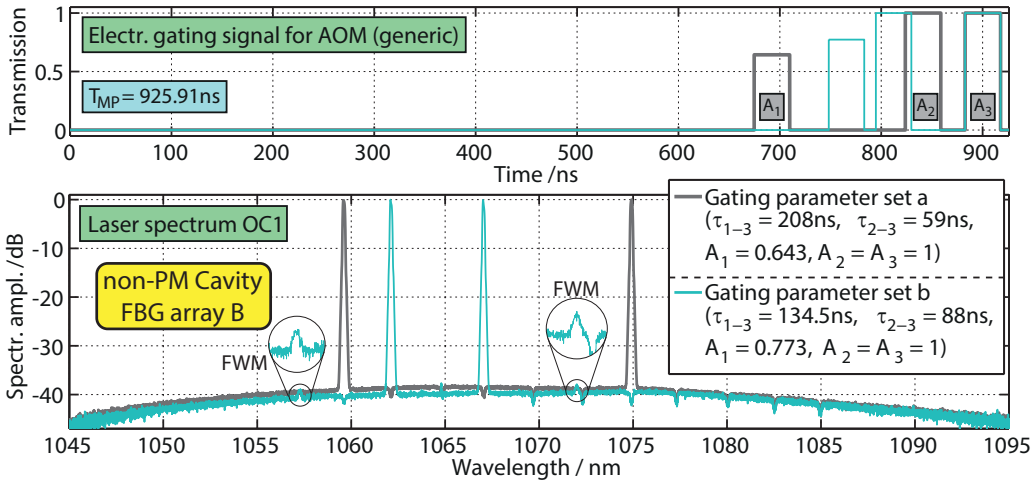

Fig. 4.8: The graph at the top plots two generic optical gating functions applied to the AOM to trigger 2-λ emission. The corresponding emission spectrum at OC1 of the TCFL is illustrated in the graph at the bottom showing two different wavelength pairs emitted at OC1 with balanced amplitudes. Two inset bubbles highlight the mild onset of four-wave mixing (FWM) sidebands at the cyan trace indicating synchronized oscillation of both wavelengths. A scan over multiple wavelength pairs is visualized in a video attached to the multimedia appendix (file name: `Dual-Wavelength-Tuning-over-25nm.mp4`).

The emission spectrum belonging to gating parameter set (a) (gray trace) features two sharp laser lines at $\lambda_{L1} \approx 1059.5\,nm$ and $\lambda_{L2} \approx 1075\,nm$. These wavelengths correspond to FBG 1 matching the filter response time selected by τ_{2-3}, and FBG 7 corresponding to τ_{1-3}. Confirming spectral tunability, a second set (b) of gating parameters triggers another wavelength pair depicted by the cyan trace. Matching to the adjusted τ_{1-3} and τ_{2-3}, the laser operates with the feedback of FBG 2 ($\lambda_{L1} \approx 1062\,nm$) and FBG 4 ($\lambda_{L2} \approx 1067\,nm$). In both measurements, the emission spectra resemble the characteristic properties of 1-λ operation as discussed in section 3.3. This particularly includes an excellent spectral signal contrast (here: $\approx 40\,dB$) and narrow linewidths ($\Delta\lambda_L < 150\,pm$ for each line). Thus, Fig. 4.8 depicts a principle demonstration of 2-λ emission that is tunable by changing the gating parameters.

As highlighted by two inset bubbles in the spectrum, the cyan trace indicates the onset of four-wave mixing (FWM) between λ_{L1} and λ_{L2} creating two weak side band peaks. They arise in a nearly phase-matched regime due to the proximity of both emission wavelengths. Energy conservation ($\Delta\omega = 0$, [15]) determines the wavelengths λ_{SB1} and λ_{SB2} of both side bands. Considering the three photon mixing process at the radial frequencies $\omega_{SB1} = (2 \cdot \omega_{L1} - \omega_{L2})$ and $\omega_{SB2} = (2 \cdot \omega_{L2} - \omega_{L1})$ together with the relation in equation(2.8), the side bands are calculated to

$$\frac{1}{\lambda_{SB1}} = \left(\frac{2}{\lambda_{L1}} - \frac{1}{\lambda_{L2}}\right) \text{ and } \frac{1}{\lambda_{SB2}} = \left(\frac{2}{\lambda_{L2}} - \frac{1}{\lambda_{L1}}\right) . \tag{4.4}$$

In agreement to the measurement in Fig. 4.8, the computed values are $\lambda_{SB1} = 1057.20\,nm$ and $\lambda_{SB2} = 1072.00\,nm$ ($\lambda_{L1} = 1062.09\,nm$ and $\lambda_{L2} = 1067.02\,nm$). The occurrence of this nonlinear $\chi^{(3)}$-effect (see equation(2.3)) already shows evidence for the pulses of both wavelengths (λ_{L1} and λ_{L2}) to oscillate somehow simultaneously in the resonator. This will be further investigated in subsection 4.2.4.

As desired in 2-λ operation, the emission lines in both spectra of Fig. 4.8 feature well balanced spectral amplitudes (absolute difference: $0.16\,dB$ for the parameter set a and $0.06\,dB$ for parameter set b). The precision depends on the fine-tuning efforts in adjusting the gating amplitudes, i.e. A_1 in the given example. For both parameter sets, balanced emission lines are achieved by applying additional losses at gate 1 ($A_1 < 1$). This gate triggers the injection of λ_{L2} into the filter section controlling the larger emission wavelength in both spectra. Looking at the ASE background as indication for the spectral gain, both traces in Fig. 4.8 are supposed to feature slightly stronger gain at λ_{L2}. Thus, this spectral component needs some additional attenuation, e.g. by selective optical gating, for balanced amplitudes between λ_{L1} and λ_{L2}. Whereas gate A_3 concerns both wavelengths equally and gate A_2 only triggers λ_{L1}, gate amplitude A_1 is lowered affecting only λ_{L2}. It is important to highlight that the electrical gating amplitudes A_1 to A_3 do not correspond linearly to the effective optical transmission amplitude due to nonlinear relations between gating voltage, RF signal strength and corresponding AOM transmission. If those values are calibrated beforehand, differences in the effective spectral gain of a laser may be investigated.

4.2.3.2 Balancing the spectral amplitudes

The sensitivity in matching the spectral amplitudes of λ_{L1} and λ_{L2} regarding the gating parameter amplitudes is exemplarily depicted in Fig. 4.9 for another wavelength pair comprising FBG 1 and FBG 4. The graph shows the spectral amplitude of λ_{L1} (dark blue trace) and λ_{L2} (dark green traces) over a fine scan of A_1 from $A_1 = 0.5$ to $A_1 = 1.0$ (maximum). The scan covers the transition zone between 1-λ operation at λ_{L1} (because the selective loss at gate 1 exceeds the laser threshold at λ_{L2}) to 2-λ operation at both emission wavelengths and further on to 1-λ operation at λ_{L2} winning the gain competition against the other emission line without sufficient loss at gate 1. This behavior demonstrates the broadband saturation of the gain curve due to the dominantly homogeneous line broadening in the active fiber. As indicated in the inset zooming into the 2-λ transition zone, the amplitudes of both emission lines are balanced at $A_1 \approx 0.725$. The measurement indicates precise adjustment to be required up to the third digit in A_1 highlighting the demanded accuracy in this parameter. Nevertheless, the transition zone shows a gradual change ranging from $A_1 = 0.66$ to $A_1 = 0.8$ (10 dB levels). The scan of A_1 is visualized in a video in the multimedia appendix (file name: `Dual-Wavelength-scan-balance-Amplitude.mp4`).

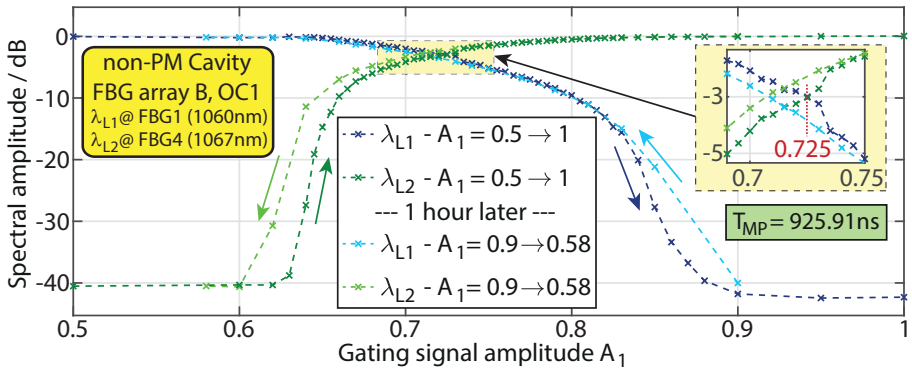

Fig. 4.9: The graph shows the spectral amplitudes of emission wavelength λ_{L1} (FBG 1) and λ_{L2} (FBG 4) depending on the gating signal amplitude A_1 balancing the peaks. Trace one and two are jointly measured with A_1 scanned from 0.5 to 1. The amplitudes of λ_{L1} and λ_{L2} are matched for $A_1 \approx 0.725$. Traces three and four are scanned in the reverse direction after a break of 1 hour showing some hysteresis. The corresponding measurement is visualized in a video following the style in Fig. 4.8 (file name in multimedia appendix: `Dual-Wavelength-scan-balance-Amplitude.mp4`).

The reproducibility of these gating settings is investigated with a second measurement conducted 1 hour later. In contrast to before, A_1 is scanned in the reverse direction starting from 0.9 down to 0.58. It is plotted by the lighter colored traces compared to before, respectively. The scan direction in A_1 is highlighted by arrows with matching colors. The measurement reveals that the spectral amplitudes do not quite match the detailed behavior of before showing a small drift particularly on the light green trace. Balanced emission lines of λ_{L1} and λ_{L2} are achieved at $A_1 \approx 0.705$ (see inset of Fig. 4.9). This shift might arise from environmental influences (the lab is not air-conditioned) impacting, e.g., the effective spectral gain or the RF driver efficiency, or potentially reveal a mild hysteresis regarding the scan direction. In any case, for a fully automated operation of the TCFL in tunable 2-λ emission, the output can be monitored steadily with a feedback loop and an iterative correction of the gating amplitudes to ensure balanced emission of λ_{L1} and λ_{L2}.

4.2.3.3 Optical gating regimes in 2-λ operation

The design criteria for the TCFL as discussed in subsection 3.3.1 for 1-λ operation remain valid in the 2-λ regime. This particularly includes the condition in equation(3.7), prohibiting optical gating with the inverse gating times τ'_{1-2}. Adding up to the aforementioned criteria, the 2-λ regime works with an additional gating window that potentially permits further undesired pulse paths resulting in parasitic emission wavelengths and delayed pulses. Corresponding gating regimes are sketched in Fig. 4.10 based on labeling the function of each transmission window at the modulator. The pulse injection at the corresponding wavelength into the filter section is labeled as 'In' whereas the out coupling of the filter response towards circulator 2 is marked as 'Out'. The respective gating times, determining the emission wavelengths, are noted for each regime.

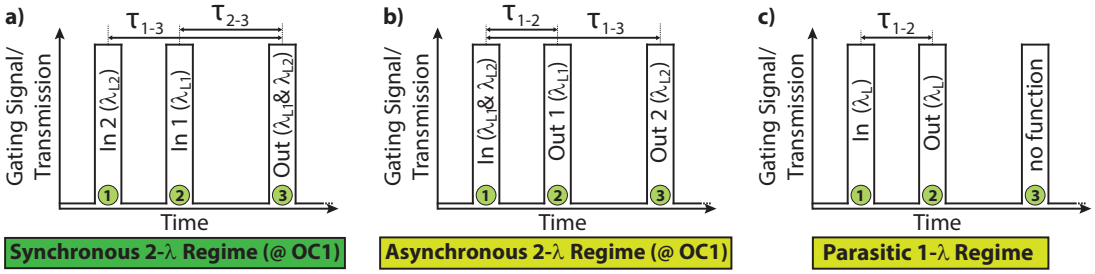

Fig. 4.10: The graphs label main optical gating regimes of the TCFL triggering 2-λ emission. Whereas each graph sketches the same gating signal comprising three gates (see green circles for gate numbering), their respective functionality differs selecting different pulse paths. Their role in the corresponding regime is labeled by 'In' for injecting the pulse of the corresponding wavelength into the filter section and 'Out' for coupling out the filter response to pass the pulse on towards the lower cavity loop.

The experimental study of the TCFL focuses on the synchronous 2-λ regime as desired operation mode enabling simultaneous pulse emission of λ_{L1} and λ_{L2} at OC1. The corresponding gate functionality is sketched in Fig. 4.10a as outlined in subsection 4.2.2. Gate 1 and gate 2 inject ('In') the respective wavelength λ_{L2} and λ_{L1} to the FBG array. The third gate couples out ('Out') the joint response for synchronous 2-λ emission at OC1. The associated gating times τ_{1-3} and τ_{2-3} control both wavelengths. In the asynchronous 2-λ gating regime (b), gate 1 injects both emission wavelengths, propagating synchronized in the upper resonator branch. Gate 2 and gate 3 pick the corresponding response for an asynchronous 2-λ emission at OC1. The pulse of λ_{L2} would be delayed by $(\tau_{1-3} - \tau_{1-2})$ compared to λ_{L1} at OC1. The parasitic 1-λ regime (c) arises from the regime in (b) by not assigning any functionality to gate 3. The laser solely runs over gate 1 and 2. In both unwanted regimes (b and c), one emission wavelength is determined by τ_{1-2} differing from the target spectral lines as adjusted by τ_{1-3} and τ_{2-3}. Gain competition favors the operating regime.

The occurrence of those regimes is shown in Fig. 4.11. The graphs relate measured emission spectra (plot a-c) to the applied gating signals (plot d-f) and the temporal emission traces over one period T_{MP} at OC1 and OC2 (plot g-i). The time scale of plots g-i is referenced to the gating signals (plot d-f) in order to correlate the emitted pulses to their defining gates. Each pulse component is labeled in matching colors with its generating gating time. Working with

the same parameters τ_{1-3} and τ_{2-3}, the gate amplitudes are varied to scan through the different gating regimes depicted by the columns.

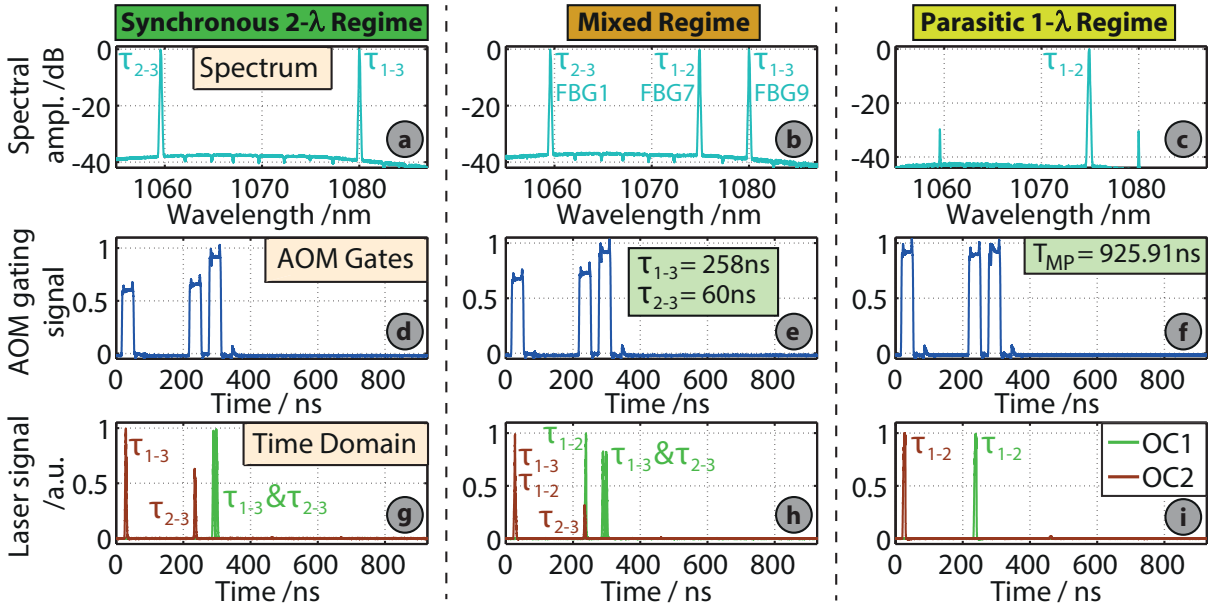

Fig. 4.11: The figure provides an overview over the emission characteristics in the different gating regimes in 2-λ mode. The graphs show the emission spectrum (top row, a-c), the corresponding electrical gating signal applied to the AOM (middle row, d-f) and the temporal emission trace (bottom row, graph g-i) at OC1 (green trace) and OC2 (brown trace) of the non-PM TCFL (FBG array B). The timing of the gates ($\tau_{1-3} = 258\,ns$ and $\tau_{1-3} = 60\,ns$) targets 2-λ emission at FBG 1 and FBG 9. The time scale in graph g-i relates to the timing of the gate in graph d-f. The different columns represent the different gating regimes triggered by varying the transmission amplitudes of gate 1 and 2. Whereas graph a,d and g correspond to the desired synchronous 2-λ regime at OC1, graphs c,f and i show the parasitic 1-λ regime emitting at FBG 7. Graph b,e and f represent an intermediate mixed regime.

The left column (plot a,d,g) corresponds to the synchronous 2-λ regime. The emission wavelengths are determined by τ_{1-3} and τ_{2-3} locking λ_{L2} and λ_{L1} to FBG 9 (1080 nm) and FBG 1 (1060 nm). In the time domain (g), the emission features a single pulse for both wavelengths emitted at OC1 (green trace), relating to the position of gate 3, and delayed spectral pulse components at OC2 (brown trace) in the upper cavity branch. The delay results from the distributed filter feedback matching the separation between gate 1 and gate 2. The central column (plot b,e,h) shows a mix of the synchronous and asynchronous 2-λ regime (Fig. 4.10 a and b) occurring at a time. As labeled in graph b), the spectrum shows three balanced emission lines with each gate timing determining one emission wavelength. FBG 7 (1075 nm) arises as parasitic peak triggered via τ_{1-2}. In the time domain (plot h), this results in an additional pulse at OC1 delayed to the initial pulse matching the position of gate 2 (exiting gate for this wavelength). In the upper cavity branch (OC2), this new wavelength component occurs synchronized with λ_{L2} triggered by τ_{1-3}. Here, the pulse connected to τ_{2-3} (FBG 1) occurs delayed by the gate separation (second brown peak). Accordingly, whereas in the lower branch, FBG 1 (triggered by τ_{2-3}) and FBG 9 (triggered by τ_{1-3}) operate synchronized, in the upper branch, it is FBG 7 (triggered by τ_{1-2}) and FBG 9.

The right column of Fig. 4.11 shows the parasitic 1-λ regime with solely τ_{1-2} defining the emission wavelength of the laser (FBG 7). The other two spectral lines occur strongly suppressed

($-30\,dB$ level). The temporal traces in plot i, showing a single pulse at each OC port, confirm that gate 3 has no functionality in this regime (compare to Fig. 4.10c).

Because the ambiguity in the optical gating signal (see Fig. 4.10) may prohibit to exploit the full tuning bandwidth in the 2-λ regime, two solutions are implemented to enforce synchronous 2-λ emission at OC1:

1. The resonator design can be adapted in the middle branch of the TCFL. For the target gating times τ_{1-3} and τ_{2-3}, the layout is required to ensure no suitable filter response time at τ_{1-2}. For an equidistant grating spacing Δz throughout the discrete filter, this would be ensured by satisfying the condition

$$z_0 = \left(j - \frac{1}{2}\right) \cdot \Delta z \ (j \in \mathbb{N}) \tag{4.5}$$

   with z_0 depicting the distance between modulator and the beginning of the filter section (equivalent to the time $\tau_{1-2,min}$). In this case, τ_{1-3} aiming for the time of flight of grating p is generally determined by $\tau_{1-3} \propto \left[\left(j - \frac{1}{2}\right) \cdot \Delta z + (p-1) \cdot \Delta z\right]$ and τ_{2-3} targeting grating q with $\tau_{2-3} \propto \left[\left(j - \frac{1}{2}\right) \cdot \Delta z + (q-1) \cdot \Delta z\right]$ $(p, q \in \mathbb{N},\, p > q)$. Accordingly, FBG response times with respect to the modulator are proportional to half-integer multiples of the FBG separation Δz. Calculating $\tau_{1-2} = \tau_{1-3} - \tau_{2-3}$ as the parasitic gating time, it results to $\tau_{2-3} \propto (p-q)\Delta z$, i.e. a multiple integer of the Δz. Hence, for each tuning pair of τ_{1-3} & τ_{2-3}, τ_{1-2} does not correspond to a time of flight in the filter section, prohibiting any wavelength to be triggered by this parameter. Thus, both parasitic regimes in Fig. 4.10b) and c) are suppressed. In the experimental study, z_0 was adjusted to the criterion in equation(4.5) by adding a short piece of fiber labeled as delay fiber 2 in Fig. 3.3. However, due to the finite rise times of the modulator, this criterion requires the delay between neighboring FBGs (equivalent to Δz) to be sufficiently larger than to the rise time t_R of the modulator to achieve full discrimination. This was not the case in the experimental study. Thus, a second solution was additionally applied.

2. As pictured in Fig. 4.10, both undesired regimes (b and c) trigger the parasitic wavelength component with gate 1 and gate 2 (i.e. τ_{1-2}). To suppress this component, additional losses may be symmetrically applied to these gates. Accordingly, signals triggering with τ_{1-2} suffer on twice the loss than the desired signals in the synchronous 2-λ regime that exit the filter section at gate 3, which is still at maximum transmission. Hence, the selective losses at gate 1 and gate 2 add additional discrimination between the gating regimes.

The strategy of point 2 has also been utilized to scan through the different gating regimes as mentioned in Fig. 4.11. For this example, the transition between parasitic 1-λ operation (λ_L at FBG 7 - $1075\,nm$) to synchronous 2-λ emission at OC1 (λ_{L1} at FBG 1 - $1060\,nm$, λ_{L2} at FBG 9 - $1080\,nm$) is investigated more extensively in Fig. 4.12.

Graph a) shows an exemplary gating signal with losses applied to gate 1 and gate 2, as well as the respective emission spectrum comprising all three spectral lines. The spectral amplitudes are controlled by adapting A_1 and A_2. While their ratio (A_1:A_2) balances the spectral

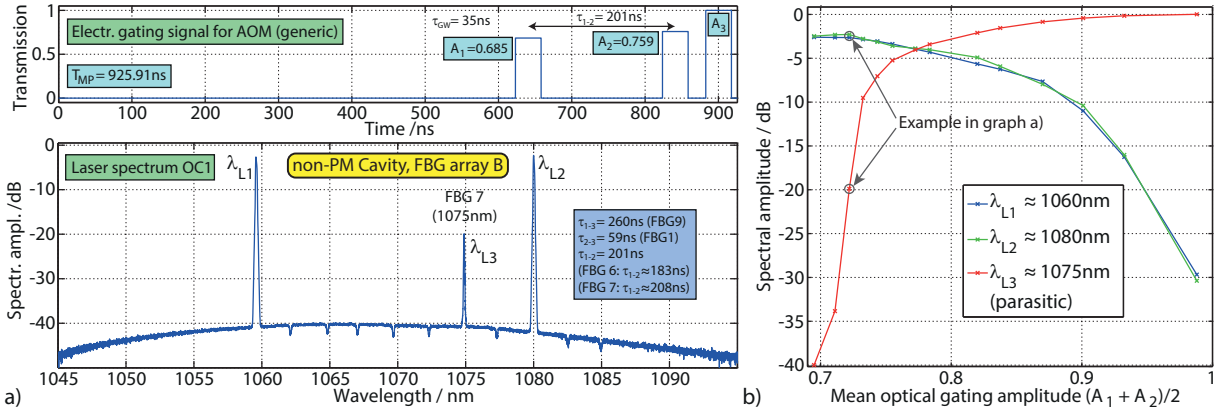

Fig. 4.12: Graph a) shows a generic electrical gating signal (graph at the top) triggering dual-wavelength emission at FBG 1 and FBG 9 as well as a parasitic emission line rising at the position of FBG 7 as pictured in the spectrum at the bottom. Graph b) plots the behavior of the corresponding spectral amplitudes depending on the mean gating amplitude of A_1 and A_2, highlighting the transition to the parasitic 1-λ regime. The transition is also visualized in a video in the multimedia appendix (file name: `Dual-Wavelength-Regimes-Transition.mp4`).

amplitudes at λ_{L1} and λ_{L2}, their absolute values quantified by the mean optical gating amplitude $\frac{A_1+A_2}{2}$ discriminate the gating regimes. Thus, by modifying A_1 and A_2 symmetrically (A_1:$A_2 \approx$ constant), the suppression of the parasitic 1-λ emission is controlled. This is pictured in graph b) plotting the spectral amplitudes of the three emission lines for changing mean gating amplitudes (A_1:A_2 is somehow maintained). This parameter scan is also highlighted in a video in the multimedia appendix plotting the spectra along the transition (file name: `Dual-Wavelength-Regimes-Transition.mp4`). Fig. 4.12b proves the 1-λ regime (λ_{L3}) to be dominant in case of minor losses at A_1 and A_2 ($\frac{A_1+A_2}{2}$ approaching 1). Increasing the losses symmetrically at both gates ($\frac{A_1+A_2}{2}$ is decreasing), the amplitudes at the target emission wavelengths λ_{L1} and λ_{L2} rise up while λ_{L3} reduces. The gradual transition reaches synchronous 2-λ operation at OC1 for mean optical gating amplitudes < 0.7 without another parasitic emission line. The increased losses at the modulator have negligible impact on the spectral amplitudes dropping by about $3\,dB$ due to two emission wavelengths. Thus, the discrimination of the optical gating regimes is verified for a modified gating signal with symmetric losses at gate 1 and gate 2.

4.2.3.4 Realized tuning functionality

By applying both discussed strategies to enforce synchronous 2-λ operation at OC1, the full potential in the tuning bandwidth of the implemented FBG array has been exploited. This is demonstrated in Fig. 4.13 by two tuning spectrograms showing a scan through the different wavelength pairs of the non-PM TCFL with FBG array B (graph a) and the PM TCFL with FBG array C (graph b). Due to multidimensional tuning parameters to control the wavelengths λ_{L1} and λ_{L2} (via τ_{1-3} & τ_{2-3}) and their respective amplitudes (via A_1 & A_2), the x-axis depicts numbered sets of applied gating parameters. Following the style of Fig. 4.8, both scans through the tuning range are also animated in videos attached to the multimedia appendix (file names: `Dual-Wavelength-Tuning-over-25nm.mp4` & `Dual-Wavelength-Tuning-over-50nm-linear.avi`).

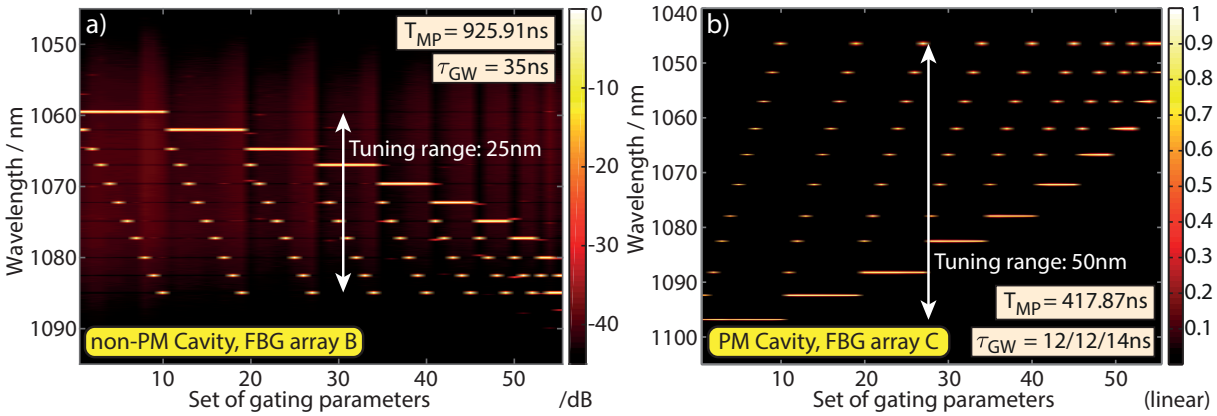

Fig. 4.13: The graphs show the dual-wavelength tuning spectrograms scanning 2-λ emission for the non-PM TCFL with FBG array B (graph a) and the PM TCFL with FBG array C (graph b). For each wavelength pair, a tailored set of gating parameters (τ_{1-3}, τ_{2-3}, A_1, A_2 and A_3) is applied. A maximum tuning range of 50 nm is achieved [142].

In both graphs in Fig. 4.13, the wavelength pairs are scanned gradually starting from λ_{L1} being operated at FBG 1 and λ_{L2} is scanned from FBG 2 to FBG 11. Then, λ_{L1} is successively locked to increasing grating numbers and λ_{L2} steps through the residual FBGs, respectively, to cover the full tuning range. The theoretical number of 2-λ combinations in λ_{L1} & λ_{L2} is computed by a binomial coefficient. In principle, for K simultaneous emission wavelengths of the laser operated over an ensemble of N discrete filter wavelengths $\lambda_{FBG,i}$, the number of potential combinations C of emission wavelengths is defined by

$$C = \binom{N}{K} . \tag{4.6}$$

Accordingly, with an FBG array of $N = 11$ gratings (FBG array B and FBG array C), $C = 55$ wavelength pairs can be addressed. Notably, with a minor increase of response wavelengths in the filter layout (N), the number of 2-λ combinations can be scaled significantly. With a non-equidistant spectral spacing in the FBG array, this becomes powerful when applying, e.g., difference frequency generation as an application, tuning through C different beat frequencies in a new spectral domain, e.g. THz range.

In both tuning spectrograms of Fig. 4.13, all 55 dual-wavelength combinations are successfully demonstrated, covering the full tuning range of 25 nm (non-PM TCFL in graph a) and 50 nm (PM TCFL in graph b). By addressing each wavelength pair offered by the discrete filter design, the tuning concept uniquely features an independent tunability of both, λ_{L1} and λ_{L2}, based on the programmable optical gating scheme. The number and tuning bandwidth of the wavelength pairs is limited by the employed FBG array. Due to the efficient spectral filtering of the tuning concept, the experiment confirms 2-λ operation with high ASE contrast and narrow linewidths over the full tuning range as discussed before. The corresponding output powers are matching the levels presented for 1-λ operation (subsection 3.3.2).

4.2.3.5 Pulse properties

As noted for tunable 1-λ operation in the TCFL (see discussion of Fig. 3.7), each response wavelength of the FBG array features an extended operation window in its triggering gating time (τ_{1-2}). This phenomenon has also been observed in 2-λ operation. Steady emission wavelengths in λ_{L1} and λ_{L2} with balanced amplitudes are achieved along decent operation windows in τ_{1-3} and τ_{2-3}, tolerating modification of a few nanoseconds with negligible impact on the emission spectra. However, this ambiguity in the gating times correlates with substantial variations in the temporal pulse shapes. This is depicted in Fig. 4.14.

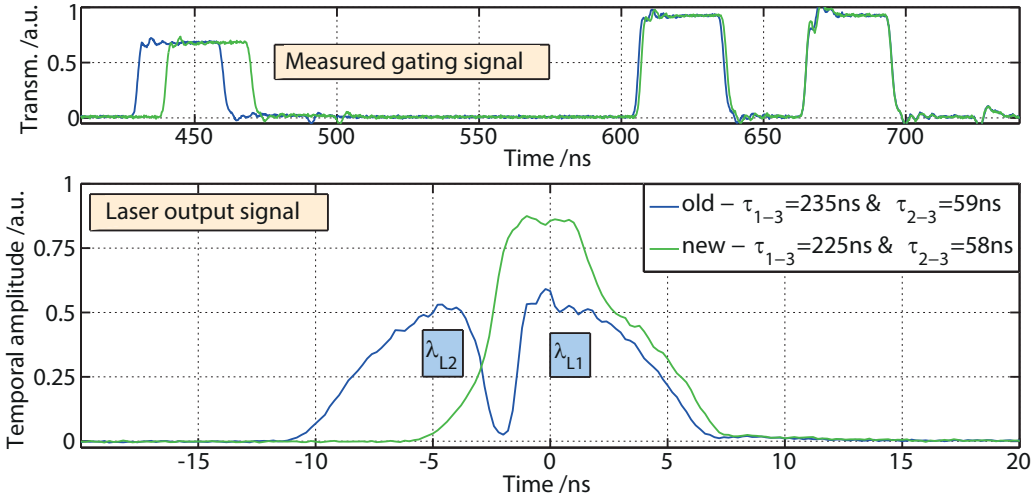

Fig. 4.14: The graph at the bottom shows the emitted pulse shape of the TCFL for two sets of gating parameters resulting in the same 2-λ emission spectrum (not in picture). The top graph illustrates the corresponding optical gating functions. Whereas the initial set of gating parameters generates a split-up pulse (blue trace) linked to the respective emission wavelength, the green trace represents a modified set of gating parameters resulting in a united pulse envelope for both wavelengths λ_{L1} and λ_{L2}.

The top graph shows two gating traces featuring different timings τ_{1-3} (tuned by $10\,ns$) and τ_{2-3} (tuned by $1\,ns$). Both signals result in essentially the same 2-λ emission spectra. However, as plotted in the graph at the bottom, the emitted pulse shapes show significant variations. The initial gating setting (blue traces) caused the pulse to have two split-up sub-pulses potentially belonging to the two respective emission wavelengths λ_{L1} and λ_{L2}. In contrast, the second gating setting (green traces) ensured a somehow uniform pulse shape. Detailed conclusions about the distribution of λ_{L1} and λ_{L2} within the pulse cannot be drawn from plain spectral or temporal measurements with an OSA or an OSCI. Hence, more elaborate analysis techniques are required.

4.2.4 Analysis of pulse synchronicity

For applications relying on the direct interaction of both tunable emission wavelengths (e.g. in nonlinear frequency mixing), the corresponding pulse components are crucially required to show proper overlap, i.e. a simultaneous emission. While the TCFL in the chosen 2-λ gating regime inherently features synchronized spectral output at OC1, the observed behavior in Fig. 4.14 reveals some dynamics in the pulse shapes depending on the precise gating settings. These characteristics need to be correlated with the temporal distribution of both emission wavelengths.

A joint investigation of the spectral and temporal dynamics is required to link both domains and optimize the gating settings enabling maximized pulse overlap between λ_{L1} and λ_{L2}.

Following that purpose, a modified time-delay spectrometer (TDS) is developed and applied to characterize the non-PM TCFL in 2-λ operation. With this tool, pulse spectrograms can be retrieved providing the foundation to investigate and optimize spectral pulse dynamics. Additionally, while an OSA records averaged emission spectra by scanning the frequency domain, the TDS enables the measurement of a single pulse spectrum. Thus, steady laser oscillations can be verified for both wavelengths λ_{L1} and λ_{L2} confirming a truly 2-λ operation in each round trip.

4.2.4.1 Time-delay spectrometer (TDS)

A TDS facilitates the simultaneous spectral and temporal characterization of pulsed light sources based on a plain temporal measurement with an OSCI followed by a numerical analysis to retrieve a pulse spectrogram. The concept of the TDS is presented in detail in reference [145].

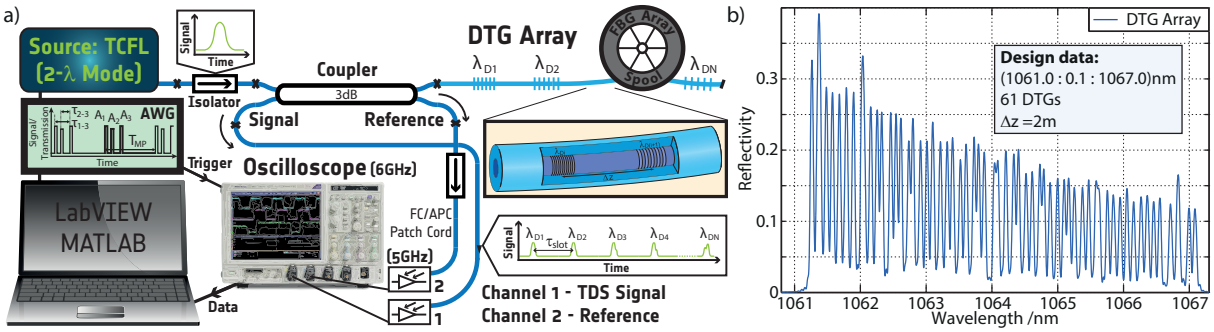

Fig. 4.15: The setup of the fiber-integrated Time-Delay spectrometer (TDS) is depicted in part a). The output signal of the TCFL working in 2-λ mode is spliced to the TDS. The measurement is triggered by the AWG working as master clock of the TCFL. Data acquisition is remote-controlled via a LabVIEW program and the recorded traces are post-processed with a `MATLAB` program reconstructing the pulse spectrogram. A DTG array with 61 DTGs covering a spectral range of 6 nm with a resolution of 100 pm is employed as spectral probe. The corresponding reflectivity spectrum is depicted in graph b).

Fig. 4.15a) shows the experimental setup of the developed fiber-integrated TDS utilized for analyzing tunable 2-λ operation. The signal of the TCFL is divided by a 3dB coupler to a reference arm and a spectral probe arm. The reference arm facilitates the measurement of the initial pulse shape based on a photodiode (bandwidth: $5\,GHz$) connected to an OSCI (`Tektronix DPO70604`, bandwidth: $6\,GHz$). On the other side, a draw tower grating (DTG) array operates as spectral probe on the incoming laser pulses. It incorporates N FBGs featuring a fine spectral sampling in the feedback wavelengths λ_{Di} and a respective spatial separation Δz. Similar to diffraction gratings in industrial spectrometers encrypting the spectrum in a spatially dependent signal, the distributed feedback of the DTG array translates the spectral content to a characteristic time-dependent trace. Each grating in the DTG array slices out a particular spectral component λ_{Di} of the injected pulse reflecting it with its characteristic temporal behavior towards the signal arm. Due to the spatial separation Δz between adjacent gratings, the spectral components are returned with a corresponding delay τ_{slot} (see inset along the signal arm sketching an exemplary trace). This enables unraveling the spectral content as well as the temporal dynamics of each component λ_{Di} in the initial pulse. The temporal trace is

recorded with the OSCI triggered by the AWG as master clock driving the TCFL. This concept enables the analysis of single laser pulses. While a LabVIEW program is developed to control the measurement, post-processing data is done based on a `MATLAB` program.

The spectral probe is an FBG array inscribed inline with the fiber drawing process. This DTG array comprises $N = 61$ gratings. For a maximized spectral resolution of the spectral probe, it is designed with a minimum spectral spacing of $100\,pm$ between adjacent FBGs limited by the resolution of the inscription technology and the linewidth of a grating ($\Delta\lambda_{FBG} \approx 50\,pm$). The corresponding feedback bandwidth is $6\,nm$ restricting the measurement range of the TDS from about $1061\,nm$ to $1067\,nm$. The measured reflectivity spectrum is depicted in Fig. 4.15b. Due to three spectrally overlapping feedback lines, it features only 58 separated response peaks. They exhibit a reflectivity of about 30%. This value drops towards longer wavelengths caused by the propagation losses through the filter structure. This measurement is used to calibrate the spectral filter response allocating the feedback wavelength and corresponding effective reflectivity of each grating, i.e. the spectral probe channels. The equidistant spatial separation of the gratings is $2\,m$ setting the delay between adjacent spectral components in the response signal. Prior to the application of the TDS to the TCFL, the temporal response of this DTG array has been characterized with a pulsed broadband laser diode. Based on the continuity between the spectral channels of the TDS, the characteristic delay between adjacent gratings, resulting from Δz, is determined to $\tau_{slot} = 19.62\,ns$.

4.2.4.2 Measurement constraints of the TDS

The TDS does not fulfill the demands of a universal high-resolution spectrometer. However, the measurement concept of the TDS is specialized to characterize dynamics of pulsed light sources within strict parameter limitations in the spectral and temporal domain.

Most importantly, the emission spectrum of the light source must be within the restricted measurement range of the spectral probe. To adapt the non-PM TCFL for the investigation with the TDS employing the discussed DTG array, a special FBG array is inscribed exclusively for this study of 2-λ operation. For having a selection of three different 2-λ pairs, FBG array D comprises three gratings within the measurement range of the TDS while still showing no spectral overlap with each other (compare to discussion in subsection 3.3.1). This is pictured in Fig. 4.16 showing the emission spectrum of the TCFL locked to the first grating of FBG array D (1-λ operation). While the peak wavelength is $\lambda_L = 1064.43\,nm$, two small drops in the ASE background reveal the spectral location of the other gratings. In order to relate them to the response spectrum of the DTG array, the calibrated feedback wavelengths of the spectral probe are plotted by the green trace versus the corresponding grating number. The trace proves that the DTG array covers all three emission lines provided by FBG array D. Based on the good spectral overlap, DTG 14 with a feedback wavelength in the proximity of λ_L (TCFL locked to FBG 1) is utilized to calibrate the temporal measurement scale of the TDS later on.

Another important criterion on the light source under investigation is the linewidth that needs to be at least as broad as the sampling resolution provided by the spectral probe of the TDS. With a lasing linewidth of $\Delta\lambda_L \approx 150\,pm$, the sampling of the DTG array ensures at least one

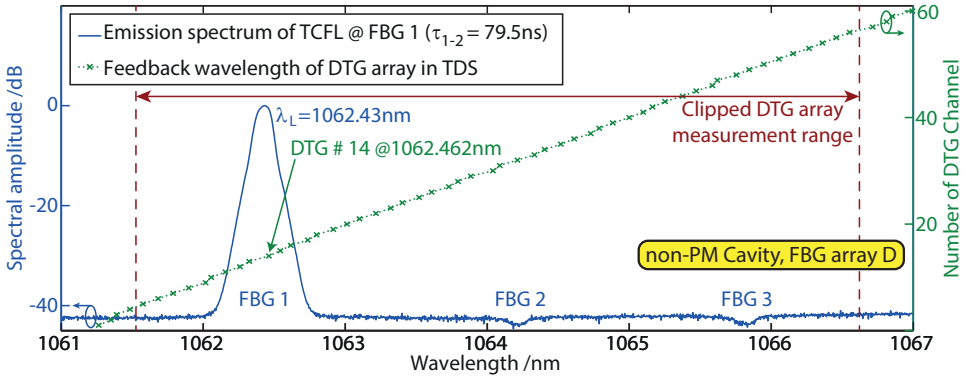

Fig. 4.16: The graph depicts the emission spectrum (blue trace) of the TCFL operated at grating 1 of FBG array D, i.e. $\lambda_L = 1064.43\,nm$. Small dips in the ASE background level reveal the spectral location of FBG 2 and FBG 3 of FBG array D. The green trace relates the characterized feedback wavelengths of the DTG array as spectral probe of the TDS to the corresponding grating number in the filter, i.e. its position and specific delay.

probe grating per emission line as also proven in Fig. 4.16. Thus, sampling issues with emission lines potentially just transmitting through the spectral probe are avoided.

Based on the length of the DTG array incorporating delay lines for $N = 61$ spectral components, a minimum repetition rate of the pulse light source is required to avoid ghost signals within the measurement trace. In order to ensure the interaction of a single pulse at a time in the spectral probe, the separation of succeeding pulses (set by the repetition rate) needs to be larger than the maximum delay acquired between DTG 1 and DTG N. For the employed DTG array, this delay results to $N \cdot \tau_{slot} = 61 \cdot 19.62\,ns = 1196.82\,ns$. The TCFL operating with FBG array D works with a modulation period of about $T_{MP} \approx 963\,ns$ and thus does not fulfill this criterion. While the laser resonator could be simply enlarged by additional delay fiber to match the requirement, the measured tuning bandwidth of the TCFL, which does not cover the full feedback bandwidth of the DTG array, provides another solution. Due to the spectral purity with an excellent signal contrast of the TCFL and clean operation restricted to the feedback wavelengths of FBG array D, many gratings of the DTG array show no overlap with the laser emission. Without any impact on the TDS signal, the spectral range of the DTG array can be virtually clipped by numerically excluding the feedback of the outer DTGs from the analysis. This is illustrated by the red dashed lines in Fig. 4.16 restricting the DTG channels of the green trace. With only 52 gratings considered for data evaluation, ghost artifacts from succeeding pulses of the source under investigation are avoided.

Another constraint in the time domain results from the spatial separation between adjacent DTGs ($\Delta z = 2\,m$). To clearly discriminate the temporal response from adjacent spectral measurement channels of the spectral probe, the full pulse duration must be shorter than the temporal delay τ_{slot}. Comparing the characteristic delay between the measurement channels $\tau_{slot} = 19.62\,ns$ of the DTG array to, e.g., the pulses measured in Fig. 4.14, the blue trace with separated spectral pulse components (worst case scenario) measures about $18\,ns$ and satisfies this condition. Based on the measurement concepts, CW background signals are disregarded anyways. On the other side, the pulse shape must be still resolvable by the oscilloscope to draw conclusions about the temporal behavior. With the employed $6\,GHz$ OSCI and $5\,GHz$ photo diode (see Fig. 4.15a), pulse dynamic down to a few hundred picoseconds can be resolved.

Conducting all the investigations regarding pulse synchronicity with the non-PM TCFL and the tailored FBG array D, the laser system fits to the measurement constraints of the TDS employing the discussed DTG array.

4.2.4.3 Data evaluation

The analysis with the TDS requires some steps of post-processing to retrieve a pulse spectrogram from the plain temporal trace. This procedure is briefly outlined in the following.

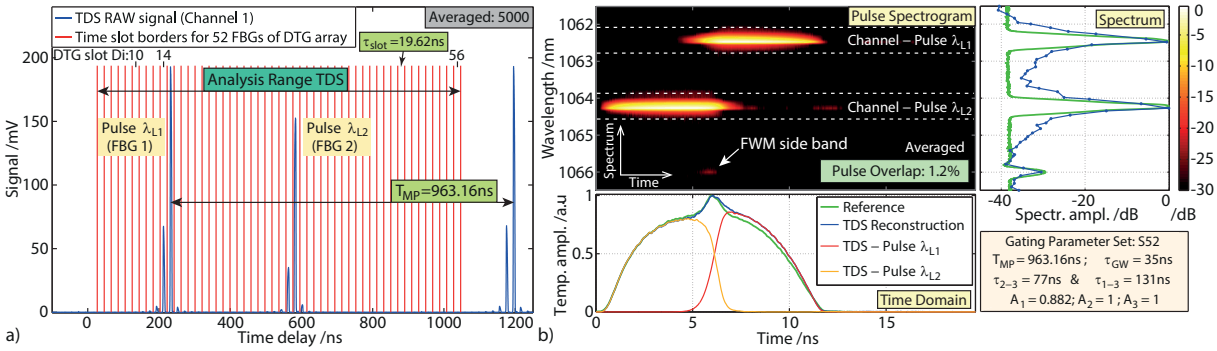

Fig. 4.17: Graph a) shows the averaged TDS raw signal measured for an exemplary setting of the TCFL operating in 2-λ mode at FBG 1 and FBG 2. The virtual slot borders for each evaluated DTG channel (slot duration calibrated to $\tau_{slot} = 19.62ns$ correlating to $\Delta z = 2\,m$) are included by red lines highlighting the TDS measurement range. Based on post-processing the TDS raw trace, part b) shows the reconstructed pulse spectrogram relating the spectral and temporal pulse properties. The graph at the bottom and on the right-hand side represent the extracted pulse shape and spectrum, respectively. Additionally, both graphs comprise the corresponding reference signals to verify the measurement.

Fig. 4.17 highlights an exemplary TDS measurement of 2-λ emission at FBG 1 and FBG 2. Graph a) shows the recorded TDS signal (blue trace, channel 1 at OSCI, averaged over 5000 pulses). The trace shows three zones of pulse bursts. While the first two zones (at a time delay of around $200\,ns$ and $600\,ns$) arise from the spectral components of λ_{L1} (determined by FBG 1) and λ_{L2} (determined by FBG 2), respectively, the third zone (at a time delay of around $1200\,ns$) is a duplicate of the first one originating from the succeeding pulse delayed by T_{MP}. Hence, the analysis focuses on the first two pulse bursts. After an offset correction and an interpolation for an enhanced temporal sampling density, the first step is to correlate the time delay to the corresponding DTG measurement channel Di. As noted for Fig. 4.16, the reference is set to DTG 14. The red lines in Fig. 4.17a highlight the calibrated response windows (channel duration τ_{slot}) for each probe grating capturing the behavior of the corresponding spectral component λ_{Di}. The signal in each channel is corrected by the effective DTG reflectivity as measured in Fig. 4.15b and assigned to the respective λ_{Di}. The data of all the measurement channels are rearranged in a matrix and normalized in logarithmic scale. The resulting pulse spectrogram is pictured by a smoothed intensity plot in Fig. 4.17b. The y-axis highlights the spectral domain (based on the ensemble of λ_{Di}) whereas the x-axis corresponds to the time domain covering the duration of τ_{slot}. The pulse spectrogram unveils the two spectral emission lines at $\lambda_{L1} \approx 1062.4\,nm$ and $\lambda_{L2} \approx 1064.2\,nm$ to occur with a delay of a few nanoseconds to each other.

To validate the measurement, the isolated spectral and temporal emission properties of the measured pulse can be extracted from the TDS signal, respectively. For the spectrum, each

measurement channel in the pulse spectrogram is integrated along the lines giving its overall spectral amplitude. The graph on the right side of Fig. 4.17b features the retrieved spectrum (blue trace) as well as the reference spectrum measured with an OSA. Considering the worse dynamic range and resolution of the TDS measurement, the traces resemble each other very well. The two emission lines at λ_{L1} and λ_{L2} match each other in amplitude and position. Furthermore, even a side band at around $1066\,nm$ is measured arising from FWM from the main emission lines. Confirming its origin, the pulse spectrogram shows the FWM side band as dark red peak in the overlapping zone of both wavelengths.

The reference in the time domain is retrieved by integrating along the columns of the pulse spectrogram. The reconstructed trace is plotted in the graph at the bottom (blue trace) and compared to the normalized reference trace measured with channel 2 of the TDS. The two signals almost match each other featuring the same pulse duration as well as the characteristic features, such as the small peak in the center. In order to analyze the temporal behavior of each emission line selectively, the time domain may also be integrated just along the respective channel of λ_{L1} and λ_{L2} as marked by the white dashed lines in the pulse spectrogram. The resulting pulse shapes are plotted in the graph at the bottom as red and orange traces highlighting the weak temporal overlap between both lines in this particular example.

Based on the superb agreement of the TDS measurement with the reference traces in time and spectral domain, the measurement concept and the outlined evaluation procedure is verified. The retrieved pulse spectrogram provides new insights into the temporal behavior of both emission lines λ_{L1} and λ_{L2}. Whereas the plain temporal measurement with an OSCI only records the green reference trace showing a uniform and symmetric pulse with a small disturbing peak in the center, only the analysis with the TDS reveals that both wavelengths are delayed to each other. The peak in the center of the overall pulse shape arises from the small overlap zone between both wavelengths. In order to quantify the overlap for further analyses, a normalized overlap factor is computed integrating over the extracted pulse shapes of λ_{L1} ($\mathrm{Pulse}_{L1}(t)$, red trace) and λ_{L2} ($\mathrm{Pulse}_{L2}(t)$, orange trace). It is defined as

$$\text{Pulse Overlapp} = \frac{\left(\int_0^{\tau_{slot}} \mathrm{Pulse}_{L1}(t) \cdot \mathrm{Pulse}_{L2}(t) dt\right)^2}{\int_0^{\tau_{slot}} (\mathrm{Pulse}_{L1}(t))^2 dt \cdot \int_0^{\tau_{slot}} (\mathrm{Pulse}_{L2}(t))^2 dt} \,. \tag{4.7}$$

For the chosen example in Fig. 4.17, the factor measures 1.2 %, proving the weak overlap.

4.2.4.4 Measurement and optimization of pulse synchronicity

Now, the introduced TDS is applied to the optimization of the 2-λ TCFL output properties. By modifying τ_{1-3} and τ_{2-3} within the operation range of the corresponding target wavelengths λ_{L1} and λ_{L2}, the difference $[\tau_{1-3} - \tau_{2-3}]$ is varied correlating experimentally with the relative pulse positions of both wavelengths. This approach is investigated to shift the pulses of λ_{L1} and λ_{L2} aiming for a maximized overlap. For 2-λ operation locked again to FBG 1 and FBG 2, the relative difference $[\tau_{1-3} - \tau_{2-3}]$ is bidirectionally scanned in steps of $1\,ns$ to investigate

the impact on the spectral distribution of the both wavelengths within the pulse. While the full scan from 38 ns to 61 ns is attached to the multimedia appendix by a video (file name: `Dual-Wavelength-scannedDelay.mp4`), Fig. 4.18 pictures two intermediate steps in the zone of maximized overlap. For each setting in τ_{1-3} and τ_{2-3} throughout the scan, the gating amplitude A_1 is fine-tuned to ensure balanced spectral amplitudes at λ_{L1} and λ_{L2}.

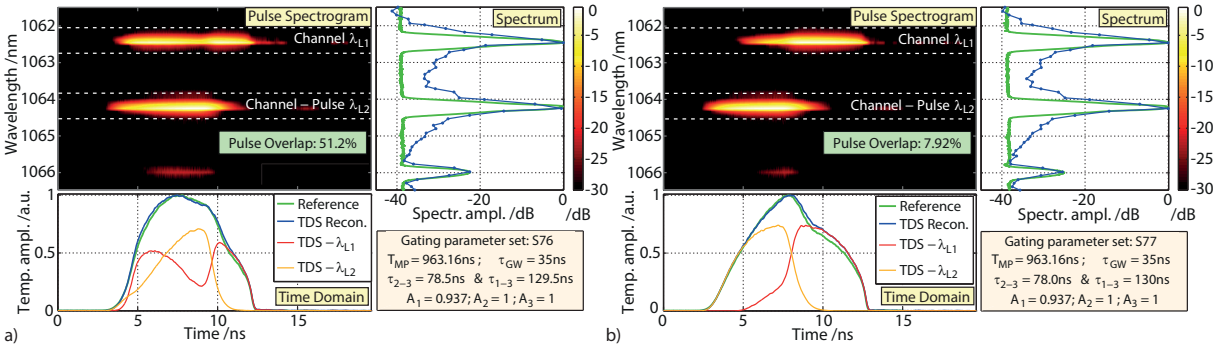

Fig. 4.18: The graphs show two measured pulse spectrograms (averaged acquisition) for the wavelength pair of FBG 1 & FBG 2 (non-PM TCFL, FBG array D). The measurements of part a) and part b) refer to two scan steps in the respective pulse delay, investigating their temporal overlap for different gating settings. The whole scan is visualized in a video attached to the multimedia appendix (file name: `Dual-Wavelength-scannedDelay.mp4`).

Graph a) is recorded for a relative delay $\tau_{1-3} - \tau_{2-3} = 51\,ns$ and represents the best pulse overlap factor achieved in this scan measuring 51%. This is confirmed by the significant FWM side band at 1066 nm observed in the pulse spectrogram as well as the extracted spectrum. While the enhanced pulse overlap is a significant improvement to the setting in Fig. 4.17b, the respective pulse shapes of λ_{L1} (red trace) and λ_{L2} (orange trace) reveal some disturbing dynamics still degrading the pulse overlap. When the TCFL is run with the same gating times, but in 1-λ mode on either of the two wavelengths (adjusted by setting either A_1 or A_2 to zero), the pulse positions overlap in time. When activating 2-λ operation (A_1 and A_2 are adapted), the behavior in Fig. 4.18a is observed showing the pulse of λ_{L1} (red trace) to be split up in two parts when the pulse at λ_{L2} peaks. Those pulse dynamics might be driven by sophisticated gain competition effects between both spectral components. This behavior was also confirmed for single-pulse acquisition of the TDS without any averaging. For applications relying on nonlinear interactions, such as nonlinear frequency mixing, the efficiency would be significantly degraded by such a behavior since the pulse amplitudes of both wavelengths are clearly mismatched in time.

In the zone of $[\tau_{1-3} - \tau_{2-3}]$ enabling proper pulse overlap, minor changes in the gating parameters may have strong impact as shown in Fig. 4.18b for the next scan step at $\tau_{1-3} - \tau_{2-3} = 52\,ns$. The overlap drops to about 8% and the split-up pulse at λ_{L1} from graph a) transferred to a single pulse with a slowly rising edge in graph b). The FWM side band as indirect indicator for the pulse overlap dropped by about 3 dB.

Fig. 4.19a presents the computed pulse overlap (logarithmic scale) along the mentioned scan of the delay between the gating times $[\tau_{1-3} - \tau_{2-3}]$. It shows a monotonic increase towards the presented maximum (see Fig. 4.18a) followed by a steady decay. The asymmetric shape and the varying slopes may be connected to the observed pulse dynamics in the overlapping zone.

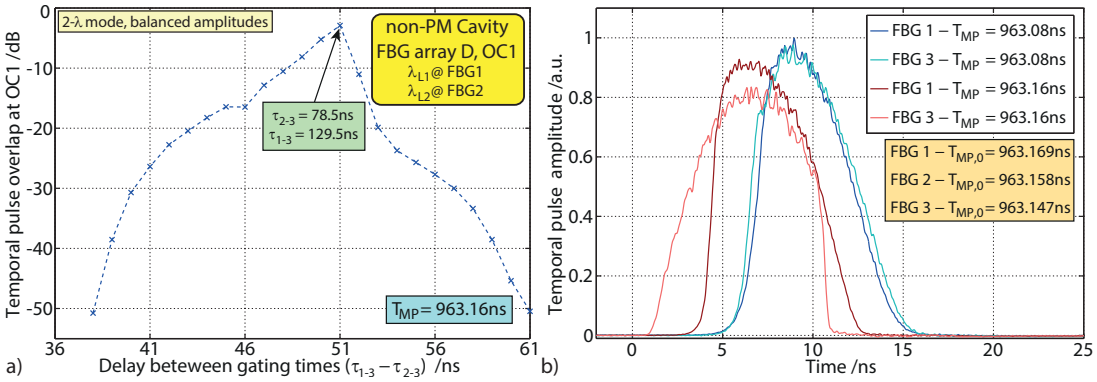

Fig. 4.19: Graph a) depicts the evaluation of the pulse overlap in 2-λ mode at FBG 1 and FBG 2 depending on the relative delay between the gating times. The point of maximum overlap corresponds to the measurement in Fig. 4.18a. Graph b) depicts pulse shapes in 1-λ emission of the TCFL at FBG 1 and FBG 3 depending on T_{MP}. The traces at $T_{MP} = 963.08$ corresponds to the regime of asymmetric pulses showing matched pulse shapes over the tuning range.

The peak maximum is well defined indicating an ideal overlap within $\tau_{1-3} - \tau_{2-3} = (51 \pm 1)ns$. However, even with a finer sampled scan range in $[\tau_{1-3} - \tau_{2-3}]$, significantly enhanced pulse overlaps have not been achieved due to the observed pulse dynamics with split-up components in the time domain. While gain competition effects, potentially causing the split up, require more research efforts to fully understand them, a strategy has been developed to circumvent this effect and maximize the pulse overlap.

This strategy can be motivated by the recorded pulse shapes in Fig. 4.19b. The graph plots four pulse shapes in 1-λ emission. The non-PM TCFL is either operating at FBG 1 (beginning of tuning range) or FBG 3 (end of tuning range). For both wavelengths, the corresponding pulse is recorded with two different modulation periods T_{MP} highlighting the impact on their shape as investigated in subsection 4.1.2. The default modulation periods $T_{MP,0}$ generating symmetric parabola-like pulses are listed for all three emission wavelengths in the yellowish box. For the initial investigations presented in Fig. 4.17 and Fig. 4.18, $T_{MP} = 963.16\,ns$ has been chosen in the central area of the different $T_{MP,0}$ over the tuning range, supposedly enabling an optimized match with the exact PRTT in the cavity and highest signal contrast (see Fig. 3.18). However, in this range of T_{MP}, the pulse shape quickly varies over the tuning range as pictured by the two reddish traces in Fig. 4.19b. While the pulse at FBG 3 shows a nearly parabola-like shape with weak steepening on the leading edge, the pulse at FBG 1 shows a steep trailing edge. Thus, matching the pulses and their behavior for a maximized overlap in 2-λ operation could be disturbed by the different pulse formation regimes. In contrast, mild detuning of T_{MP} to $T_{MP} = 963.08\,ns$, while still enabling excellent signal contrast, ensures the pulses to operate in the same formation regime with respect to $T_{MP,0}$ throughout the tuning range. Accordingly, the respective blueish traces show matching pulse shapes with significant steepening on the trailing edge and similar pulse duration. Both pulses at FBG 1 and FBG 3 resemble each other indicating steady conditions in their properties throughout the tuning range. In prospect, they may also show identical behavior in 2-λ operation enabling maximized pulse overlaps.

This is investigated in Fig. 4.20. The gating settings are optimized for 2-λ operation working at the mildly detuned $T_{MP} = 963.08\,ns$. While graph a) targets the same wavelength pair as discussed in the previous figures, i.e. FBG 1 and FBG 2, graph b) exemplarily pictures the

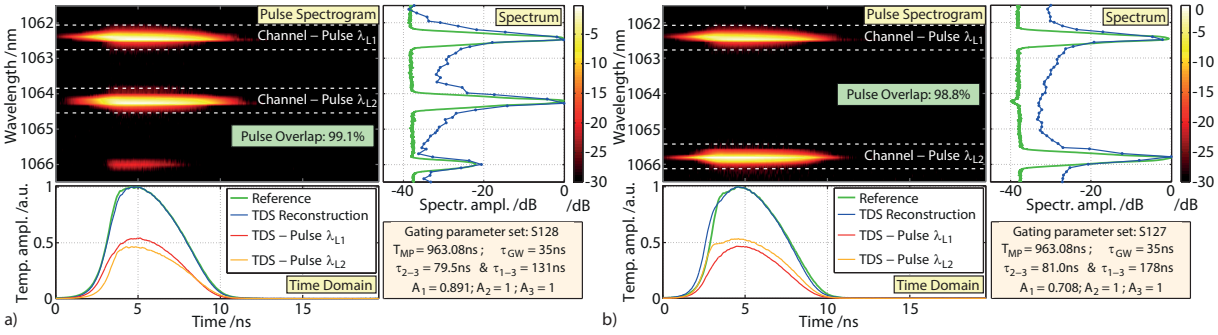

Fig. 4.20: The graphs show two measured pulse spectrograms (averaged acquisition) for the wavelength pairs of FBG 1 & FBG 2 (part a) as well as FBG 1 & FBG 3 (part b). The measurements are recorded with optical gating parameters optimized for maximized pulse overlap in 2-λ operation.

optimization of pulse overlap at another set operating λ_{L1} and λ_{L2} at FBG 1 and FBG 3. The residual set of FBG 2 and FBG 3 has achieved similar results. In all three 2-λ combinations, the discussed settings enable pulse overlap factors approaching 100%. As indicated in the pulse spectrogram and confirmed by the temporal traces in graph a) and b), the pulses in either wavelength show similar shape with coinciding amplitudes and strengths confirming the good match in balanced 2-λ operation. Accordingly, in graph a), a comparably strong FWM side band rises in the overlapping zone of λ_{L1} and λ_{L2} resulting in a peaking FWM strength of $-20\,dB$ in the emission spectrum.

4.2.4.5 Single-pulse analysis

In principle, the measurements with the TDS discussed in Fig. 4.18 and Fig. 4.20 have also been performed with a single-pulse acquisition at the OSCI showing fundamentally the same characteristics. To highlight the simultaneous emission at two wavelengths λ_{L1} and λ_{L2} with

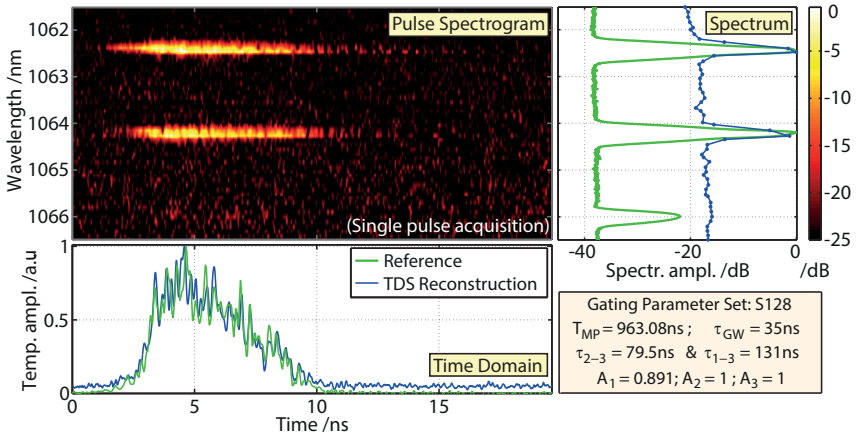

Fig. 4.21: The figure shows a pulse spectrogram of the TCFL in 2-λ mode operating at the wavelength pair of FBG 1 & FBG 2. It is recorded for a single laser pulse (no averaging) with the TCFL operating at the same gating settings as in Fig. 4.20a confirming steady dual-wavelength emission in each round trip.

overlapping pulses, Fig. 4.21 features the single-pulse analysis for the gating settings tested in Fig. 4.20a. In this sample acquisition mode, the measurement noise is significantly stronger. This degrades the dynamic range in the measurement as well as induces a spiky character to the

temporal traces. Hence, more extensive data analysis is not applicable. Nevertheless, the graph confirms both emission wavelengths to be emitted simultaneously showing a good overlap. A small amplitude mismatch of about $1.2\,dB$ is measured which could be connected to the discrete spectral sampling of the DTG array. Still, this measurement confirms 2-λ operation even down to single-pulses level verifying this emission mode to be no artifact of an averaged spectral data acquisition with an OSA.

4.2.4.6 Summary

In summary, both measurements in Fig. 4.20 as well as the single-pulse analysis in Fig. 4.21 demonstrated an excellent pulse overlap in this unique 2-λ operation mode. The approach in fine tuning τ_{1-3} and τ_{2-3} in order to match the relative pulse positions, as well as weakly detuning T_{MP} from $T_{MP,0}$ throughout the tuning range to operate in the same pulse formation regime proves successful in maximizing the pulse overlap. However, more research is required to model this behavior. Still, based on a prior calibration of the temporal gating settings, reliable 2-λ emission can be ensured throughout the tuning range. With these results, tunable 2-λ operation in the TCFL provides huge potential to address demanding applications based on nonlinear frequency mixing with a single fiber-integrated laser system potentially setting the benchmark in robustness and cost. On the other side, the study which has been discussed in Fig. 4.18 indicates that by changing the gating delay $[\tau_{1-3} - \tau_{2-3}]$, the relative pulse delay between the emission of both wavelengths λ_{L1} and λ_{L2} can be variably tuned. Due to the flexibility in remote-controlling the electrical gating signal, this mode could be interesting in pump-probe applications with one wavelength pumping a process and the other one probing the result with variable delays. However, to confirm this idea, more investigations of this mode would be required.

4.2.5 Scaling of multi-wavelength emission

As conceptually noted in subsection 4.2.2, the flexibility in the optical gating approach enables the number of tunable emission wavelengths to be scaled even beyond the 2-λ regime. With $[p+1]$ ($p \in \mathbb{N}$, $p \leq N$) transmission windows applied at the AOM, p response times of the filter section could be promoted for lasing enabling potentially p emission wavelengths. As in the 2-λ mode, the spectral amplitudes could be conveniently balanced by the amplitudes of the optical gates.

Based on a simultaneous and tunable triple-wavelength (3-λ) emission, the prospect of this concept is experimentally investigated. Fig. 4.22 depicts two graphs. The top graph features generic gating signals applying 4 transmission windows with specific timings, respectively. The order of the gates is labeled for the blue trace. As joint transition gate of the $p = 3$ target wavelengths (λ_{L1}, λ_{L2} and λ_{L3}), the time axis is referenced to gate 4 returning the synchronized filter feedback towards the lower cavity branch. In the graph at the bottom, the measured emission spectra are depicted corresponding to the gating signals. For demonstrating tunability in the 3-λ mode, three different parameter sets in the gating signal are investigated. They are recorded at OC1 of the PM TCFL employing FBG array C. The blue trace depicts the

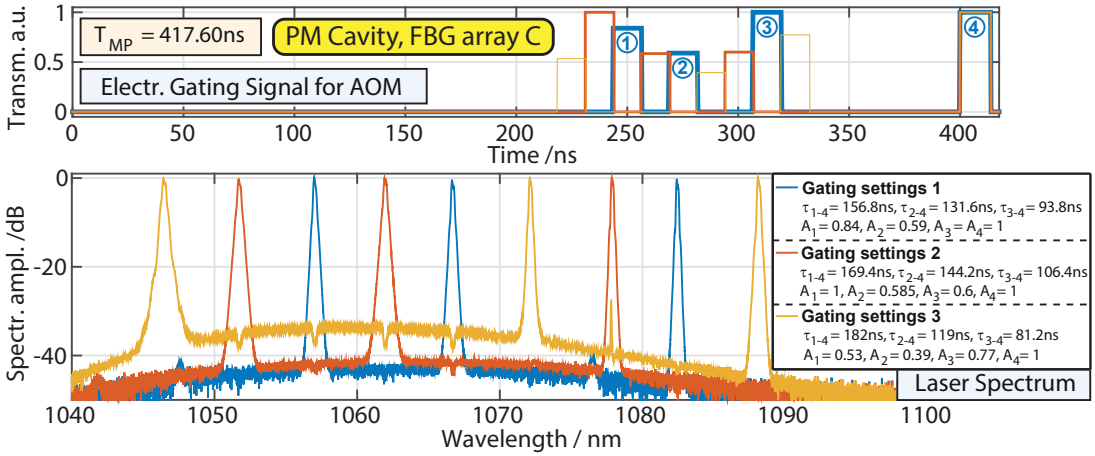

Fig. 4.22: The plots depict the measured emission spectra in tunable triple-wavelength emission (graph at the bottom) as well as the corresponding generic optical gating functions (top graph). The three exemplary triplets cover a tuning bandwidth of $40\,nm$.

first wavelength triplet emitting at $\lambda_{L1} = 1082\,nm$, $\lambda_{L2} = 1067\,nm$ and $\lambda_{L3} = 1057\,nm$. It features the typical emission properties of FBG array tuned lasers with narrow linewidths and high signal contrast ($> 40\,dB$). The red trace pictures an example with another wavelength triplet ($\lambda_{L1} = 1077\,nm$, $\lambda_{L2} = 1062\,nm$ and $\lambda_{L3} = 1052\,nm$) and equal emission characteristics. While in both cases, the spectral amplitudes of the emission lines are balanced by lowering two gating amplitudes, respectively, providing enough freedom, the gating signal of the yellow trace applies losses to gate 1, gate 2 and gate 3 in order to suppress parasitic emission lines in asynchronous regimes. This is synonymous to the behavior discussed for the optical gating regimes in 2-λ operation (see subsection 4.2.3). The rising losses cause a slightly elevated ASE background of the yellow emission spectrum. Still, another wavelength triplet is demonstrated with wavelengths ranging over $40\,nm$ ($\lambda_{L1} = 1087\,nm$, $\lambda_{L2} = 1072\,nm$ and $\lambda_{L3} = 1047\,nm$). The onset of a parasitic asynchronous emission line at OC1 is indicated by the small peak at $1077\,nm$ (arising from gate 1 and gate 3). Further triplets could be demonstrated by applying different gating parameter sets. Applying equation(4.6), 165 dissimilar triplets would be feasible with FBG array C.

With the measurements in Fig. 4.22, discretely tunable 3-λ emission over a tuning range of $40\,nm$ is successfully demonstrated. Accordingly, an identical experimental laser setup of the TCFL enables tunable single-wavelength as well as independently tunable dual-wavelength and triple-wavelength emission simply by adapting the electrical driving signal. Potentially, even more simultaneous emission wavelengths may be realized. An experimental demonstration for $p > 3$ wavelengths was technologically prohibited by the employed AOM due to a duty cycle in the gating signal exceeding the specified limit of the modulator.

More emission wavelengths ($p > 3$) are connected to a rising number of transmission windows ($[p + 1]$) at the AOM. This potentially opens up even further parasitic pulse paths degrading the tuning characteristics. However, precautions in the resonator design, as discussed for 1-λ and 2-λ mode, may ensure proper operation on p ($p \leq N$) emission lines providing the basis for scaling tunable multi-wavelength operation. A generalized criterion for the laser layout is required to suppress parasitic pulse regimes independent of p.

For an universal condition, the laser is assumed to enforce solely the normal gating regime ($T_{MP} > 2 \cdot \tau_{1-2,N}$, compare to equation(3.7)). This enables inverse gating times (i.e. τ'_{1-2}) to be disregarded. In particular, the first transmission window of each cycle works as injecting gate to the filter section. On the other side, enforcing the synchronous multi-wavelength (p emission lines) gating regime at OC1 means that the $[p+1]^{th}$ gate as last transmission window in each cycle jointly collects the complete filter response to continue the round trip. Any other gate, transmitting a response signal from the filter, would operate in a parasitic regime. Accordingly, within the corresponding ensemble of gating times $\tau_{i-[p+1]}$, each intermediate delay τ_{i-j} $(i, j \in \mathbb{N})$ for $i < j < [p+1]$ must be prohibited to match another response time in the FBG array. This is enforced by, e.g., ensuring the minimum gating delay $\tau_{p-[p+1]}$ in the desired synchronous regime at OC1 to always exceed the maximum gating delay τ_{1-p} in a parasitic regime, i.e. $\tau_{p-[p+1]} > \tau_{1-p}$. Equivalently, within the tuning range of p emission wavelengths, only gating delays $\tau_{i-[p+1]}$ $(i \leq p)$ provide spectrally filtered feedback from the FBG array. Transferring this to the single-wavelength regime targeting a direct design condition for the cavity, the minimum response time from the filter section (with respect to the modulator) is required to exceed the time of flight difference between first and last grating, i.e. $\tau_{1-2,1} > (\tau_{1-2,N} - \tau_{1-2,1})$. Rearranging this relation, the resonator layout must meet the requirement

$$\tau_{1-2,1} > \frac{1}{2} \cdot \tau_{1-2,N} \ . \tag{4.8}$$

This can be fulfilled by additional delay fiber in between the modulator and FBG 1 or a comparably short FBG array.

Without any direct application scenario of more than two emission wavelengths, this condition has not been verified experimentally. Still, it should enable tunable multi-wavelength emission to be scaled to p emission lines ($p \leq N$) operating solely in the synchronous gating regime at OC1 without any parasitic laser peaks. Importantly, any detrimental resonance effects as discussed for pulse echos in subsubsection 3.3.1.2 are not considered yet by this condition.

5 Conclusion and outlook

Dispersion tuning based on chirped FBG structures combines unique advantages that open up a wide field of applications for tunable fiber lasers in several branches. The key element is depicted by the spectral filter providing unique spectral freedom to exhaust the broad gain regions of rare-earth doped fibers. While continuously-chirped FBGs enable continuous tuning ranges, discretely chirped FBG arrays as employed in this work enable tailored tuning characteristics. This particularly comprises record bandwidths, but also features adapted spectral resolutions as well as specific emission lines customized to an application. On the other side, adding up to the typical advantages of single-mode fiber lasers exhibiting especially an excellent beam quality, the monolithic filter design provides the basis for fiber-integrated layouts. Accordingly, robust and compact solutions can be established working with high stability, user-friendly operations as well as low-maintenance requirements which reduces cost and pushes the relevance for industrial applications. The potential of this approach for pulsed systems has already been demonstrated by commercial solutions employing a sigma-ring cavity layout [149].

In this thesis, a new tuning method has been developed that combines these advantages with a new cavity layout. The theta-ring resonator induces two filter interactions per cavity round trip with counter-propagating passes that balance the characteristic spectral delays induced by the distributed filter feedback. Accordingly, a constant pulse repetition rate (PRR) throughout the tuning range is achieved solving a bottleneck of the previous approach in the sigma-ring resonator. While this is important for applications relying on synchronized processes such as clocked detectors or an interaction with another pulsed laser in nonlinear frequency mixing, a steady PRR with a fixed duty cycle also ensures consistent pulse properties which has been a limitation of sigma-ring resonators employing long FBG arrays [139]. As a consequence, tunable theta-ring lasers with FBG arrays may exhibit huge potential to address a wider range of applications, such as in life sciences, spectroscopy, medical technology and industry.

Within the framework of this thesis, three main contributions have been addressed: while the main challenge was to realize spectral tuning by optical gating in the theta-ring resonator and to investigate its characteristics, the second part of the thesis discusses advanced operation concepts to highlight the flexibility in the new tuning approach towards tailored emission properties and new applications. Accordingly, a new method has been established to measure the fiber dispersion parameter for a sample. Furthermore, a novel operation regime is analyzed uniquely enabling synchronized and independently tunable multi-wavelength emission from a single laser oscillator.

After establishing spectral tuning in the theta-ring resonator, the tuning concept has been investigated extensively in a PM as well as a non-PM layout regarding design criteria to optimize operations. The experiments revealed spectral overlapping FBGs to sensitively degrade the emission properties by detrimental losses in the filter section. In order to avoid internal Fabry-Pérot sub-resonators and to cleanly lock the laser on a single filter element, isolated spectral filter lines are required in the discrete FBG array, ultimately limiting the potential tuning resolution by the grating linewidths. Furthermore, the branched layout of the theta-ring resonator

is prone to parasitic pulse paths inducing e.g. undesired emission wavelengths. Solutions have been established balancing resonator dimensions by additional delay fiber to operate the laser in the desired pulse regime and avoid any ambiguity in the optical gating signal. In an optimized resonator layout, the tunable theta cavity fiber laser (TCFL) features excellent emission properties with the spectral tuning behavior perfectly following the characteristics of the FBG array. A narrow linewidth ($< 150\,pm$) as well as high spectral signal contrast with ASE suppression reaching values beyond $45\,dB$ have been demonstrated for the discrete tuning method with steady pulse properties throughout the tuning range. Providing even some flexibility to modify the temporal emission properties, the pulse duration itself can be tuned in a small range of around $10\,ns$ by electrically changing the optical gating window durations. With fast pulse formation times of $< 5\ \mu s$, the TCFL would also qualify for applications requiring high sweep speeds beyond $10\,kHz$. A considerable tuning range of $50\,nm$ has been established in the Ytterbium band approaching the modeled limit of about $65\,nm$ for the given resonator. The implemented bandwidth was solely restricted by the FBG array with a different design potentially exhausting the full potential. As an additional feature, the output coupler position within the resonator offers design freedom to tailor the laser signal. While an output coupler in the upper cavity branch (OC2) features almost ASE free signals with excellent spectral signal contrast, high output powers above $100\,mW$ are feasible from the oscillator at an output coupler in the lower cavity branch (OC1). This simplifies further power scaling by additional power amplifiers. Overall, considering the design criteria, the TCFL showed excellent emission characteristics with remarkable freedom to match diverse demands on the laser.

As discussed in the first part of chapter 4, the TCFL has been utilized to introduce a new method for the dispersion analysis of fiber samples. Minor pulse shape variations have been traced back on small mismatches of the applied modulation period to the precise pulse round-trip time in the cavity, varying along the tuning range due to dispersion. Reversing this effect, an automated measurement procedure has been developed evaluating the pulse symmetry along the tuning range with a self-convolution criterion to analyze the net cavity dispersion. Applying this procedure to the plain TCFL (reference) as well as an extended cavity with a fiber under test, its dispersion properties can be retrieved within the operation window. As an example, the mean dispersion parameter has been measured for two fiber samples of `Nufern PM980-XP`. While simulations showed a deviation of about 10% to the measurement with the TCFL, which is probably caused by an oversimplified numerical model and deviating fiber specifications, a reference value has been obtained by an alternative method employing spectral interferometry. With a respective deviation of 0.3% and 1.3% in the experimental results of the two samples between both methods, the analysis with the TCFL has been verified. This concept features an outstanding sensitivity in the range of $1\,ps$ employing only standard electronics. With a simple and direct temporal measurement of the cavity dispersion in a small spectral range, the TCFL may provide a promising tool to analyze the dispersion parameter in specific scenarios such as quality management demanding quick assessment. Still, conventional methods based on spectral interferometry may not be challenged for extensive dispersion measurements enabling spectrally resolved curves over broad bandwidths and highest sensitivities (i.e. shorter lengths of the fiber under test).

In the last part, spectral tuning in the TCFL has been extended towards an independently tunable multi-wavelength emission. The basis for this operation mode is provided by the theta-ring resonator layout with constant pulse round-trip times for all wavelengths ensuring synchronized output. Hence, an adapted optical gating signal, switching three or more transmission windows, enables multi-wavelength emission from a single oscillator. This mode has been implemented and investigated based on dual-wavelength and triple-wavelength emission with a tuning bandwidth of up to $50\,nm$. In dual-wavelength operation, all discrete wavelength pairs provided by the FBG array design have been demonstrated verifying independent tunability. The optical gating parameters conveniently select the emission wavelengths as well as balance their spectral amplitudes. Due to gain competition detuning the peak values over time, an industrial application of this mode may demand a feedback loop and iterative control of the gating parameters for compensation. Simultaneous emission of two emission wavelengths in each round trip has been verified with a fiber-integrated time-delay spectrometer that has been established for further analyzing this operation regime. The pulse overlap has been investigated and optimized with this tool reaching 99% with fine-tuned gating parameters. With confirmed simultaneous emission, the dual-wavelength mode in the TCFL together with the customizability of the tuning range qualifies as novel pump source for nonlinear process. Based on frequency mixing, other spectral ranges (e.g. the Terahertz domain) may be addressed by fiber laser technology, which are hard to access with common gain media. This exhibits huge potential for tailored light sources in spectroscopy.

Compared to other multi-wavelength approaches, this concept operates with a programmable tuning mechanism in a single oscillator. Thus, the emission is inherently synchronized and the detailed pulse overlap can be fine-tuned by the gating parameters. Additionally, driven by the optical gating signal, it features a unique scalability. While the number of simultaneously oscillating laser lines can be extended by electrically applying more transmission windows, the overall ensemble of potential emission wavelengths is increased by incorporating more gratings into the FBG array.

Within the framework of this thesis, a new tuning mechanism has been established that provides unique advantages to extend the application field of fiber lasers. Further research may be connected to a numerical analysis of the pulse formation in the cavity. This could provide deeper insights in some of the observed effects, such as the pulse dynamics in dual-wavelength operation or the pulse shape variations utilized for the dispersion analysis. Furthermore, this tuning concept may be fused with a new mode-locking approach in fiber lasers demonstrated recently [45, 96]. The scheme based on a Mamyshev-oscillator attracts recent attention in fiber lasers enabling high power levels. The discrete structure of the FBG array in the TCFL correlates with the basic mode-locking principle of detuned spectral filter interactions inducing nonlinear spectral broadening by pulse shortening for maintaining a laser resonator [75]. Fusing the mode-locking mechanism with tunable operation could provide a powerful platform for tunable fiber lasers.

Additionally, an application of the TCFL is already planned to highlight its prospects. As suggested previously, the dual-wavelength mode may be utilized for developing light sources in new spectral ranges. An international research project (name: TERATUNE) is ongoing applying

a Thulium-doped TCFL in dual-wavelength mode and a subsequent fiber amplifier chain to pump nonlinear frequency generation towards the Terahertz domain [146]. With a tunable beat frequency in dual-wavelength operation, this would transfer to a fiber laser-pumped and tunable Terahertz source.

Bibliography

[1] *Data sheet: Corning HI 1060 (accessed via https://www.corning.com/media/worldwide/csm/documents/HI 1060 Specialty Fiber PDF.pdf on 30.07.2018).*

[2] *Data sheet: LIEKKI Yb1200-6/125DC-PM (accessed via http://www.nlight.net/products/optical-fibers/21-LIEKKI-Yb12006125 on 28.07.2018).*

[3] *Data sheet: Nufern PM980-XP (accessed via http://www.nufern.com/pam/optical_fibers/964/PM980-XP/ on 28.07.2018).*

[4] *Data sheet: Thorlabs Single Mode Fiber 1060XP (accessed via www.thorlabs.com/thorproduct.cfm?partnumber=1060XP on 12.07.2018).*

[5] https://en.wikipedia.org/wiki/Double-clad_fiber (time stamp: 06.04.2018), 2011.

[6] G. P. Agrawal. *Nonlinear Fiber Optics*. Elsevier Academic Press, 4th edition, 2007.

[7] V. Akulov, D. Afanasiev, S. Babin, D. Churkin, S. Kablukov, M. Rybakov, and A. Vlasov. Frequency tuning and doubling in Yb-doped fiber lasers. *Laser Physics*, 17(2):124–129, 2007.

[8] I. Armas-Rivera, C. Cuadrado-Laborde, A. Carrascosa, E. A. Kuzin, G. Beltrán-Pérez, A. Díez, and M. V. Andrés. Dissipative soliton resonance in a full polarization-maintaining fiber ring laser at different values of dispersion. *Optics Express*, 24(9):9966–9974, 2016.

[9] C. Askins, M. Putnam, G. Williams, and E. Friebele. Stepped-wavelength optical-fiber Bragg gratings arrays fabricated in line on a draw tower. *Optics Letters*, 19(2):147–149, 1994.

[10] T. Balciunas, C. Fourcade-Dutin, G. Fan, T. Witting, A. Voronin, A. Zheltikov, F. Gerome, G. Paulus, A. Baltuska, and F. Benabid. A strong-field driver in the single-cycle regime based on self-compression in a kagome fibre. *Nature Communications*, 6:6117, 2015.

[11] C. Barnard, P. Myslinski, J. Chrostowski, and M. Kavehrad. Analytical model for rare-earth-doped fiber amplifiers and lasers. *IEEE Journal of Quantum Electronics*, 30(8):1817–1830, Aug 1994.

[12] M. Bass, editor. *Handbook of Optics - Fundamentals, Techniques & Design (2nd Edition)*, volume 1. McGraw-Hill, 2nd edition, 1995.

[13] M. Becker, J. Bergmann, S. Brückner, M. Franke, E. Lindner, M. W. Rothhardt, and H. Bartelt. Fiber Bragg grating inscription combining DUV sub-picosecond laser pulses and two-beam interferometry. *Optics Express*, 16(23):19169–19178, 2008.

[14] M. Becker, T. Elsmann, I. Latka, M. Rothhardt, and H. Bartelt. Chirped phase mask interferometer for fiber Bragg grating array inscription. *Journal of Lightwave Technology*, 33(10):2093–2098, 2015.

[15] R. W. Boyd. *Nonlinear Optics*. Academic Press, 3rd edition, 2008.

[16] I. N. Bronstein, J. Hromkovic, B. Luderer, H.-R. Schwarz, J. Blath, A. Schied, S. Dempe, G. Wanka, and S. Gottwald. *Taschenbuch der Mathematik*, volume 1. Springer-Verlag, 2012.

[17] B. Burgoyne, A. Dupuis, and A. Villeneuve. An experimentally validated discrete model for dispersion-tuned actively mode-locked lasers. *IEEE Journal of Selected Topics in Quantum Electronics*, 20(5):390–398, 2014.

[18] T. F. Carruthers, I. N. Duling, M. Horowitz, and C. R. Menyuk. Dispersion management in a harmonically mode-locked fiber soliton laser. *Optics Letters*, 25(3):153–155, 2000.

[19] A. Castillo-Guzman, R. Selvas, C. Calles, and M. Basurto-Pensado. Gain and numerical modelling of rare-earth doped fiber devices. In *2006 Multiconference on Electronics and Photonics*, pages 35–39, Nov 2006.

[20] K. Chan and C. Shu. Compensated dispersion tuning in harmonically mode-locked fiber laser. *Applied Physics Letters*, 75(7):891–893, 1999.

[21] I. Chang. *Acousto-optic signal processing: theory and implementation - Chapter 5: Acousto-optic tunable filters*. Marcel Dekker, 1996.

[22] D. Chen, S. Qin, and S. He. Channel-spacing-tunable multi-wavelength fiber ring laser with hybrid raman and erbium-doped fiber gains. *Optics Express*, 15(3):930–935, Feb 2007.

[23] C. Chojetzki, M. W. Rothhardt, J. Ommer, S. Unger, K. Schuster, and H.-R. Mueller. High-reflectivity draw-tower fiber Bragg gratings-arrays and single gratings of type II. *Optical Engineering*, 44(6):060503, 2005.

[24] A. Chong, J. Buckley, W. Renninger, and F. Wise. All-normal-dispersion femtosecond fiber laser. *Optics Express*, 14(21):10095–10100, 2006.

[25] L. G. Cohen. Comparison of single-mode fiber dispersion measurement techniques. In *Optical Fiber Communication Conference*, page TUF1. Optical Society of America, 1985.

[26] L. G. Cohen and C. Lin. Pulse delay measurements in the zero material dispersion wavelength region for optical fibers. *Applied Optics*, 16(12):3136–3139, 1977.

[27] J. Crisp and B. Elliott. *Introduction to Fiber Optics*. Newnes, 3nd edition, 2005.

[28] W. Demtröder. *Laser Spectroscopy: Vol. 1: Basic Principles*. Springer, 4 edition, 2008.

[29] E. Desurvire, J. Sulhoff, J. Zyskind, and J. Simpson. Spectral dependence of gain saturation and effect of inhomogeneous broadening in Erbium-doped aluminosilicate fiber amplifiers. In *Optical Amplifiers and Their Applications*, 1990.

[30] M. J. Digonnet, editor. *Rare-Earth-Doped Fiber Lasers and Amplifiers*. Marcel Dekker Inc., 2nd edition, 2001.

[31] L. Dong, J.-L. Archambault, L. Reekie, P. Russel, and D. Payne. Single pulse Bragg gratings written during fibre drawing. *Electronics Letters*, 29(17):1577–1578, 1993.

[32] L. Dong and B. Samson. *Fiber Lasers: Basics, Technology, and Applications*. CRC Press, 2016.

[33] N. Doran and D. Wood. Nonlinear-optical loop mirror. *Optics Letters*, 13(1):56–58, 1988.

[34] C. Dorrer. Chromatic dispersion characterization by direct instantaneous frequency measurement. *Optics Letters*, 29(2):204–206, 2004.

[35] F. J. Duarte. *Tunable laser applications*. CRC press, 2016.

[36] J. M. Dudley, G. Genty, and S. Coen. Supercontinuum generation in photonic crystal fiber. *Reviews of modern physics*, 78(4):1135, 2006.

[37] J. M. Dudley and J. R. Taylor. *Supercontinuum generation in optical fibers*. Cambridge University Press, 2010.

[38] T. Erdogan. Fiber grating spectra. *Journal of Lightwave Technology*, 15(8):1277–1294, 1997.

[39] Y.-X. Fan, F.-Y. Lu, S.-L. Hu, K.-C. Lu, H.-J. Wang, G.-Y. Zhang, and X.-Y. Dong. Narrow-linewidth widely tunable hybrid q-switched double-clad fiber laser. *Optics Letters*, 28(7):537–539, Apr 2003.

[40] Q. Fang, J. Li, W. Shi, Y. Qin, Y. Xu, X. Meng, R. A. Norwood, and N. Peyghambarian. 5 kw near-diffraction-limited and 8 kW high-brightness monolithic continuous wave fiber lasers directly pumped by laser diodes. *IEEE Photonics Journal*, 9(5):1–7, Oct 2017.

[41] Q. Fang, Z. Wang, L. Jin, J. Liu, Y. Yue, Y. Liu, G. Kai, S. Yuan, and X. Dong. Dispersion design of all-solid photonic bandgap fiber. *JOSA B*, 24(11):2899–2905, 2007.

[42] R. Frankel and J. Hoose. Tunable multi-wavelength laser device, Aug. 5 2002. US Patent App. 10/212,844.

[43] O. Frazão, R. M. Silva, M. S. Ferreira, J. L. Santos, and A. B. L. Ribeiro. Suspended-core fibers for sensing applications. *Photonic Sensors*, 2(2):118–126, 2012.

[44] A. Frenkel and H. Chinlon Lia. Etalon filters for optical channel selection in wavelength division multiplexed fiber systems US Patent 4,813,756, 1989.

[45] W. Fu, L. G. Wright, P. Sidorenko, S. Backus, and F. W. Wise. Several new directions for ultrafast fiber lasers. *Optics Express*, 26(8):9432–9463, 2018.

[46] M. Gagné, S. Loranger, J. Lapointe, and R. Kashyap. Fabrication of high quality, ultra-long fiber Bragg gratings: up to 2 million periods in phase. *Optics Express*, 22(1):387–398, 2014.

[47] M. A. Galle and L. Qian. Low-coherence virtual reference interferometry for dispersion analysis. *IEEE Photonics Technology Letters*, 26(20):2020–2022, 2014.

[48] A. Galvanauskas, M. Fermann, D. Harter, K. Sugden, and I. Bennion. All-fiber femtosecond pulse amplification circuit using chirped Bragg gratings. *Applied Physics Letters*, 66(9):1053–1055, 1995.

[49] F. Ganikhanov, S. Carrasco, X. S. Xie, M. Katz, W. Seitz, and D. Kopf. Broadly tunable dual-wavelength light source for coherent anti-Stokes Raman scattering microscopy. *Optics Letters*, 31(9):1292–1294, May 2006.

[50] R. Gaulton, F. Danson, F. Ramirez, and O. Gunawan. The potential of dual-wavelength laser scanning for estimating vegetation moisture content. *Remote Sensing of Environment*, 132:32 – 39, 2013.

[51] M. Giguere, V. N. Dang, and J. Salhany. Mid-IR laser source is widely tunable for standoff explosives detection. *LASER FOCUS WORLD*, 51(4):59–61, 2015.

[52] C. R. Giles and E. Desurvire. Modeling Erbium-doped fiber amplifiers. *Journal of Lightwave Technology*, 9(2):271–283, Feb 1991.

[53] C. Goh, M. R. Mokhtar, S. A. Butler, S. Set, K. Kikuchi, and M. Ibsen. Wavelength tuning of fiber Bragg gratings over 90 nm using a simple tuning package. *Photonics Technology Letters, IEEE*, 15(4):557–559, 2003.

[54] T. Gottschall, T. Meyer, M. Baumgartl, C. Jauregui, M. Schmitt, J. Popp, J. Limpert, and A. Tünnermann. Fiber-based light sources for biomedical applications of coherent anti-Stokes Raman scattering microscopy. *Laser & Photonics Reviews*, 9(5):435–451, 9 2015.

[55] T. Gottschall, T. Meyer, M. Schmitt, J. Popp, J. Limpert, and A. Tünnermann. Four-wave-mixing-based optical parametric oscillator delivering energetic, tunable, chirped femtosecond pulses for non-linear biomedical applications. *Optics Express*, 23(18):23968–23977, Sep 2015.

[56] S. G. Grubb and D. F. Welch. Patent: Double-clad optical fiber with improved inner cladding geometry, 2000.

[57] B.-O. Guan, H.-Y. Tam, H. L. Chan, X.-Y. Dong, C.-L. Choy, and M. S. Demokan. Temperature-tuned Erbium-doped fiber ring laser with polymer-coated fiber grating. *Optics Communications*, 202(4-6):331 – 334, 2002.

[58] P. Günter, J.-P. Huignard, and A. M. Glass. *Photorefractive materials and their applications*, volume 1. Springer, 1988.

[59] M. Guy, D. Noske, and J. Taylor. Generation of femtosecond soliton pulses by passive mode locking of an Ytterbium-erbium figure-of-eight fiber laser. *Optics Letters*, 18(17):1447–1449, 1993.

[60] V. Hagemann. *Untersuchungen zum dynamischen Einzelpuls-Einschreiben von Faser-Bragg-Gittern und zu deren Anwendung*. PhD thesis, Friedrich-Schiller-Universität Jena, 2000.

[61] Y.-G. Han, T. V. A. Tran, and S. B. Lee. Wavelength-spacing tunable multiwavelength erbium-doped fiber laser based on four-wave mixing of dispersion-shifted fiber. *Optics Letters*, 31(6):697–699, Mar 2006.

[62] D. Hanna, R. Percival, I. Perry, R. Smart, P. Suni, and A. Tropper. An Ytterbium-doped monomode fibre laser: Broadly tunable operation from 1.010 um to 1.162 um and three-level operation at 974 nm. *Journal of Modern Optics*, 37(4):517–525, 1990.

[63] J. Hecht. PHOTONIC FRONTIERS: FIBER LASERS: Fiber lasers ramp up the power. https://www.laserfocusworld.com/articles/print/volume-45/issue-12/features/photonic-frontiers-fiber-lasers-fiber-lasers-ramp-up-the-power.html (time stamp: 16.02.2018), 2009.

[64] R. Hegenbarth, A. Steinmann, S. Sarkisov, and H. Giessen. Milliwatt-level mid-infrared (10.5 - 16.5 μ m) difference frequency generation with a femtosecond dual-signal-wavelength optical parametric oscillator. *Optics Letters*, 37(17):3513–3515, Sep 2012.

[65] A. M. Heidt. Pulse preserving flat-top supercontinuum generation in all-normal dispersion photonic crystal fibers. *JOSA B*, 27(3):550–559, 2010.

[66] A. M. Heidt, A. Hartung, G. W. Bosman, P. Krok, E. G. Rohwer, H. Schwoerer, and H. Bartelt. Coherent octave spanning near-infrared and visible supercontinuum generation in all-normal dispersion photonic crystal fibers. *Optics Express*, 19(4):3775–3787, 2011.

[67] S. W. Hell and J. Wichmann. Breaking the diffraction resolution limit by stimulated emission: stimulated-emission-depletion fluorescence microscopy. *Optics Letters*, 19(11):780–782, 1994.

[68] A. Hideur, T. Chartier, C. Özkul, and F. Sanchez. All-fiber tunable Ytterbium-doped double-clad fiber ring laser. *Optics Letters*, 26(14):1054–1056, 2001.

[69] K. Hill, Y. Fujii, D. C. Johnson, and B. Kawasaki. Photosensitivity in optical fiber waveguides: Application to reflection filter fabrication. *Applied Physics Letters*, 32(10):647–649, 1978.

[70] K. O. Hill and G. Meltz. Fiber Bragg grating technology fundamentals and overview. *Journal of Lightwave Technology*, 15(8):1263–1276, 1997.

[71] J. Hubbert. The german biophotonics industry and the global biophotonics market: Key segments, opportunities and risks. *Optik & Photonik*, 9(2):27–29, 2014.

[72] G. Imeshev, I. Hartl, and M. E. Fermann. Chirped pulse amplification with a nonlinearly chirped fiber Bragg grating matched to the Treacy compressor. *Optics Letters*, 29(7):679–681, Apr 2004.

[73] M. Y. Jeon, N. Kim, J. Shin, J. S. Jeong, S.-P. Han, C. W. Lee, Y. A. Leem, D.-S. Yee, H. S. Chun, and K. H. Park. Widely tunable dual-wavelength Er3+-doped fiber laser for tunable continuous-wave terahertz radiation. *Optics Express*, 18(12):12291–12297, Jun 2010.

[74] Y. Jeong, J. Nilsson, J. K. Sahu, D. N. Payne, R. Horley, L. Hickey, and P. Turner. Power scaling of single-frequency Ytterbium-doped fiber master-oscillator power-amplifier sources up to 500 W. *IEEE Journal of Selected Topics in Quantum Electronics*, 13(3):546–551, 2007.

[75] M. Jäger and A. Lorenz. Passiv modengekoppelter faseroptischer Lasergenerator, Patent: DE102014117555A1, 2014.

[76] M. Jäger and T. Tieß. Faseroptischer Lasergenerator, Patent: DE102015106633B4, 2018.

[77] M. S. Kang, M. S. Lee, J. C. Yong, and B. Y. Kim. Characterization of wavelength-tunable single-frequency fiber laser employing acoustooptic tunable filter. *Journal of Lightwave Technology*, 24(4):1812–1823, 2006.

[78] R. Kashyap. *Fiber Bragg Gratings*. Academic press, 2009.

[79] A. Kersey, M. Davis, H. Patrick, M. Leblanc, K. Koo, C. Askins, M. Putnam, and E. Friebele. Fiber grating sensors. *Journal of Lightwave Technology*, 15(8):1442–1463, 1997.

[80] Y. Kim, A. Archambault, A. Dupuis, B. Burgoyne, G. Pena, and A. Villeneuve. Wavelength and pulse width tunable 1 μm Yb-doped programmable fiber laser. In *Lasers and Electro-Optics (CLEO), 2013 Conference on*, pages 1–2. IEEE, 2013.

[81] K. Kincade, A. Nogee, G. Overton, D. Belforte, and C. Holton. ANNUAL LASER MARKET REVIEW & FORECAST: Lasers enabling lasers. *LASER FOCUS WORLD*, 54(1):42–67, 2018.

[82] A. N. Kolyadin, A. F. Kosolapov, A. D. Pryamikov, A. S. Biriukov, V. G. Plotnichenko, and E. M. Dianov. Light transmission in negative curvature hollow core fiber in extremely high material loss region. *Optics Express*, 21(8):9514–9519, 2013.

[83] J. E. Koroshetz. Fiber Lasers for Lidar. In *Optical Fiber Communication Conference and Exposition and The National Fiber Optic Engineers Conference*, page OFJ4. Optical Society of America, 2005.

[84] Y. S. Kwon, M. O. Ko, M. S. Jung, I. G. Park, N. Kim, S.-P. Han, H.-C. Ryu, K. H. Park, and M. Y. Jeon. Dynamic sensor interrogation using wavelength-swept laser with a polygon-scanner-based wavelength filter. *Sensors*, 13(8):9669–9678, 2013.

[85] K. Lee, K. Chan, and C. Shu. Self-compensated dispersion tuning of a mode-locked fiber laser using a linearly chirped fiber grating. *IEEE Photonics Technology Letters*, 13(2):106–108, 2001.

[86] K. K. Lee, A. Mariampillai, M. Haque, B. A. Standish, V. X. Yang, and P. R. Herman. Temperature-compensated fiber-optic 3d shape sensor based on femtosecond laser direct-written Bragg grating waveguides. *Optics Express*, 21(20):24076–24086, 2013.

[87] S. Lee, K. Kim, and P. J. Delfyett. Extreme chirped pulse oscillator (XCPO) using a theta cavity design. *IEEE Photonics Technology Letters*, 18(7):799–801, 2006.

[88] J. Li, Z. Sun, H. Luo, Z. Yan, K. Zhou, Y. Liu, and L. Zhang. Wide wavelength selectable all-fiber Thulium doped fiber laser between 1925 nm and 2200 nm. *Optics Express*, 22(5):5387–5399, 2014.

[89] S. Li and K. Chan. Electrical wavelength-tunable actively mode-locked fiber ring laser with a linearly chirped fiber Bragg grating. *Photonics Technology Letters, IEEE*, 10(6):799–801, 1998.

[90] S. Li and K. T. Chan. A novel configuration for multiwavelength actively mode-locked fiber lasers using cascaded fiber Bragg gratings. *IEEE Photonics Technology Letters*, 11(2):179–181, 1999.

[91] X. Li, Y. Wang, W. Zhao, W. Zhang, Z. Yang, X. Hu, H. Wang, X. Wang, Y. Zhang, Y. Gong, et al. All-normal dispersion, figure-eight, tunable passively mode-locked fiber laser with an invisible and changeable intracavity bandpass filter. *Laser Physics*, 21(5):940–944, 2011.

[92] Z. Li, S. Alam, Y. Jung, A. Heidt, and D. Richardson. All-fiber, ultra-wideband tunable laser at 2 μm. *Optics Letters*, 38(22):4739–4742, 2013.

[93] J. Limpert, F. Stutzki, F. Jansen, H.-J. Otto, T. Eidam, C. Jauregui, and A. Tünnermann. Yb-doped large-pitch fibres: effective single-mode operation based on higher-order mode delocalisation. *Light: Science & Applications*, 1(4):e8, 2012.

[94] E. Lindner, M. Becker, M. Rothhardt, and H. Bartelt. Generation and characterization of first order fiber Bragg gratings with bragg wavelengths in the visible spectral range. *Optics Communications*, 281(18):4612–4615, 2008.

[95] X. Liu, X. Yang, F. Lu, J. Ng, X. Zhou, and C. Lu. Stable and uniform dual-wavelength erbium-doped fiber laser based on fiber Bragg gratings and photonic crystal fiber. *Optics Express*, 13(1):142–147, Jan 2005.

[96] Z. Liu, Z. M. Ziegler, L. G. Wright, and F. W. Wise. Megawatt peak power from a Mamyshev oscillator. *Optica*, 4(6):649–654, 2017.

[97] S. Loranger, V. Lambin-Iezzi, and R. Kashyap. Reproducible ultra-long FBGs in phase corrected non-uniform fibers. *Optica*, 4(9):1143–1146, 2017.

[98] I. Malitson. Interspecimen comparison of the refractive index of fused silica. *Journal of the Optical Society of America*, 55(10):1205–1209, 1965.

[99] D. Mandridis, C. Williams, I. Ozdur, and P. J. Delfyett. Low noise chirped pulse mode-locked laser using an intra-cavity Fabry-Pérot etalon. *Optics Express*, 19(10):8994–8999, 2011.

[100] G. D. Marshall, R. J. Williams, N. Jovanovic, M. Steel, and M. J. Withford. Point-by-point written fiber-Bragg gratings and their application in complex grating designs. *Optics Express*, 18(19):19844–19859, 2010.

[101] H. Mavoori, S. Jin, R. P. Espindola, and T. A. Strasser. Enhanced thermal and magnetic actuations for broad-range tuning of fiber Bragg grating based reconfigurable add drop devices. *Optics Letters*, 24(11):714–716, Jun 1999.

[102] J. C. Maxwell. *A dynamical theory of the electromagnetic field*. The Society, 1864.

[103] A. Méndez. Optics in medicine. In *Optics in Our Time*, pages 299–333. Springer, 2016.

[104] F. Mitschke. *Fiber optics: physics and technology*. Springer, 2016.

[105] M. Mokhtar, C. Goh, S. Butler, S. Set, K. Kikuchi, D. Richardson, and M. Ibsen. Fibre Bragg grating compression-tuned over 110 nm. *Electronics Letters*, 39(6):509–511, 2003.

[106] J. P. Moore and M. D. Rogge. Shape sensing using multi-core fiber optic cable and parametric curve solutions. *Optics Express*, 20(3):2967–2973, 2012.

[107] N. Q. Ngo et al. *Ultra-fast fiber lasers: principles and applications with MATLAB® models*. CRC Press, 2010.

[108] J. Nilsson, W. Clarkson, R. Selvas, J. Sahu, P. Turner, S.-U. Alam, and A. Grudinin. High-power wavelength-tunable cladding-pumped rare-earth-doped silica fiber lasers. *Optical Fiber Technology*, 10(1):5 – 30, 2004.

[109] D. R. Pape and A. P. Goutzoulis. *Design and fabrication of acousto-optic devices*. M. Dekker, 1994.

[110] R. Paschotta. *Encyclopedia of Laser Physics and Technology (article: master oscillator power amplifier)*. Wiley-VCH (ISBN 978-3-527-40828-3), 2008.

[111] R. Paschotta. *Field Guide to Optical Fiber Technology*. SPIE Press, 2010.

[112] R. Paschotta. RP Photonics Excyclopedia. https://www.rp-photonics.com/encyclopedia.html, 2018.

[113] R. Paschotta, J. Nilsson, A. Tropper, and D. Hanna. Ytterbium-doped fiber amplifiers. *IEEE Journal of Quantum Electronics*, 33(7):1049 –1056, jul 1997.

[114] A. S. Paterno, N. Haramoni, J. C. Silva, and H. J. Kalinowski. Highly reliable strain-tuning of an Erbium-doped fiber laser for the interrogation of multiplexed Bragg grating sensors. *Optics Communications*, 273(1):187 – 192, 2007.

[115] G. M. Ponzo, M. N. Petrovich, X. Feng, P. Horak, F. Poletti, P. Petropoulos, and D. J. Richardson. Fast and broadband fiber dispersion measurement with dense wavelength sampling. *Optics Express*, 22(1):943–953, 2014.

[116] Y.-J. Rao. In-fibre Bragg grating sensors. *Measurement science and technology*, 8(4):355, 1997.

[117] D. Richardson, J. Nilsson, and W. Clarkson. High power fiber lasers: current status and future perspectives. *JOSA B*, 27(11):B63–B92, 2010.

[118] A. J. Rogers. *Polarization in optical fibers*. Artech House, 2008.

[119] P. S. J. Russell, J.-L. Archambault, and L. Reekie. Fibre gratings. *Physics World*, 6(10):41, 1993.

[120] B. E. A. Saleh and M. C. Teich. *Fundamentals of Photonics*. Wiley, 2nd edition, 2007.

[121] H.-T. Shang. Chromatic dispersion measurement by white-light interferometry on metre-length single-mode optical fibres. *Electronics Letters*, 17(17):603–605, 1981.

[122] K. K. Sharma. *Optics: principles and applications*. Academic Press, 2006.

[123] U. Sharma, C.-S. Kim, J. U. Kang, and N. M. Fried. Highly stable tunable dual-wavelength Q-switched fiber laser for DIAL applications. In *Laser Applications to Chemical and Environmental Analysis*, page MB3. Optical Society of America, 2004.

[124] A. W. Snyder and J. Love. *Optical waveguide theory*. Springer Science & Business Media, 2012.

[125] Y. Song, S. Havstad, D. Starodubov, Y. Xie, A. Willner, and J. Feinberg. 40-nm-wide tunable fiber ring laser with single-mode operation using a highly stretchable FBG. *IEEE Photonics Technology Letters*, 13(11):1167–1169, 2001.

[126] R. M. Sova, C.-S. Kim, and J. U. Kang. Tunable dual-wavelength all-PM fiber ring laser. *IEEE Photonics Technology Letters*, 14(3):287–289, March 2002.

[127] H. Sun, X. Liu, Y. Gong, X. Li, and L. Wang. Broadly tunable dual-wavelength erbium-doped ring fiber laser based on a high-birefringence fiber loop mirror. *Laser Physics*, 20(2):522–527, 2010.

[128] H. B. Sun, X. M. Liu, Y. K. Gong, X. H. Li, and L. R. Wang. Broadly tunable dual-wavelength erbium-doped ring fiber laser based on a high-birefringence fiber loop mirror. *Laser Physics*, 20(2):522–527, 2010.

[129] S. Taccheo, K. Schuster, M. Ferrari, A. Seddon, M. Marciniak, C. Taudt, J. Troles, G. Valentini, D. Dorosz, F. Prudenzano, et al. Challenges and future trends in fiber lasers. In *Transparent Optical Networks (ICTON), 2016 18th International Conference on*, pages 1–5. IEEE, 2016.

[130] M. Tang, H. Minamide, Y. Wang, T. Notake, S. Ohno, and H. Ito. Tunable terahertz-wave generation from dast crystal pumped by a monolithic dual-wavelength fiber laser. *Optics Express*, 19(2):779–786, Jan 2011.

[131] TechNavio. *Global Fiber Laser Market 2018-2022 (https://www.giiresearch.com/report/infi281899-global-fiber-laser-market.html)*. Infiniti Research Ltd., 2018.

[132] V. Ter-Mikirtychev. *Fundamentals of Fiber Lasers and Fiber Amplifiers*. Springer, 2014.

[133] R. Teschner. *Glasfasern*. Springer Vieweg, 2013.

[134] F. Théberge, M. Châteauneuf, J. Dubois, A. Villeneuve, J. Salhany, and B. Burgoyne. Tunable mid-infrared generation using a synchronized programmable fiber lasers. In *2011 IEEE Photonics Society Summer Topical Meeting Series*, pages 71–72, July 2011.

[135] J. Thomas, N. Jovanovic, R. G. Becker, G. D. Marshall, M. J. Withford, A. Tünnermann, S. Nolte, and M. Steel. Cladding mode coupling in highly localized fiber bragg gratings: modal properties and transmission spectra. *Optics Express*, 19(1):325–341, 2011.

[136] J. Thomas, C. Voigtlaender, R. G. Becker, D. Richter, A. Tuennermann, and S. Nolte. Femtosecond pulse written fiber gratings: a new avenue to integrated fiber technology. *Laser & Photonics Reviews*, 6(6):709–723, 2012.

[137] J. Thomas, E. Wikszak, T. Clausnitzer, U. Fuchs, U. Zeitner, S. Nolte, and A. Tünnermann. Inscription of fiber Bragg gratings with femtosecond pulses using a phase mask scanning technique. *Applied Physics A*, 86(2):153–157, 2007.

[138] J. U. Thomas. *Mode control with ultra-short pulse written fiber Bragg gratings*. Dissertation, 2012.

[139] T. Tieß. *Tunable fiber laser based on fiber-Bragg-grating-arrays - A highly flexible tuning concept enabling programmable all-fiber lasers*. AV Akademikerverlag, 2017.

[140] T. Tiess, M. Becker, M. Rothhardt, H. Bartelt, and M. Jäger. Discrete tuning concept for fiber-integrated lasers based on tailored FBG arrays and a theta cavity layout. *Optics Letters*, 42(6):1125–1128, 2017.

[141] T. Tiess, M. Becker, M. Rothhardt, H. Bartelt, and M. Jäger. Independently tunable dual-wavelength fiber oscillator with synchronized pulsed emission based on a theta ring cavity and a fiber Bragg grating array. *Optics Express*, 25(22):26393–26404, 2017.

[142] T. Tiess, M. Becker, M. Rothhardt, H. Bartelt, and M. Jäger. Tunable all-fiber PM lasers with single-and dual-wavelength emission and extended tuning range at 1μm and 2μm. In *Specialty Optical Fibers*, pages SoTh2H–4. Optical Society of America, 2018.

[143] T. Tiess, C. Chojetzki, M. Rothhardt, H. Bartelt, and M. Jäger. Fiber-integrated concept to electrically tune pulsed fiber lasers based on step-chirped fiber Bragg grating arrays. *Optics Express*, 23(15):19634–19645, 2015.

[144] T. Tiess, S. Junaid, M. Becker, M. Rothhardt, H. Bartelt, and M. L. Jäger. Discretely tunable Thulium-doped fiber-based polarization-maintaining master oscillator power amplifier using fiber Bragg grating arrays as spectral filters. *Optical Engineering*, 55(6):064106, 2016.

[145] T. Tiess, M. Rothhardt, M. Jäger, and H. Bartelt. All-fiber time-delay spectrometer for simultaneous spectral and temporal laser pulse characterization in the nanosecond range. *Applied Optics*, 52(6):1161–1167, 2013.

[146] T. Tieß, M. Sabra, M. Becker, M. Rothhardt, G. Humbert, P. Roy, H. Bartelt, and M. Jäger. Dual-wavelength fiber laser based on a theta ring cavity and an FBG array with tailored tuning range for Thz generation. In *Laser Applications Conference*, pages JM5A–35. Optical Society of America, 2017.

[147] A. Tünnermann, T. Schreiber, and J. Limpert. Fiber lasers and amplifiers: an ultrafast performance evolution. *Applied Optics*, 49(25):F71–F78, 2010.

[148] A. Villeneuve and B. Burgoyne. Programmable laser: design and applications. photonics west. In *Proc. of SPIE*, volume 7580, pages 758002–1, 2010.

[149] A. Villeneuve and N. Godbout. Tunable mode-locked laser, US Patent 8,085,822 B2, 2011.

[150] W. J. Wadsworth, A. Ortigosa-Blanch, J. C. Knight, T. A. Birks, T.-P. M. Man, and P. S. J. Russell. Supercontinuum generation in photonic crystal fibers and optical fiber tapers: a novel light source. *JOSA B*, 19(9):2148–2155, 2002.

[151] Y. Wang, J. Gong, D. Y. Wang, B. Dong, W. Bi, and A. Wang. A quasi-distributed sensing network with time-division-multiplexed fiber Bragg gratings. *IEEE Photonics Technology Letters*, 23(2):70–72, 2011.

[152] Y. Wei and B. Sun. Wavelength spacing tunable dual-wavelength single-longitudinal-mode fiber ring laser based on fiber Bragg gratings. *Laser Physics*, 19(6):1252–1256, 2009.

[153] J. Williams, I. Bennion, and N. Doran. The design of in-fiber Bragg grating systems for cubic and quadratic dispersion compensation. *Optics Communications*, 116(1-3):62 – 66, 1995.

[154] M. Wirth, A. Fix, P. Mahnke, H. Schwarzer, F. Schrandt, and G. Ehret. The airborne multi-wavelength water vapor differential absorption lidar WALES: system design and performance. *Applied Physics B*, 96(1):201, Feb 2009.

[155] S. Wu, J. Strait, R. L. Fork, and T. Morse. High-power passively mode-locked Er-doped fiber laser with a nonlinear optical loop mirror. *Optics Letters*, 18(17):1444–1446, 1993.

[156] D. Yan, Y. Wang, D. Xu, P. Liu, C. Yan, J. Shi, H. Liu, Y. He, L. Tang, J. Feng, J. Guo, W. Shi, K. Zhong, Y. H. Tsang, and J. Yao. High-average-power, high-repetition-rate tunable terahertz difference frequency generation with gase crystal pumped by 2 μ m dual-wavelength intracavity ktp optical parametric oscillator. *Photonics Research*, 5(2):82–87, Apr 2017.

[157] J. Yao, J. Yao, Y. Wang, S. C. Tjin, Y. Zhou, Y. L. Lam, J. Liu, and C. Lu. Active mode locking of tunable multi-wavelength fiber ring laser. *Optics Communications*, 191(3):341 – 345, 2001.

[158] S. Yun, D. Richardson, D. Culverhouse, and B. Kim. Wavelength-swept fiber laser with frequency shifted feedback and resonantly swept intra-cavity acoustooptic tunable filter. *IEEE Journal of Selected Topics in Quantum Electronics*, 3(4):1087–1096, 1997.

[159] S. H. Yun and B. E. Bouma. *Wavelength Swept Lasers*, pages 359–377. Springer Berlin Heidelberg, Berlin, Heidelberg, 2008.

[160] H. Zellmer, A. Tünnermann, H. Welling, and V. Reichel. Double-clad fiber laser with 30 W output power. In *Optical Amplifiers and Their Applications*, page FAW18. Optical Society of America, 1997.

[161] J. Zyskind, J. Sulhoff, J. Stone, D. Digiovanni, L. Stulz, H. Presby, A. Piccirilli, and P. Pramayon. Electrically tunable, diode-pumped Erbium-doped fibre ring laser with fibre Fabry-Pérot etalon. *Electronics Letters*, 27(21):1950–1951, 1991.

A Zusammenfassung

Abstimmbarer Faserlaser basierend auf Faser-Bragg-Gitter Arrays sowie einem Theta-Ring-Resonator

Um das große Potential von Faserlasern für die Erschließung neuer Anwendungsgebiete auszureizen, sind neue Betriebs- und Abstimmkonzepte notwendig, die einerseits die breiten spektralen Arbeitsfenster von Laserfasern für Bereiche in den Lebenswissenschaften erschließen. Um die vielfältigen Vorteile faserbasierter Netzwerke zu erhalten, werden andererseits monolithische Designs bevorzugt, die in vielen Anwendungsgebieten der Telekommunikation und Materialbearbeitung bereits die Referenz bilden.

In der vorliegenden Arbeit wurde ein faserintegriertes Abstimmkonzept für die Emissionswellenlänge von gepulsten Faserlasern entwickelt. Die Basis bilden Faser-Bragg-Gitter (FBG) als schmalbandige Spiegel, die in den Kern einer Faser eingeschrieben werden. Durch eine Aneinanderreihung von vielen einzelnen dieser Filterelemente mit individuell gestaltbaren Antwortwellenlängen erhält man einen FBG Array als vielseitig anpassbare spektrale Filterstruktur, die die Grundlage des diskreten Abstimmkonzeptes bildet. Durch ein neuartiges Resonatorlayout - den sogenannten Theta-Ring-Resonator - erreicht man trotz der räumlich verteilten Filterantworten eine konstante Pulsumlaufzeit für jede Emissionswellenlänge im Laser. Damit ergibt sich eine für ein breites Anwendungsspektrum notwendige Konstanz in der Pulsschussrate. Das Einstellen und Verstellen der Emissionswellenlänge geschieht auf der Basis vom 'Optical Gating' Konzept. Hierfür werden mit einem optischen Modulator elektronisch kurze Zeitfenster mit hoher Transmission geschalten, die die Pulslaufzeiten im Filter steuern und damit die Laseremission gezielt mit dem Feedback eines oder mehrerer FBG im Filter verknüpfen. Die jeweilige Antwortwellenlänge gibt die Emissionslinie des Lasers vor. Dieser Ansatz ermöglicht gepulste Faserlaser im faserintegrierten Layout mit breiten spektralen Arbeitsbereichen, die individuell auf Anwendungen zugeschnitten werden können.

Im Rahmen der Arbeit wurde dieses Abstimmkonzept des Theta-Faserlasers erstmals experimentell demonstriert. Das System arbeitet mit hervorragenden Emissionseigenschaften. Das beinhaltet insbesondere eine schmale Linienbreite ($< 150\,pm$) vorgegeben durch die Antwortbreite der FBG sowie einen hohen spektralen Signalkontrast von teils über $45\,dB$. Die Unterdrückung von etwaigen parasitären Emissionswellenlängen über den kompletten Arbeitsbereich des Lasers bestätigt eine effiziente Ankopplung der Laseremission an die spektrale Filterantwort. Zur Vermeidung von ungewollten Pulsregimen im verzweigten Resonatoraufbau wurden fundamentale Designkriterien für den Laser herausgearbeitet, sodass die volle spektrale Bandbreite zur Verfügung steht. Im Ytterbium-Band wurde eine Bandbreite von $50\,nm$ realisiert, die durch das Arbeitsfenster vom eingesetzten FBG Array limitiert ist.

Um das große Anwendungspotential des Theta-Faserlasers über das reine Abstimmen einer Emissionswellenlänge hinaus darzustellen, wurden beispielhaft zwei weitere Betriebskonzepte entwickelt und vorgestellt, die die Flexibilität des Konzeptes offenbaren. Im ersten Beispiel wurden Abhängigkeiten der Pulsform von der eingestellten Pulsschussrate analysiert und mittels Simulationen auf die Faserdispersion im Resonator zurückgeführt. Dieser Effekt erlaubt im Umkehrschluss die Messung der Faserdispersion über den Betriebsbereich des abstimmbaren Lasers. Diese direkte zeitliche Messmethode konnte anhand einer Bespielmessung vom Dispersionsparameter für zwei Testfasern verifiziert werden. Die Messergebnisse stimmen innerhalb von 1.3% mit einer ebenfalls implementierten Referenzmethode überein.

Ein zweites Beispiel für ein weiterführendes Betriebskonzept des Theta-Faserlasers ist durch einen abstimmbargen Mehrwellenlängenmodus gegeben. Durch ein angepasstes Ansteuersignal für den optischen Modulator kann der Laserresonator gleichzeitig auf den Antwortlinien mehre-

rer FBG anschwingen. Mit der konstanten Pulsschussrate im Theta-Ring-Resonator ergibt sich erstmals eine synchronisierte Emission von Pulsen mit unabhängig einstellbaren Emissionswellenlängen. Dieser Modus wurde experimentell anhand von einem Zweiwellenlängenbetrieb mit einer Abstimmbandbreite von 50 nm verteilt über 55 Wellenlängenpaare tiefgehend untersucht. Für die Analyse des Pulsüberlapps der beiden Emissionswellenlängen wurde ein Laufzeitspektrometer entwickelt. Mit optimierten Ansteuerparametern konnte ein Pulsüberlapp von 99% im Zweiwellenlängenbetrieb demonstriert werden. Basierend auf nichtlinearer Frequenzkonversion bietet dieser Betriebsmodus damit vielfältige Anwendungsmöglichkeiten für die Erschließung neuer Spektralbereiche (z.B. mittleres Infrarot oder Terahertz) mit faserintegrierten Pumpquellen.

Das in dieser Arbeit entwickelte Abstimmkonzept im Theta-Faserlaser bietet ein großes Potential und neue spektrale Freiheiten um faserintegrierte Laserquellen für klassische Anwendungsgebiete, wie z.B. der Materialbearbeitung von Kunststoffen, sowie neue Bereiche in den Lebenswissenschaften zu erschließen. Neben den maßgeschneiderten Abstimmbereichen, exzellenten spektralen Emissionseigenschaften und großen Tuningbandbreiten ermöglicht es basierend auf dem elektrischen Abstimmmechanismus einen fernsteuerbaren und programmierbaren Betrieb ohne mechanisch verstellbare Komponenten. Zusammen mit dem faserintegrierten Layout ist eine hohe Nutzerfreundlichkeit und Stabilität gewährleistet. Zusätzliche Flexibilität resultiert aus elektronisch verstellbaren Parametern wie der Pulsdauer im Nanosekundenbereich oder der Anzahl an Emissionswellenlänge.

B FBG array designs

FBG Array A

Parameter	Design value
Spectral operation range	$(1060 - 1069)\,nm$
Number of gratings N	10
Spectral separation	$1\,nm$ (equidistant)
Spatial spacing Δz	$3\,m$
FWHM of FBGs	$\approx 500\,pm$
Fiber model	`Thorlabs 1060XP`
Reflectivity R	$R > 99\,\%$
Aim	Maximum reflectivity for low IL, demonstrate tunablility

FBG Array B

Parameter	Design value
Spectral operation range	$(1060 - 1085)\,nm$
Number of gratings N	11
Spectral separation	$2.5\,nm$ (equidistant)
Spatial spacing Δz	$2.5\,m$
FWHM of FBGs	$\approx 150\,pm$
Fiber model	`Thorlabs 1060XP` (non-PM), Hydrogen loaded
Reflectivity R	$R \approx 95 - 98\,\%$
Aim	spectrally isolated FBG peaks, extended tuning range

FBG Array C

Parameter	Design value
Spectral operation range	$(1047 - 1097)\,nm$
Number of gratings N	11
Spectral separation	$5\,nm$ (equidistant)
Spatial spacing Δz	$1.3\,m$
FWHM of FBGs	$\approx 150\,pm$
Fiber model	`Nufern PM980-XP` (PM)
Reflectivity R	$R \approx 90 - 95\,\%$
Aim	PM design, more extended tuning range, smaller FBG separation due to faster AOM

FBG Array D

Parameter	Design value
Spectral operation range	$(1062.3 - 1065.7)\,nm$
Number of gratings N	3
Spectral separation	$1.7\,nm$ (equidistant)
Spatial spacing Δz	$5\,m$
FWHM of FBGs	$\approx (150 - 200)\,pm$
Fiber model	`Thorlabs 1060XP` (non-PM)
Reflectivity R	$R \approx 95\,\%$
Aim	2-λ mode, tuning range adapted for TDS measurement, large spatial FBG separation for more freedom in optical gating parameters

DTG Array

Parameter	Design value
Spectral operation range	$(1061 - 1067)\,nm$
Number of gratings N	61
Spectral separation	$100pm\,nm$ (equidistant)
Spatial spacing Δz	$2\,m$
FWHM of FBGs	$\approx 50\,pm$
Fiber model	`IPHT 194MA0` ($4.6/125\,\mu m$, non-PM) - draw tower inscription
Reflectivity R	$R < 40\,\%$
Aim	TDS measurement of TCFL in $2 - \lambda$ mode, analysis of pulse dynamics

C Acronyms and symbols

List of acronyms

Acronym	Meaning
1-λ, 2-λ, 3-λ	single-wavelength, dual-wavelength, triple-wavelength
ASE	amplified spontaneous emission
AWG	arbitrary waveform generator
a.u.	arbitrary units
CH	channel, e.g. of oscilloscope
CW	continuous wave - steady operation
dB	decibel
DTG	draw tower grating
e.g.	exempli gratia (for example)
Er	Erbium
FUT	fiber under test
FWHM	full width at half maximum
FWM	four-wave mixing
GVD	group velocity dispersion
GW	gate width (electrical width of transmission window)
i.e.	id est (in other words)
IL	insertion losses
IR	infrared (spectral region - $\sim 780\ nm < \lambda <\sim 1\ mm$)
LD	laser diode
MOPA	master oscillator power amplifier
MP	modulation period - gate signal period of AOM = T_{MP}
NA	numerical aperture, also referred to as core-NA
OC	output coupler of laser cavity
OSA	optical spectrum analyzer
OSCI	oscilloscope
PM	polarization maintaining
ppm	parts per million
PRR	pulse repetition rate f_{PRR}
PRTT	pulse round-trip time T_{RT}
PSC	pump signal combiner
RE	rare earth
TCFL	theta cavity fiber laser
TDS	time-delay spectrometer
SM	single-mode (guiding of only a single transversal modes)
Tm	Thulium
Yb	Ytterbium
YDF	Ytterbium-doped fiber
UV	ultraviolet

List of symbols

Symbol	Description
z	coordinate along fiber axis
t	time
$\vec{r}$	position vector
L	length of fiber
L_{eff}	effective length of (active) fiber
λ	wavelength of the light in vacuum
t	time
n	refractive index
i, j, p, q	integer: $i, j, p, q \in \mathbb{N}$
c_0	speed of light in vacuum
c	speed of light in medium
ω	radial frequency
$k_0 = \frac{2\pi}{\lambda} = \frac{\omega}{c_0}$	vacuum wave number k_0
β	propagation constant for a specific mode in the fiber
$\beta_{(j)}$	propagation constant of mode j in the fiber
ρ	radial coordinate in cylindrical coordinate system
φ	azimuthal coordinate in cylindrical coordinate system
r_{core}	radius of fiber core
n_{core}	refractive index of fiber core
r_{clad}	radius of fiber cladding
n_{clad}	refractive index of fiber cladding
n_{clad2}	refractive index of second fiber cladding (double-clad geometry)
A_{core}	cross-section area of fiber core $A_{core} = \pi r_{core}^2$
A_{clad}	cross-section area of fiber cladding (including the core) $A_{clad} = \pi r_{clad}^2$
n_{eff}	effective refractive mode index (guided modes: $n_{clad} < n_{eff} < n_{core}$)
NA	numerical aperture $NA = \sqrt{n_{core}^2 - n_{clad}^2}$, also referred to as core-NA
$V = r_{core} k_0 NA$	normalized frequency
MFD	mode field diameter
A_{eff}	effective mode field area $A_{eff} = \pi/4 \cdot MFD^2$
Γ	normalized overlap integral factor of fundamental mode and doped core region
v_{ph}	phase velocity
v_{gr}	group velocity
$n_{gr,eff}$	effective group index of a mode in a fiber
τ_{gr}	group propagation time along fiber length L
D_λ	dispersion parameter
$D_{\lambda,theor.}$ & $D_{\lambda,exp.}$	simulated and experimental dispersion parameter
$\beta_2 = \frac{d^2\beta}{d\omega^2}$	group velocity dispersion parameter
$\mathbf{E}$	electric field vector
$\widetilde{\mathbf{E}}$	electric field vector in frequency domain
$\mathbf{P}$	polarization vector
μ_0	vacuum permeability
ϵ_0	vacuum permittivity
$\chi^{(i)}$	i^{th} order susceptibility tensor for dielectric medium
L_{FBG}	length of FBG
Λ_{FBG}	grating period of an FBG
λ_{FBG}	reflection wavelength of an FBG

$\Delta\lambda_{FBG}$	feedback bandwidth of an FBG (FWHM)
$\Delta\lambda_{FBG,0}$	feedback bandwidth of an FBG (separation of zeros)
Δz	equidistant distance between neighboring FBGs in a FBG array
z_0	distance of Modulator and the beginning of the filter section in the TCFL
t_R	rise time (10% level to 90% level)
m	diffraction order ($m \in \mathbb{Z}$) or modulation order ($m \in \mathbb{N}$)
R	peak reflectivity of FBG
N_i	population density in energetic level i
N_1	population density in energetic level 1 - ground state
N_2	population density in energetic level 2 - excited state
N_{total}	total dopant density
n_i	normalized or relative population density in energetic level i
n_1	normalized or relative population density in energetic level 1 - ground state
n_2	normalized or relative population density in energetic level 2 - excited state
P	power of laser signal
$g(\lambda)$	spectral gain coefficient
$G(\lambda)$	spectral gain factor (Neper scale)
$G_{dB}(\lambda)$	spectral gain factor (decibel scale)
$\sigma_e(\lambda)$	spectral emission cross section
$\sigma_a(\lambda)$	spectral absorption cross section
T_{RT}	pulse round-trip time in resonator
T_{MP}	modulation period
$T_{MP,0}$	default modulation period matching the precise PRTT in the TCFL, featuring symmetric parabola-like pulse shapes and highest spectral signal contrast
ΔT_{MP}	deviations in T_{MP} from its default value, i.e. $(T_{MP} - T_{MP,0})$
$\Delta T_{MP,0}$	shift of $T_{MP,0}$ over the tuning range of the TCFL
$\delta T_{MP,0}$	shift of $T_{MP,0}$ between two cavity designs or measurements at corresponding λ_L
f_{PRR}	pulse repetition rate $= T_{MP}^{-1}$
τ_{GW}	electrical gate width of the optical gating signal
τ_{GWi}	i^{th}electrical gate width of the optical gating signal
$\tau_{GW,opt}$	opening duration of optical gate
τ_{i-j}	temporal delay between gate i and gate j of the optical gating signal ($i, j \in \mathbb{N}$)
τ_{1-2}	temporal delay between gate 1 and gate 2 of the optical gating signal
$\tau_{1-2,i}$	temporal delay between gate 1 and gate 2 of the optical gating signal to address FBG i
$\tau_{1-2,max}$	maximum temporal delay between gate 1 and gate 2 with respect to the filter matches $\tau_{1-2,N}$ using an FBG array
$\tau_{1-2,min}$	minimum temporal delay between gate 1 and gate 2 with respect to the filter, matches $\tau_{1-2,1}$ using an FBG array
τ_{pulse}	pulse duration (FWHM)
T_{filter}	filter response time with respect to the modulator in the TCFL
A_i	electrical amplitude of gate window i of the optical gating signal
λ_L	peak emission wavelength of laser
λ_{Li}	peak emission wavelength of the i^{th} emission line of the laser
$\Delta\lambda_L$	linewidth (FWHM) of laser emission line
$\delta\lambda_L$	tuning bandwidth of laser
λ_{SB1}, λ_{SB2}	wavelength of FWM side bands
I_C	normalized self-convolution of a pulse profile
$\widehat{I}_C$	peak of normalized self-convolution trace of a pulse

D Files in the multimedia appendix

1. `Single-Wavelength-Tuning.mp4` (see Fig. 3.11)
2. `Single-Wavelength-TuningOC1&OC2.avi` (see Fig. 3.14)
3. `Dual-Wavelength-Tuning-over-25nm.mp4` (see Fig. 4.8 as well as Fig. 4.13)
4. `Dual-Wavelength-scan-balance-Amplitude.mp4` (see Fig. 4.9)
5. `Dual-Wavelength-Regimes-Transition.mp4` (see Fig. 4.12 as well as Fig. 4.11)
6. `Dual-Wavelength-Tuning-over-50nm-linear.avi` (see Fig. 4.13)
7. `Dual-Wavelength-scannedDelay.mp4` (see Fig. 4.18 as well as Fig. 4.19a)

E List of publications

Peer-reviewed journal publications

1. Hofmann, P., Mafi, A., Jollivet, C., **Tiess, T.**, Peyghambarian, N., and Schülzgen, A. (2012). *Detailed investigation of mode-field adapters utilizing multimode-interference in graded index fibers.* Journal of Lightwave Technology, 30(14), 2289-2298.

2. **Tiess, T.**, Rothhardt, M., Jäger, M., and Bartelt, H. (2013). *All-fiber time-delay spectrometer for simultaneous spectral and temporal laser pulse characterization in the nanosecond range.* Applied Optics, 52(6), 1161-1167.

3. Silva, R. E., **Tiess, T.**, Becker, M., Eschrich, T., Rothhardt, M., Jäger, M., Pohl, A., and Bartelt, H. (2015). *Acousto-optic modulation of a fiber Bragg grating in suspended core fiber for mode-locked all-fiber lasers.* Laser Physics Letters, 12(4), 045101.

4. **Tiess, T.**, Chojetzki, C., Rothhardt, M., Bartelt, H., and Jäger, M. (2015). *Fiber-integrated concept to electrically tune pulsed fiber lasers based on step-chirped fiber Bragg grating arrays.* Optics Express, 23(15), 19634-19645.

5. Silva, R. E., **Tiess, T.**, Becker, M., Eschrich, T., Rothhardt, M., Jäger, M., Pohl, A., and Bartelt, H. (2015). *All-fiber 10 MHz acousto-optic modulator of a fiber Bragg grating at 1060 nm wavelength.* Optics Express, 23(20), 25972-25978.

6. **Tiess, T.**, Junaid, S., Becker, M., Rothhardt, M., Bartelt, H., and Jäger, M. (2016). *Discretely tunable thulium-doped fiber-based polarization-maintaining master oscillator power amplifier using fiber Bragg grating arrays as spectral filters.* Optical Engineering, 55(6), 064106-064106.

7. Schmidt, S., **Tiess, T.**, Schröter, S., Hambach, R., Jäger, M., Bartelt, H., Tünnermann, A., and Gross, H. (2016). *Wave-optical modeling beyond the thin-element-approximation.* Optics Express, 24(26), 30188-30200.

8. **Tiess, T.**, Becker, M., Rothhardt, M., Bartelt, H., and Jäger, M. (2017). *Discrete tuning concept for fiber-integrated lasers based on tailored FBG arrays and a theta cavity layout.* Optics Letters, 42(6), 1125-1128.

9. **Tiess, T.**, Becker, M., Rothhardt, M., Bartelt, H., and Jäger, M. (2017). *Independently tunable dual-wavelength fiber oscillator with synchronized pulsed emission based on a theta ring cavity and a fiber Bragg grating array.* Optics Express, 25(22), 26393-26404.

10. Schmidt, S., **Tiess, T.**, Schröter, S., Schwuchow, A., Jäger, M., Bartelt, H., Tünnermann, A., and Gross, H. (2017). *Noninvasive characterization of optical fibers.* Optics Letters, 42(23), 4946-4949.

Patents

1. Jäger, M., **Tieß, T.**, *Faseroptischer Lasergenerator*, Patent DE102015106633B4 (2018)

Books

1. *Tunable fiber laser based on fiber-Bragg-grating-arrays - A highly flexible tuning concept enabling programmable all-fiber lasers*, **Tobias Tieß**, AV Akademikerverlag, ISBN 978-620-2-20601-3 (2017)

First author conference presentations

1. Talk: *All Fiber Time-Delay Spectrometer - Simultaneous spectral and temporal laser pulse characterization in the nanosecond range*
   CLEO Europe 2013 - Munich (2013)

2. Poster: *Faserintegriertes Laufzeitspektrometer - Zeitaufgelöste spektrale Charakterisierung von Lichtpulsen im Nanosekundenbereich*
   DGaO Jahrestagung 2013 - Brunswick (2013)

3. Talk: *Ein faserintegriertes Konzept zur Abstimmung der Emissionswellenlänge gepulster Faserlaser*
   DGaO Jahrestagung 2014 - Karlsruhe (2014)

4. Talk: *Wavelength tunable Yb3+-doped fiber laser based on an all-fiber geometry with fiber Bragg grating arrays*
   Specialty Optical Fibers (SOF) - Barcelona, Spain (2014)

5. Talk: *Abstimmbare Faserlaser basierend auf Faser-Bragg-Gitter Arrays als spektrale Filter*
   9. Jenaer Lasertagung - Jena (2014)

6. Talk: *Electrically tunable fiber-integrated Yb-doped laser covering 74nm based on a fiber Bragg grating array*
   SPIE Photonics West - LASE, San Francisco, USA (2015)

7. Talk: *Discretely tunable pulsed fiber laser based on tailored FBG arrays*
   CLEO Europe 2015 - Munich (2015)

8. Poster: *Discretely tunable Tm-doped fiber laser using FBG arrays as spectral filter*
   Advanced Solid State Lasers (ASSL) - Berlin (2015)

9. Talk: *Discretely tunable Tm-doped fiber-based MOPA using FBG arrays as spectral filters*
   SPIE Photonics West - LASE, San Francisco, USA (2016)

10. Talk: *Tunable Yb-doped fiber laser based on a fiber Bragg grating array and a modified resonator design enabling a constant repetition rate*
    Europhoton 2016 - Vienna, Austria (2016)

11. Poster: *Tunable fiber lasers based on FBG arrays enabling tailored tuning ranges*
    10. Jenaer Lasertagung - Jena (2016)

12. Talk: *Tunable Yb-doped fiber laser based on a FBG array and a theta ring resonator ensuring a constant repetition rate*
    SPIE Photonics West - LASE, San Francisco, USA (2017)

13. Invited talk: *Tunable Fiber Lasers in the* $1\mu m$ *and* $2\mu m$ *Wavelength Range using Fiber Bragg Grating Arrays*
    OASIS - Conference and Exhibition on Optics and Electro-Optics 6 - Tel Aviv, Israel (2017)

14. Talk: *Tunable single and dual-wavelength emission of a fiber laser based on a discretely chirped FBG array and a theta ring cavity*
    CLEO Europe 2017 - Munich (2017)

15. Talk: *Tunable fiber lasers based on fiber Bragg grating arrays - a powerful platform for spectral and temporal pulse control and multi-wavelength emission*
    WSOF 2017 - Limassol, Cyprus (2017)

16. Poster: *Pulse synchronicity of an independently tunable Dual-Wavelength Theta Cavity Fiber Laser with an FBG Array*
    ASSL 2017 - Nagoja, Japan (2017)

17. Poster: *Dual-Wavelength fiber laser based on a theta ring cavity and an FBG array with tailored tuning range for THz generation*
    ASSL 2017 - Nagoja, Japan (2017)

18. Talk: *Independently tunable dual-wavelength fiber laser based on a discrete fiber Bragg grating array*
    Annual COST Meeting MP1401 - Jena (2017)

19. Talk: *Tunable all-fiber PM lasers with single-and dual-wavelength emission and extended tuning range at* $1\mu m$ *and* $2\mu m$
    Advanced Photonics Congress, Specialty Optical Fibers - Zürich, Switzerland (2018)

20. Poster: *Tunable fiber Lasers using FBG arrays for dual-wavelength emission and sub-ns-pulse generation*
    Europhoton - Barcelona, Spain (2018)

21. Talk: *An intra-cavity method to measure dispersion properties based on pulse shape variations in a tunable fiber laser*
    Annual COST Meeting MP1401 - Warsaw, Poland (2018)

F Ehrenwörtliche Erklärung

Ich erkläre hiermit ehrenwörtlich, dass ich die vorliegende Arbeit selbständig, ohne unzulässige Hilfe Dritter und ohne Benutzung anderer als der angegebenen Hilfsmittel und Literatur angefertigt habe. Zitierte Textstellen, Abbildungen sowie übernommene Daten und Konzepte sind unter Angabe der Quellen als solche kenntlich gemacht und ausgewiesen. Bei der Auswahl und Auswertung des verwendeten Materials haben mir die nachstehend aufgeführten Personen in der jeweils beschriebenen Weise unentgeltlich geholfen:

- FBG Array A wurde von Martin Becker hergestellt.
- FBG Array B,C und D wurden zusammen mit Martin Becker eingeschrieben.
- Der DTG Array wurde von Christoph Chojetzki für die erste Generation des Laufzeitspektrometers eingeschrieben.
- Die Faserlängen der `Nufern PM980-XP` Faser wurden von Christoph Chojetzki mit einem Faserspulgerät gemessen.
- Der Dispersionsmessplatz nach Referenz [47] als alternative Messmethode zum TCFL für die `Nufern PM980-XP` Faser wurde zusammen mit Alexander Hartung aufgebaut. Die numerische Datenauswertung der aufgenommenen Messkurven wurde von Alexander Hartung durchgeführt.

Weitere Personen waren an der inhaltlich-materiellen Erstellung der vorliegenden Arbeit nicht beteiligt. Insbesondere habe ich hierfür keine entgeltliche Hilfe von Vermittlungs- bzw. Beratungsdiensten (Promotionsberater oder andere Personen) in Anspruch genommen. Niemand hat von mir unmittelbar oder mittelbar geldwerte Leistungen für Arbeiten erhalten, die im Zusammenhang mit dem Inhalt der vorliegenden Dissertation stehen. Die Arbeit wurde in gleicher oder ähnlicher Form bisher weder im In- noch Ausland einer anderen Prüfungsbehörde vorgelegt. Teile dieser Arbeit wurden aus Prioritätsgründen bereits veröffentlicht.
Die geltende Promotionsordnung der Physikalisch-Astronomischen Fakultät der Friedrich-Schiller-Universität ist mir bekannt.
Ich versichere ehrenwörtlich, dass ich nach bestem Wissen die reine Wahrheit gesagt und nichts verschwiegen habe.

Jena, den 31.08.2018

(Tobias Tieß)